AUTOMATION OF MICRORAFT ARRAYS FOR STEM CELL ANALYSIS AND SORTING

Matthew DiSalvo

A dissertation submitted to the faculty at the University of North Carolina at Chapel Hill in partial fulfillment of the requirements for the degree of Doctor of Philosophy in the School of Medicine (Biomedical Engineering).

Chapel Hill
2018

Approved by:

J. Michael Ramsey

Nancy L. Allbritton

Dale O. Cowley

Frances S. Ligler

David S. Lalush

ABSTRACT

Matthew DiSalvo: Automation of Microraft Arrays for Stem Cell Analysis and Sorting
(Under the Direction of Nancy L. Allbritton)

Induced pluripotent stem cells (iPSCs) are reprogrammed somatic cells with the potential to revolutionize personalized medicine, disease modeling, and tissue engineering. Emerging therapies based upon human iPSCs (hiPSCs) are already under development for degenerative diseases such as age-related macular degeneration (AMD). Despite the ready availability of hiPSCs, their enormous clinical and research potential is limited by the need to purify the cells during generation, genetic editing, and differentiation using tedious manual methodologies. This dissertation describes the automation and further development of microraft arrays to perform the isolation and splitting of hiPSCs colonies, which is the primary bottleneck in hiPSC purification pipelines.

Microraft arrays are elastomeric microwell arrays with releasable magnetic cell culture and transfer elements, or "microrafts," held within each microwell. Microraft arrays enable the identification of cells by imaging cytometry and the isolation of cells and their associated microrafts by dislodgement from the microarray, followed by magnetic manipulation into secondary vessels. The microraft array platform has been previously shown to be automatable and able to sort cells with exceptional viability and efficiencies. However, previous platforms have lacked the speed and robustness to perform large-scale microraft releases. Furthermore, previous microraft array designs were not designed to culture isolated microcolonies of hiPSCs.

In this dissertation, microraft arrays were redesigned to isolate hundreds of microcolonies of cells, each within a nested grid of microrafts. Novel microarray microfabrication and computational modeling methods were developed to enable automated and robust imaging of microraft arrays. Image acquisition and analysis software was created to perform label-free detection of hiPSC microcolonies on microraft arrays and, in a separate application, to monitor colonic organoids. Additionally, a high-throughput automated microraft release and collection platform was developed that, for the first time, made used of real-time imaging to intelligently maximize the robustness and speed of microraft releases. This platform was utilized to isolate, culture, monitor, and successfully split hundreds of hiPSC microcolonies, thus demonstrating its utility for hiPSC purification.

For my family, especially my parents Louis and Lisa. Thank you for always encouraging me to be the best I can.

ACKNOWLEDGEMENTS

There are many people I would like to thank for providing support, guidance, and assistance during the duration of my graduate studies. I would like to particularly thank my advisor, Nancy Allbritton, for offering me a position in her lab and for guiding me throughout my graduate research career. I am also grateful to Chris Sims for his assistance both inside and outside of lab. I want to extend my gratitude to my other preliminary and dissertation committee members Mike Ramsey, Fran Ligler, Dale Cowley, David Lalush, and Anne Taylor, for their invaluable advice over the years. I acknowledge the National Institutes of Health for making my research possible with grants CA206233 and EY024556.

I want to extend my deepest gratitude to all of the members of the Allbritton lab, past and present, for making the lab a wonderful place to be day in and day out. You've all helped me immensely as scientists and as friends. I am particularly thankful to Pete Attayek for helping me get started in the lab, to Nicole Smiddy for her valiant efforts to help me become a more organized scientist, and to both for teaming up with me to solve more problems than I can count. I want to specifically mention Angie Proctor, Yuli Wang, Nick Dobes, Hannah Nowotarski, Alexis Peña, Jazz Dickinson, Jennifer Speer, Dulan Gunasekara, and Sebastian Mestril for their help and companionship. I am also indebted to all of my scientific collaborators for sharing their expertise, especially Hamp Henley, Dan Harris, Jacque Cole, Kim Kluckman, and Adriana Beltran. I am most especially grateful to my colleague Davey West for his extensive collaboration and perseverance through thick and thin. To my student mentees, Saurin Kantesaria, Jamie Lebhar,

Vinayak Subramanian, and Jules Allbritton-King: I am so proud of you. Thank you for your patience and all your help.

Most importantly, I want to thank my family and friends. I am eternally grateful to my parents, for always believing in me, for being my first and best role models, and for fostering my interest in science. Thank you to my brother Louis, for being my second half, and to my sister Adrienne for looking out for me. I want to thank all my friends and especially Anthony Pais, Daniel Carinci, Jude Murphy, Joe Mullen, Alexis Rodriguez, and Stephanie Curley for sticking with me.

TABLE OF CONTENTS

LIST OF FIGURES

LIST OF TABLES

LIST OF ABBREVIATIONS AND SYMBOLS

Δ	Temperature difference of curing
ΔA	Area change
°C	Degrees Celsius
µL	Microliter
µm	Micrometer
2D	Two-dimensional
3D	Three-dimensional
A	Scale factor
a	X slope
AcH	Acetylcholine
A_i	Area at time *i*
ANOVA	Analysis of variance
API	Application programming interface
Arf6	ADP-ribosylation factor 6
ATCC	American Type Culture Collection
ATP	Adenosine triphosphate
b	Y slope
BSA	Bovine serum albumin
c.i.	Confidence interval
Ca	Calcium
CAG	Cytomegalovirus enhancer/chicken β-actin promoter
cAMP	3',5'-cyclic adenosine monophosphate

C-B	Cholera toxin B-subunit
CCD	Charge-coupled device
CFTR	Cystic fibrosis transmembrane conductance regulator
CH_4	Methane
CLCA	Calcium-activated chloride channel
cm	Centimeter
CMOS	Complimentary metal-oxide semiconductor
CO_2	Carbon dioxide
COC	Cyclic olefin copolymer
C-T	Cholera toxin
CTA1	Cholera toxin A1
CTE	Coefficient of thermal expansion
D	Rigidity
d	Depth
DAPI	4’,6-diamidino-2-phenylindole dihydrochloride
DI	Deionized
DIC	Differential interference contrast
DMEM/F12	Dulbecco's Modified Eagle Medium/Nutrient Mixture F-12
DMSO	Dimethyl sulfoxide
DNA	Deoxyribonucleic acid
DOF	Depth of field
DTT	Dithiothreitol
E	Young's modulus

ECM	Extracellular matrix
EDTA	Ethylenediaminetetraacetic acid
EdU	(5-ethynyl-2-deoxyuridine)
EGF	Epidermal growth factor
EGFP	Enhanced green fluorescence protein
EL	Electroluminescence
ELISA	Enzyme-linked immunosorbent assay
ESEM	Environmental scanning electron microscope
F-actin	Filamentous actin
FITC	Fluorescein isothiocyanate
FOV	Field of view
g	Gravitational constant
GBL	Gamma-butyrolactone
GFP	Green fluorescent protein
GUI	Graphical user interface
Gαs	G_s alpha subunit
h	Effective thickness
h	hour
HEPES	(4-(2-hydroxyethyl)-1-piperazineethanesulfonic acid)
HESC	Human embryonic stem cell
hiPSCs	Human induced pluripotent stem cells
IACUC	Institutional animal care and use committee
ID	Identification

IFB	Immunofluorescence buffer
iPSCs	Induced pluripotent stem cells
KCl	Potassium Chloride
kDa	Kilodaltons
KH_2PO_4	Monopotassium phosphate
L	Width
m	Meter
MEMS	Microelectromechanical system
min	Minute
mL	Milliliter
mM	Millimolar
MpA	Megapascals
N_2	Nitrogen
NA	Numerical aperture
Na_2HPO_4	Disodium phosphate
NaCl	Sodium chloride
NaN_3	Sodium azide
nM	Nanomolar
P	Pressure
PAA	Polyacrylic acid
PAF	Platelet-activating factor
PBMC	Peripheral blood mononuclear cell
PBS	Phosphate buffered saline

PCA	Principle component analysis
PCR	Polymerase chain reaction
PDMS	Polydimethylsiloxane
PGE2	Prostaglandin E2
P-gp	P-glycoprotein
PI	Propidium Iodide
PKA	Protein kinase A
PMT	Photomultiplier tube
ppm	Parts per million
PS-AA	Poly(styrene-co-acrylic acid)
rcf	Relative centrifuge force
RNA	Ribonucleic acid
RNA-seq	RNA sequencing
rpm	Revolutions per minute
RPMI	Roswell Park Memorial Institute medium
s	Second
s	Side length
SDP	Standard deviation projection
SFF	Shape-from-focus
SM	Stem cell medium
sq.	Square
SVM	Support vector machine
T	Tension

t	Thickness
t_i	Time i
UCP	Micro-contact printing
UNC	University of North Carolina
UV	Ultraviolet
V	Volume
V_i	Volume at time i
VIP	Vasoactive intestinal peptide
w	Well-to-well distance
WT	Wild-type
x_0	Center X displacement
y_0	Center Y displacement
YFP	Yellow fluorescent protein
Z_m	Transverse displacement
Z_m^*	Tilt-corrected transverse displacement
α	Coefficient of thermal expansion
γFe_2O_3	Gamma-iron(III) oxide
v	Poisson's ratio
ρ	Density
σ	Standard deviation

CHAPTER 1: INTRODUCTION

1.1 Induced Pluripotent Stem Cells

Induced pluripotent stem cells (iPSCs) were first reported in 2006, when the transduction of the "Yamanaka factors" Oct4, Sox2, Klf4 and c-Myc induced a state of cellular reprogramming in somatic cells.[1–3] Under specific conditions, pluripotent cells are capable of rapid self-renewal and differentiation into the mesoderm, ectoderm, and endoderm.[4–8] The ability to derive iPSCs from somatic cells such as dermal fibroblasts or peripheral blood mononuclear cells (PBMCs) is a distinguishing advantage of iPSCs over embryonic stem cells.[9,10] Human iPSCs (hiPSCs) have enormous potential to advance human health. Patient-specific hiPSCs can be differentiated to provide disease-specific allogenic cells for personalized regenerative medicine and drug screening.[11–17] Previously unobtainable cells, now readily generated using iPSCs, have been utilized for the study of a variety of currently incurable diseases such as Alzheimer's disease, Huntington's disease, and Duchenne muscular dystrophy.[18–30,8,31–33] Furthermore, the rapid renewal and pluripotency of iPSCs have enabled researchers to create unprecedented quantities of cells for tissue engineering.[34,35]

Despite the rapid advances in hiPSC research over the past decade, several obstacles impede clinical and research applications of hiPSCs. Current challenges for hiPSCs include the safety risks of hiPSCs for clinical application, high culture costs, and lack of standardization across methodologies.[10,36–42] At the root of these challenges lies the inherent inefficiencies of hiPSC generation, gene-editing, and differentiation. Despite recent advances, somatic cell reprogramming, hiPSC gene-editing, and hiPSC differentiation processes typically yield less than

1% appropriately modified cells.[43–48] Furthermore, these cells must be purified from contaminating cells that are often only distinguishable by means of cell-destructive assays. HiPSC purification must be extensive; in clinical applications, as few as 2 unpurified stem cells are capable of forming a teratoma.[10,36,49] Virtually all hiPSC purification requires tedious manual picking of colonies, followed by the expansion, splitting, and cell-destructive assay of each colony to ultimately identify the cells of interest for continued culture. HiPSC purification by current methods is a costly and labor-intensive endeavor, often non-specific, and requires extended culture and repeated chemical dissociation of hiPSCs during which the cells can develop chromosomal instability, differentiate into an unwanted cell type, or undergo dissociation-induced apoptosis.[42,50–52] Recent approaches to automate the isolation and splitting of hiPSCs are still limited by the use of cellular labeling, extended culture times, frequent chemical dissociation, or low hiPSC viability after colony splitting.[53–57] A detailed discussion of current methods and emerging technologies for splitting hiPSCs and their limitations is presented in Section 3.1. Overall, there is a need for high-throughput technology to quickly and effectively purify hiPSCs with minimal perturbation of the cells. An idealized technology for hiPSC purification would:

(1) Isolate several hundred hiPSC colonies

(2) Split each hiPSC colony into at least 2 fractions

(3) From each colony, route one fraction for destructive assay and, contingent on the results, route another fraction for continued culture

(4) Perform (1) – (3) at the microcolony level to minimize culture time and reagent consumption

(5) Perform (1) – (3) quickly with minimal cost and labor

The focus of this dissertation is to develop an automated system to culture and split hiPSC microcolonies in preparation for downstream cell-destructive assays, thus satisfying criteria (1), (2), (4), and (5) stated above (Figure 1.1). The feasibility of Criterion (3) is established in chapter 3 and can be satisfied in the future by encoding the identities of microcolonies and their split fractions such that the results of destructive assays performed on split fractions can be related back to their mother microcolonies. The technology developed in this research would improve the speed, consistency, cost, and scalability of hiPSC purification and thus greatly facilitate research and clinical applications of the cells.

1.2 Microraft arrays

1.2.1 Introduction to microraft arrays

Microraft arrays are a microwell technology developed by the Allbritton lab, originally as a cost-effective device for imaging cytometry and sorting adherent cells.[58,59] Microraft arrays were microfabricated by photo- and soft- lithography methods. Standard photolithography was used to generate a micropillar array of photoresist on glass: substrate preparation, photoresist layering, soft baking, ultraviolet (UV) light exposure, post expose bake, development, and hard baking. Polydimethylsiloxane (PDMS) microwell arrays were molded from the silanized, hard baked template. The PDMS microwell arrays were dipcoated in a solution of poly(styrene-*co*-acrylic acid) (PS-AA) in γ-butyrolactone (GBL) containing dispersed γFe_2O_3 nanoparticles. Discontinuous dewetting of the microarray surface left a droplet of solution within each microwell, which formed a solid, micromolded microraft after evaporation of the solvent.[60] The microraft array was then attached to culture chambers, plasma treated, and sterilized before use.

The key distinguishing factor between microraft arrays and other microwell arrays is the ability to selectively isolate individual culture elements and associated cells from the microarray

grid. The micromolded magnetic polystyrene cell culture elements, or "microrafts", are individually seated within an elastomeric microwell. Cells in culture on the arrays adhere to the microraft surface and can be identified by imaging cytometry. Once a target microraft and cell(s) have been identified, a microneedle can be used to pierce the microarray and dislodge the microraft and associated cell(s). Ejected microrafts with cellular loads can then be magnetically manipulated into secondary vessels for downstream applications. The resealability of PDMS prevents the formation of leaks during repeated microneedle punctures.

Prior to this dissertation, variations on the design and use of microraft arrays have been developed. Circular microrafts were used to efficiently capture single HeLa cells.[61] Microarrays with biodegradable microrafts were used for selective implantation of cells into patient-derived xenograft mice.[62] Microraft arrays with deep, cup-shaped microrafts were used during the capture of nonadherent cells.[63,64] Microraft isolation has been performed by gravitational collection, magnetic collection into petri dishes oriented above the microarray, magnetic wand collection and transfer into well plates or PCR tubes, and collection into well plates using magnetic arrays.[58,59,63–66] Recently, the release process was automated using a motorized microneedle, microscope, and magnetic wand. This system was applied for semi- and fully- automatic isolation of microrafts of cytotoxic T lymphocytes and lymphoblast cells.[63,64] This system successfully isolated more microrafts and their associated cells than can be done feasibly using manual methods; however, a more rapid and precise approach to microraft collection was needed for applications requiring hundreds of releases or more.

1.2.2 Considerations for colony culture on microraft arrays

The use of microrafts for colony-based applications represents a significant deviation from previous approaches and warrants a re-evaluation of microraft design parameters. Prior to this

dissertation, microrafts have only been used for sorting single cells or small colonies of cells. Overall, the size of the microrafts was a minor design parameter, typically adjusted between 50 and 200 μm simply to provide the desired number of microrafts in a given area while also providing a large enough target for microneedle release. However, microraft size represents a much more critical design parameter for colony splitting. The size of the microrafts used for colony culture and splitting dictates the amount of cells in each microcolony and in each split. Especially for delicate mammalian cells such as iPSCs, the microraft size requires optimization to present enough surface area to facilitate the consistent survival of adhered colonies. In the work presented in Chapter 3, microrafts of 200 × 200 μm lateral dimensions were used to support a cellular load of 50-100 hiPSCs, depending on colony density. These quantities were sufficient for consistent expansion of colonies from microraft biopsies.

Microraft array design and culture protocols must be optimized to enable HiPSCs on the microdevices to expand into microcolonies without cross-contamination. The density of microrafts, culture duration, and seeding density are all contributing factors to the cross-contamination of adjacent cell colonies on microraft arrays. While the initial locations of cells seeded on microraft arrays follows the Poisson distribution, it can be difficult to predict the final distribution of mature colonies on microraft arrays due to the culture times required to grow microcolonies, during which cells migrate across the array. Generally, to minimize cross contamination between colonies, thus maximizing colony purity, the number of seeded cells should be decreased, or the number of microrafts increased. As discussed in Chapter 3, the additional of a physical barrier between groups of microrafts is one approach to isolate hiPSC microcolonies. Another potentially effective approach may be to selectively modify the surface of

microraft arrays, for instance by using micro-contact printing (UCP) to pattern biomolecules on the array.[67]

1.3 Automation of microraft arrays

1.3.1 Automated Image Acquisition

Automated imaging of cells and microscale features benefits from detectors capable of quickly obtaining images from a large region of interest with high sensitivity and resolution. In general, microscope stage translation speed, shuttering, objective changes, and light path changes can also be determinants of overall image acquisition speed. As discussed in detail in Chapter 2, the shape of the sample can also limit automation speeds if automated autofocusing methods are required to refocus upon regions of the sample. For Chapters 2 and 4, a Photometrics CoolSnap HQ2 (a 1.4 Megapixel CCD with 6.45 μm pixel pitch, frame readout of 90 ms, and 60% quantum efficiency) was used. However, for Chapter 3, high-speed, real time image acquisition was imperative to devising an automated system that used microscopy data to guide the microraft release process. The Hamamatsu Flash 4.0 V2 was selected for this application. Its 3× larger sensor area, 9× faster frame readout, and up 82% quantum efficiency enabled rapid imaging of microrafts during the release process.

1.3.2 User interfaces for image acquisition

Successful automation aims to reduce or eliminate human interaction for tedious or repetitive tasks while simultaneously providing user control over the processes. Scripted algorithms can very effectively eliminate human interaction during the operation of automated systems. However, the sequential coordination of multiple scripts quickly becomes impractical as the number of scripts and process complexity increase. In addition, some processes are impractical to automate or pre-script and require some level of user input. Software graphical user interfaces

(GUIs) address the above challenges to enable smooth operation of automated systems.[68] GUIs are frontends consisting of buttons, textboxes, images, and other visual features that can query user input and while also outputting information about the status of the backend automated process. Ideally, GUIs use features such as pop-up windows, collapsible panes, and tab panels to organize information in a digestible fashion.[69] For the automated systems described in this dissertation, GUIs were designed and executed using MATLAB's GUI Layout Toolbox (File Exchange #47982). This toolbox simplified the design of modular, resizable GUIs (Figure 1.2).

1.3.3 Automated image analysis

Extremely precise and specialized strategies exist to analyze microscopy data. For example, the morphological complexity of hiPSC has been probed by methods capable of quantifying such metrics as the nucleus:cytoplasm ratio, nucleoli prominence, cell compaction, colony edge definition, and colony layering.[70–76] These methods typically used supervised machine learning algorithms, which when implemented with careful calibration and optimization can be amazingly powerful. However, the automation developed for this dissertation required, above all, exceptionally robust image analysis methods that can be executed in real-time. As a result, this dissertation has focused on the application of simple but accurate methods to locate various tissues, cells, and microfeatures. The below automated image analysis challenges were addressed as a part of this dissertation:

1. Nuclear detection: Section 2.2.6
2. Microraft detection: Section 3.3.2
3. HiPSC microcolony detection: Section 3.3.5
4. Organoid segmentation: Section 4.3.7

1.4 Screening experiments: High content data analysis

Automated imaging of biological samples is a powerful tool for high content data analysis. The hardware and software for automated image acquisition, automated image analysis, and screening analysis described in Chapters 2-4 have been used for characterization of parathyroid adenoma tissue, screening of pancreatic cells for selective RNA sequencing and screening of dietary compounds on various *in vitro* murine colon models in addition to the work described in this dissertation.[65,77,78] Motorized microscopes and sensitive scientific cameras can enable rapid image-based assay of samples to acquire valuable data at tissue, cellular, and subcellular scales. In particular, automation technologies enable large-scale screening experiments. Automated microscopy provides levels of precision and consistencies to imaging that are impractical to achieve using manual methods. In particular, reduced labor requirements provided by automated systems allow the design of experiments of greater scales than could be previously considered.

However, methods of sample preparation, microscopy, and data analysis often translate poorly when applied in automated pipelines. Careful experimental design and optimization are required to best exploit the obvious advantages of automated imaging for screening. Sample preparation should be optimized for consistency and optical clarity. Notably, ensuring that the sample lies along a flat plane greatly facilitates automated imaging because automated autofocusing for curved or warped samples requires extensive, sample specific optimization. Sample substrates that provide sufficient optical clarity to draw qualitative conclusions from image data are not necessarily optimized to enable high signal-to-noise ratios for automated screening. The use of low background thin glass or cyclic olefin copolymer (COC) surfaces can enable automated measurement of quantitative and statistically relevant readouts. Additional sample concerns such as sample desiccation due to evaporation or photobleaching due to prolonged or

secondary exposures should be evaluated, especially for extended duration screening sessions within incubated systems, to determine if incubated microscopes or stages and opaque sample plates may be required.

When using well plates, the ordering and position of samples across wells and plates can be optimized to minimize the substantial inter- and intra- plate variances present in commercial plates.[79,80] Random ordering of samples within and across well plates, avoidance of evaporation-prone border wells, and the use of experimental, technical, and/or biological replicates are effective strategies to improve screening accuracy. The size of each sample to be screened is an important parameter determining not only reagent consumption, but also the accuracy of the screen readout depending on the heterogeneity of the biological samples.

Appropriate data storage and analysis pipelines are required to handle the large scales of data generated by automated imaging, which typically range from $10^9 – 10^{12}$ bytes per experiment. Although a thorough discussion of large scale data analysis is outside the scope of this work, two data analysis paradigms can be identified for high throughput screening data: 1) the use of statistical analyses to identify hits and 2) the application of machine learning and artificial intelligence.[81–84,79] As described in Chapter 4, dimensionality reduction with principle component analysis (PCA) combined with clustering analyses have proved a particularly effective method to identify patterns from complex, multidimensional data. With appropriate sample preparation, experimental design, and data handling, high-throughput image-based screening is an effective tool for probing biological samples.

1.5 Overview of this dissertation

The primary focus of this work was the development of an automated microraft array system to culture and split hiPSC microcolonies. A secondary, simultaneous focus was to apply

automated imaging and analysis for high-throughput bioassays of primary colonic tissue. Chapter 2 describes the development of microfabrication, mathematical modeling, and automated microscopy approaches to enable automated, well-focused microscopy imaging of microraft arrays. The work in Chapter 2 has been published in the journal *Analytical Chemistry*.[85] Chapter 3 details research into the detection, culture and biopsy of hiPSCs using an automated microraft array platform. The work in Chapter 3 is in preparation to be submitted as a manuscript. Chapter 4 focuses on applying automated imaging and analysis for high-throughput screening of colonic organoid tissue. The work in Chapter 4 has been published in the journal *Analytical Chemistry*.[86]

1.6 Figures

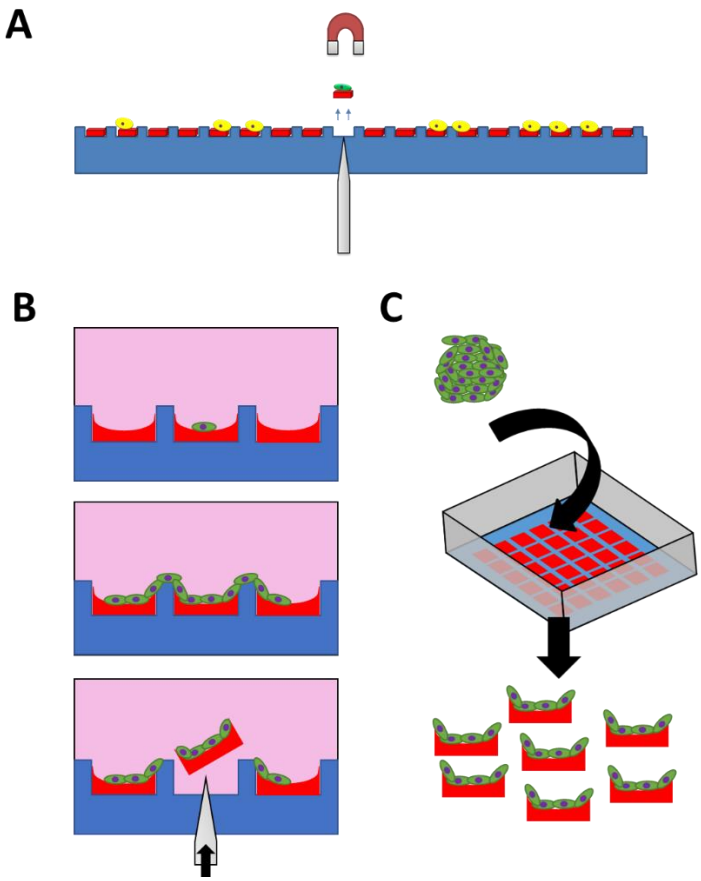

Figure 1.1 Microraft arrays for colony splitting. (A) Schematic of microraft ejection. Superparamagnetic microrafts bearing cells of interest are released from the microarray using a microneedle. Red: microrafts; blue: PDMS; yellow: cells; green: cell of interest. (B) Schematic of colony splitting using microrafts. Cells seeded on microrafts (top) that expand into microcolonies (middle) can be split by ejection of an underlying microraft from the array (bottom). (C) Schematic of microraft hiPSC colony splitting goals. A microraft array is used to quickly reformat hiPSCs into many colony splits with minimal labor and cell perturbations.

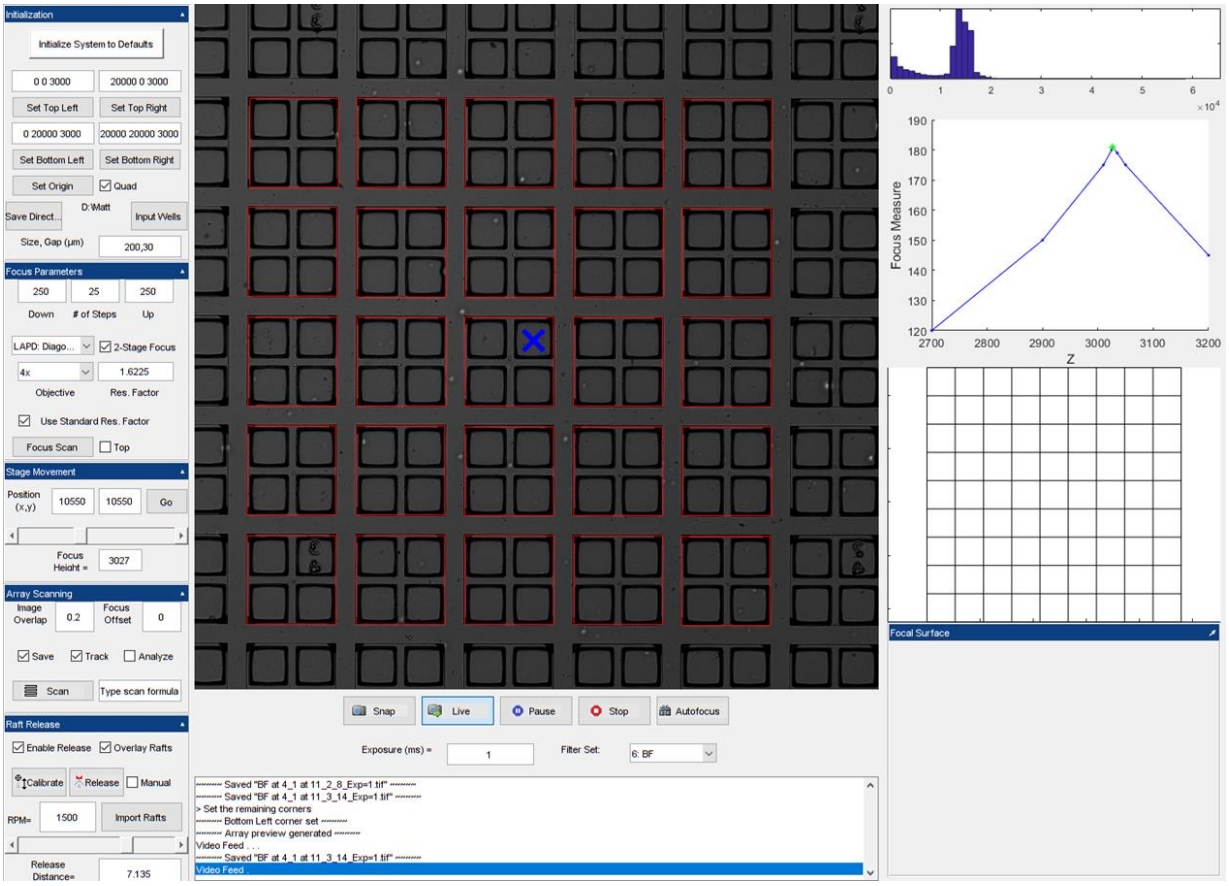

Figure 1.2 Screenshot of a MATLAB graphical user interface for automated microraft imaging and release. The left-hand side of the GUI accepts various user input, including (from top to bottom): hardware initialization, autofocusing and focus scanning, stage positioning, image acquisition and analysis, and microraft release. Image of the sample with overlays of real-time analyses, a textual summary of previously executed commands, image intensity histograms, and a map of the sample are maximized within the remaining space to provide clear and concise feedback to the user.

1.7 REFERENCES

(1) Takahashi, K.; Yamanaka, S. Induction of Pluripotent Stem Cells from Mouse Embryonic and Adult Fibroblast Cultures by Defined Factors. *Cell* **2006**, *126* (4), 663–676.

(2) Takahashi, K.; Tanabe, K.; Ohnuki, M.; Narita, M.; Ichisaka, T.; Tomoda, K.; Yamanaka, S. Induction of Pluripotent Stem Cells from Adult Human Fibroblasts by Defined Factors. *Cell* **2007**, *131* (5), 861–872.

(3) Anabe, B. K. T.; Akahashi, K. T.; Amanaka, S. Y. Review Induction of Pluripotency by de Fi Ned Factors. **2014**, *90* (3), 83–96.

(4) Kattman, S. J.; Witty, A. D.; Gagliardi, M.; Dubois, N. C.; Niapour, M.; Hotta, A.; Ellis, J.; Keller, G. Stage-Specific Optimization of Activin/Nodal and BMP Signaling Promotes Cardiac Differentiation of Mouse and Human Pluripotent Stem Cell Lines. *Cell Stem Cell* **2011**, *8* (2), 228–240.

(5) Hernández, D.; Millard, R.; Sivakumaran, P.; Wong, R. C. B.; Crombie, D. E.; Hewitt, A. W.; Liang, H.; Hung, S. S. C.; Pébay, A.; Shepherd, R. K.; et al. Electrical Stimulation Promotes Cardiac Differentiation of Human Induced Pluripotent Stem Cells. *Stem Cells Int.* **2016**, *2016*, 1–12.

(6) Burridge, P. W.; Keller, G.; Gold, J. D.; Wu, J. C. Production of De Novo Cardiomyocytes: Human Pluripotent Stem Cell Differentiation and Direct Reprogramming. *Cell Stem Cell* **2012**, *10* (1), 16–28.

(7) Pandya, H.; Shen, M. J.; Ichikawa, D. M.; Sedlock, A. B.; Choi, Y.; Johnson, K. R.; Kim, G.; Brown, M. A.; Elkahloun, A. G.; Maric, D.; et al. Differentiation of Human and Murine Induced Pluripotent Stem Cells to Microglia-like Cells. *Nat. Neurosci.* **2017**, *20* (5), 753–759.

(8) Mandai, M.; Watanabe, A.; Kurimoto, Y.; Hirami, Y.; Morinaga, C.; Daimon, T.; Fujihara, M.; Akimaru, H.; Sakai, N.; Shibata, Y.; et al. Autologous Induced Stem-Cell–Derived Retinal Cells for Macular Degeneration. *N. Engl. J. Med.* **2017**, *376* (11).

(9) Choi, J.; Lee, S.; Mallard, W.; Clement, K.; Tagliazucchi, G. M.; Lim, H.; Choi, I. Y.; Ferrari, F.; Tsankov, A. M.; Pop, R.; et al. A Comparison of Genetically Matched Cell Lines Reveals the Equivalence of Human iPSCs and ESCs. *Nat. Biotechnol.* **2015**, *33* (11), 1173–1181.

(10) De Sousa, P. A. Optimising the Therapeutic Safety of Human Embryonic Stem Cells through the Evolution of Defined Culture Systems Supporting Their Isolation. *Expert Opin Biol Ther* **2006**, *6* (6), 551–554.

(11) Shiba, Y.; Gomibuchi, T.; Seto, T.; Wada, Y.; Ichimura, H.; Tanaka, Y.; Ogasawara, T.; Okada, K.; Shiba, N.; Sakamoto, K.; et al. Allogeneic Transplantation of iPS Cell-Derived Cardiomyocytes Regenerates Primate Hearts. *Nature* **2016**, *538* (7625), 388–391.

(12) Kamao, H.; Mandai, M.; Okamoto, S.; Sakai, N.; Suga, A.; Sugita, S.; Kiryu, J.; Takahashi, M. Characterization of Human Induced Pluripotent Stem Cell-Derived Retinal Pigment Epithelium Cell Sheets Aiming for Clinical Application. *Stem Cell Reports* **2014**, *2* (2), 205–218.

(13) Song, W. K.; Park, K.-M.; Kim, H.-J.; Lee, J. H.; Choi, J.; Chong, S. Y.; Shim, S. H.; Del Priore, L. V.; Lanza, R. Treatment of Macular Degeneration Using Embryonic Stem Cell-Derived Retinal Pigment Epithelium: Preliminary Results in Asian Patients. *Stem Cell Reports* **2015**, *4* (5), 860–872.

(14) Assawachananont, J.; Mandai, M.; Okamoto, S.; Yamada, C.; Eiraku, M.; Yonemura, S.; Sasai, Y.; Takahashi, M. Transplantation of Embryonic and Induced Pluripotent Stem Cell-Derived 3D Retinal Sheets into Retinal Degenerative Mice. *Stem Cell Reports* **2014**, *2* (5), 662–674.

(15) Mathur, A.; Loskill, P.; Shao, K.; Huebsch, N.; Hong, S.; Marcus, S. G.; Marks, N.; Mandegar, M.; Conklin, B. R.; Lee, L. P.; et al. Human iPSC-Based Cardiac Microphysiological System For Drug Screening Applications. *Sci. Rep.* **2015**, *5* (1), 8883.

(16) Dempsey, G. T.; Chaudhary, K. W.; Atwater, N.; Nguyen, C.; Brown, B. S.; McNeish, J. D.; Cohen, A. E.; Kralj, J. M. Cardiotoxicity Screening with Simultaneous Optogenetic Pacing, Voltage Imaging and Calcium Imaging. *J. Pharmacol. Toxicol. Methods* **2016**, *81*, 240–250.

(17) Blinova, K.; Stohlman, J.; Vicente, J.; Chan, D.; Johannesen, L.; Hortigon-Vinagre, M. P.; Zamora, V.; Smith, G.; Crumb, W. J.; Pang, L.; et al. Comprehensive Translational Assessment of Human-Induced Pluripotent Stem Cell Derived Cardiomyocytes for Evaluating Drug-Induced Arrhythmias. *Toxicol. Sci.* **2017**, *155* (1), 234–247.

(18) Wang, G.; McCain, M. L.; Yang, L.; He, A.; Pasqualini, F. S.; Agarwal, A.; Yuan, H.; Jiang, D.; Zhang, D.; Zangi, L.; et al. Modeling the Mitochondrial Cardiomyopathy of Barth Syndrome with Induced Pluripotent Stem Cell and Heart-on-Chip Technologies. *Nat. Med.* **2014**, *20* (6), 616–623.

(19) Kondo, T.; Asai, M.; Tsukita, K.; Kutoku, Y.; Ohsawa, Y.; Sunada, Y.; Imamura, K.; Egawa, N.; Yahata, N.; Okita, K.; et al. Modeling Alzheimer's Disease with iPSCs Reveals Stress Phenotypes Associated with Intracellular Aβ and Differential Drug Responsiveness. *Cell Stem Cell* **2013**, *12* (4), 487–496.

(20) Devlin, A.-C.; Burr, K.; Borooah, S.; Foster, J. D.; Cleary, E. M.; Geti, I.; Vallier, L.; Shaw, C. E.; Chandran, S.; Miles, G. B. Human iPSC-Derived Motoneurons Harbouring TARDBP or C9ORF72 ALS Mutations Are Dysfunctional despite Maintaining Viability. *Nat. Commun.* **2015**, *6* (1), 5999.

(21) Li, H. L.; Fujimoto, N.; Sasakawa, N.; Shirai, S.; Ohkame, T.; Sakuma, T.; Tanaka, M.; Amano, N.; Watanabe, A.; Sakurai, H.; et al. Precise Correction of the Dystrophin Gene in Duchenne Muscular Dystrophy Patient Induced Pluripotent Stem Cells by TALEN and CRISPR-Cas9. *Stem Cell Reports* **2015**, *4* (1), 143–154.

(22) Ciancanelli, M. J.; Huang, S. X. L.; Luthra, P.; Garner, H.; Itan, Y.; Volpi, S.; Lafaille, F. G.; Trouillet, C.; Schmolke, M.; Albrecht, R. A.; et al. Life-Threatening Influenza and Impaired Interferon Amplification in Human IRF7 Deficiency. *Science (80-.).* **2015**, *348* (6233), 448–453.

(23) de la Torre-Ubieta, L.; Won, H.; Stein, J. L.; Geschwind, D. H. Advancing the Understanding of Autism Disease Mechanisms through Genetics. *Nat. Med.* **2016**, *22* (4), 345–361.

(24) Hoekstra, M.; Mummery, C. L.; Wilde, A. A. M.; Bezzina, C. R.; Verkerk, A. O. Induced Pluripotent Stem Cell Derived Cardiomyocytes as Models for Cardiac Arrhythmias. *Front. Physiol.* **2012**, *3*.

(25) Burnett, L. C.; LeDuc, C. A.; Sulsona, C. R.; Paull, D.; Eddiry, S.; Levy, B.; Salles, J. P.; Tauber, M.; Driscoll, D. J.; Egli, D.; et al. Induced Pluripotent Stem Cells (iPSC) Created from Skin Fibroblasts of Patients with Prader-Willi Syndrome (PWS) Retain the Molecular Signature of PWS. *Stem Cell Res.* **2016**, *17* (3), 526–530.

(26) Burnett, L. C.; LeDuc, C. A.; Sulsona, C. R.; Paull, D.; Rausch, R.; Eddiry, S.; Carli, J. F. M.; Morabito, M. V.; Skowronski, A. A.; Hubner, G.; et al. Deficiency in Prohormone Convertase PC1 Impairs Prohormone Processing in Prader-Willi Syndrome. *J. Clin. Invest.* **2016**, *127* (1), 293–305.

(27) Kawasaki, Y.; Oda, H.; Ito, J.; Niwa, A.; Tanaka, T.; Hijikata, A.; Seki, R.; Nagahashi, A.; Osawa, M.; Asaka, I.; et al. Identification of a High-Frequency Somatic *NLRC4* Mutation as a Cause of Autoinflammation by Pluripotent Cell-Based Phenotype Dissection. *Arthritis Rheumatol.* **2017**, *69* (2), 447–459.

(28) Canfield, S. G.; Stebbins, M. J.; Morales, B. S.; Asai, S. W.; Vatine, G. D.; Svendsen, C. N.; Palecek, S. P.; Shusta, E. V. An Isogenic Blood-Brain Barrier Model Comprising Brain Endothelial Cells, Astrocytes, and Neurons Derived from Human Induced Pluripotent Stem Cells. *J. Neurochem.* **2017**, *140* (6), 874–888.

(29) Gabriel, E.; Ramani, A.; Karow, U.; Gottardo, M.; Natarajan, K.; Gooi, L. M.; Goranci-Buzhala, G.; Krut, O.; Peters, F.; Nikolic, M.; et al. Recent Zika Virus Isolates Induce Premature Differentiation of Neural Progenitors in Human Brain Organoids. *Cell Stem Cell* **2017**, *20* (3), 397–406.e5.

(30) Dang, J.; Tiwari, S. K.; Lichinchi, G.; Qin, Y.; Patil, V. S.; Eroshkin, A. M.; Rana, T. M. Zika Virus Depletes Neural Progenitors in Human Cerebral Organoids through Activation of the Innate Immune Receptor TLR3. *Cell Stem Cell* **2016**, *19* (2), 258–265.

(31) Bershteyn, M.; Nowakowski, T. J.; Pollen, A. A.; Di Lullo, E.; Nene, A.; Wynshaw-Boris, A.; Kriegstein, A. R. Human iPSC-Derived Cerebral Organoids Model Cellular Features of Lissencephaly and Reveal Prolonged Mitosis of Outer Radial Glia. *Cell Stem Cell* **2017**, *20* (4), 435–449.e4.

(32) Abud, E. M.; Ramirez, R. N.; Martinez, E. S.; Healy, L. M.; Nguyen, C. H. H.; Newman, S. A.; Yeromin, A. V.; Scarfone, V. M.; Marsh, S. E.; Fimbres, C.; et al. iPSC-Derived Human Microglia-like Cells to Study Neurological Diseases. *Neuron* **2017**, *94* (2), 278–293.e9.

(33) Lim, R. G.; Quan, C.; Reyes-Ortiz, A. M.; Lutz, S. E.; Kedaigle, A. J.; Gipson, T. A.; Wu, J.; Vatine, G. D.; Stocksdale, J.; Casale, M. S.; et al. Huntington's Disease iPSC-Derived Brain Microvascular Endothelial Cells Reveal WNT-Mediated Angiogenic and Blood-Brain Barrier Deficits. *Cell Rep.* **2017**, *19* (7), 1365–1377.

(34) Takebe, T.; Sekine, K.; Enomura, M.; Koike, H.; Kimura, M.; Ogaeri, T.; Zhang, R.-R.; Ueno, Y.; Zheng, Y.-W.; Koike, N.; et al. Vascularized and Functional Human Liver from an iPSC-Derived Organ Bud Transplant. *Nature* **2013**, *499* (7459), 481–484.

(35) Tzatzalos, E.; Abilez, O. J.; Shukla, P.; Wu, J. C. Engineered Heart Tissues and Induced Pluripotent Stem Cells: Macro- and Microstructures for Disease Modeling, Drug Screening, and Translational Studies. *Adv. Drug Deliv. Rev.* **2016**, *96*, 234–244.

(36) Masuda, S.; Miyagawa, S.; Fukushima, S.; Sougawa, N.; Ito, E.; Takeda, M.; Saito, A.; Sawa, Y. Emerging Innovation towards Safety in the Clinical Application of ESCs and iPSCs. *Nat. Rev. Cardiol.* **2014**, *11* (9), 553–554.

(37) Lowry, W. E.; Quan, W. L. Roadblocks En Route to the Clinical Application of Induced Pluripotent Stem Cells. *J. Cell Sci.* **2010**, *123* (Pt 5), 643–651.

(38) Shi, Y.; Inoue, H.; Wu, J. C.; Yamanaka, S. Induced Pluripotent Stem Cell Technology: A Decade of Progress. **2016**.

(39) Carcamo-Orive, I.; Hoffman, G. E.; Cundiff, P.; Beckmann, N. D.; D'Souza, S. L.; Knowles, J. W.; Patel, A.; Papatsenko, D.; Abbasi, F.; Reaven, G. M.; et al. Analysis of Transcriptional Variability in a Large Human iPSC Library Reveals Genetic and Non-Genetic Determinants of Heterogeneity. *Cell Stem Cell* **2017**, *20* (4), 518–532.e9.

(40) Yoshihara, M.; Hayashizaki, Y.; Murakawa, Y. Genomic Instability of iPSCs: Challenges Towards Their Clinical Applications. **2015**.

(41) Turksen, K. *Stem Cells and Good Manufacturing Practices*; 2015; Vol. 1283.

(42) van der Sanden, B.; Dhobb, M.; Berger, F.; Wion, D. Optimizing Stem Cell Culture. *J. Cell. Biochem.* **2010**, *111* (4), 801–807.

(43) Schlaeger, T. M.; Daheron, L.; Brickler, T. R.; Entwisle, S.; Chan, K.; Cianci, A.; DeVine, A.; Ettenger, A.; Fitzgerald, K.; Godfrey, M.; et al. A Comparison of Non-Integrating Reprogramming Methods. *Nat. Biotechnol.* **2014**, *33* (1), 58–63.

(44) Zhou, Y.; Zeng, F. Integration-Free Methods for Generating Induced Pluripotent Stem Cells. *Genomics. Proteomics Bioinformatics* **2013**, *11* (5), 284–287.

(45) Miyaoka, Y.; Chan, A. H.; Judge, L. M.; Yoo, J.; Huang, M.; Nguyen, T. D.; Lizarraga, P. P.; So, P.-L.; Conklin, B. R. Isolation of Single-Base Genome-Edited Human iPS Cells without Antibiotic Selection. *Nat. Methods* **2014**, *11* (3), 291–293.

(46) Ding, Q.; Lee, Y.-K.; Schaefer, E. A. K.; Peters, D. T.; Veres, A.; Kim, K.; Kuperwasser, N.; Motola, D. L.; Meissner, T. B.; Hendriks, W. T.; et al. A TALEN Genome-Editing System for Generating Human Stem Cell-Based Disease Models. *Cell Stem Cell* **2013**, *12* (2), 238–251.

(47) Chen, F.; Pruett-Miller, S. M.; Huang, Y.; Gjoka, M.; Duda, K.; Taunton, J.; Collingwood, T. N.; Frodin, M.; Davis, G. D. High-Frequency Genome Editing Using ssDNA Oligonucleotides with Zinc-Finger Nucleases. *Nat. Methods* **2011**, *8*, 753.

(48) Hu, B.-Y.; Weick, J. P.; Yu, J.; Ma, L.-X.; Zhang, X.-Q.; Thomson, J. A.; Zhang, S.-C. Neural Differentiation of Human Induced Pluripotent Stem Cells Follows Developmental Principles but with Variable Potency. *Proc. Natl. Acad. Sci.* **2010**, *107* (9), 4335 LP-4340.

(49) Lawrenz, B.; Schiller, H.; Willbold, E.; Ruediger, M.; Muhs, A.; Esser, S. Highly Sensitive Biosafety Model for Stem-Cell-Derived Grafts. *Cytotherapy* **2004**, *6* (3), 212–222.

(50) Beers, J.; Gulbranson, D. R.; George, N.; Siniscalchi, L. I.; Jones, J.; Thomson, J. A.; Chen, G. Passaging and Colony Expansion of Human Pluripotent Stem Cells by Enzyme-Free Dissociation in Chemically Defined Culture Conditions. *Nat Protoc* **2012**, *7*, 2029–2040.

(51) Draper, J. S.; Smith, K.; Gokhale, P.; Moore, H. D.; Maltby, E.; Johnson, J.; Meisner, L.; Zwaka, T. P.; Thomson, J. A.; Andrews, P. W. Recurrent Gain of Chromosomes 17q and 12 in Cultured Human Embryonic Stem Cells. *Nat. Biotechnol.* **2004**, *22* (1), 53–54.

(52) Gonzalez, F.; Boue, S.; Izpisua Belmonte, J. C. Methods for Making Induced Pluripotent Stem Cells: Reprogramming a La Carte. *Nat Rev Genet* **2011**, *12* (4), 231–242.

(53) Haupt, S.; Grutzner, J.; Thier, M. C.; Kallweit, T.; Rath, B. H.; Laufenberg, I.; Forgber, M.; Eberhardt, J.; Edenhofer, F.; Brustle, O. Automated Selection and Harvesting of Pluripotent Stem Cell Colonies. *Biotechnol Appl Biochem* **2012**, *59* (2), 77–87.

(54) Paull, D.; Sevilla, A.; Zhou, H.; Hahn, A. K.; Kim, H.; Napolitano, C.; Tsankov, A.; Shang, L.; Krumholz, K.; Jagadeesan, P.; et al. Automated, High-Throughput Derivation, Characterization and Differentiation of Induced Pluripotent Stem Cells. *Nat. Methods* **2015**, *12* (9), 885–892.

(55) Joannides, A.; Fiore-Hériché, C.; Westmore, K.; Caldwell, M.; Compston, A.; Allen, N.; Chandran, S. Automated Mechanical Passaging: A Novel and Efficient Method for Human Embryonic Stem Cell Expansion. *Stem Cells* **2006**, *24* (2), 230–235.

(56) Daniszewski, M.; Crombie, D. E.; Henderson, R.; Liang, H. H.; Wong, R. C. B.; Hewitt, A. W.; Pébay, A. Automated Cell Culture Systems and Their Applications to Human Pluripotent Stem Cell Studies. *SLAS Technol. Transl. Life Sci. Innov.* **2017**, 247263031771222.

(57) Crombie, D. E.; Daniszewski, M.; Liang, H. H.; Kulkarni, T.; Li, F.; Lidgerwood, G. E.; Conquest, A.; Hernández, D.; Hung, S. S.; Gill, K. P.; et al. Development of a Modular Automated System for Maintenance and Differentiation of Adherent Human Pluripotent Stem Cells. *SLAS Discov. Adv. Life Sci. R&D* **2017**, *22* (8), 1016–1025.

(58) Wang, Y.; Phillips, C.; Xu, W.; Pai, J.-H.; Dhopeshwarkar, R.; Sims, C. E.; Allbritton, N. L. Micromolded Arrays for Separation of Adherent Cells. *Lab Chip* **2010**, *10* (21), 2917–2924.

(59) Gach, P. C.; Wang, Y.; Phillips, C.; Sims, C. E.; Allbritton, N. L. Isolation and Manipulation of Living Adherent Cells by Micromolded Magnetic Rafts. *Biomicrofluidics* **2011**, *5* (3), 32002–3200212.

(60) Jackman, R. J.; Duffy, D. C.; Ostuni, E.; Willmore, N. D.; Whitesides, G. M. Fabricating Large Arrays of Microwells with Arbitrary Dimensions and Filling Them Using Discontinuous Dewetting. *Anal. Chem.* **1998**, *70* (11), 2280–2287.

(61) Wang, Y.; Phillips, C.; Xu, W.; Pai, J.-H.; Dhopeshwarkar, R.; Sims, C. E.; Allbritton, N. Micromolded Arrays for Separation of Adherent Cells. *Lab Chip* **2010**, *10* (21), 2917.

(62) Wang, Y.; Phillips, C. N.; Herrera, G. S.; Sims, C. E.; Yeh, J. J.; Allbritton, N. L. Array of Biodegradable Microrafts for Isolation and Implantation of Living, Adherent Cells. *RSC Adv.* **2013**, *3*, 9264–9272.

(63) Attayek, P. J.; Hunsucker, S. A.; Sims, C. E.; Allbritton, N. L.; Armistead, P. M. Identification and Isolation of Antigen-Specific Cytotoxic T Lymphocytes with an Automated Microraft Sorting System. *Integr. Biol. (Camb).* **2016**, *8* (12), 1208–1220.

(64) Attayek, P. J.; Hunsucker, S. A.; Wang, Y.; Sims, C. E.; Armistead, P. M.; Allbritton, N. L. Array-Based Platform to Select, Release, and Capture Epstein-Barr Virus-Infected Cells Based on Intercellular Adhesion. *Anal. Chem.* **2015**, *87* (24).

(65) Welch, J. D.; Williams, L. A.; DiSalvo, M.; Brandt, A. T.; Marayati, R.; Sims, C. E.; Allbritton, N. L.; Prins, J. F.; Yeh, J. J.; Jones, C. D. Selective Single Cell Isolation for Genomics Using Microraft Arrays. *Nucleic Acids Res.* **2016**, *44* (17), 8292–8301.

(66) Gordon, K. R.; Wang, Y.; Allbritton, N. L.; Taylor, A. M. Magnetic Alignment of Microelements Containing Cultured Neuronal Networks for High-Throughput Screening. *J. Biomol. Screen.* **2015**, *20* (9), 1091–1100.

(67) Kumar, A.; Whitesides, G. M. Features of Gold Having Micrometer to Centimeter Dimensions Can Be Formed through a Combination of Stamping with an Elastomeric Stamp and an Alkanethiol "'ink'" Followed by Chemical Etching. *Appl. Phys. Lett.* **1993**, *63* (14), 2002–2004.

(68) Vallerio, K. S.; Zhong, L.; Jha, N. K. Graphical User Interface Design. In *Modern Industrial Automation Software Design*; John Wiley & Sons, Inc.: Hoboken, NJ, USA, 2006; Vol. 5, pp 53–57.

(69) Galitz; O., W. *The Essential Guide to User Interface Design: An Introduction to GUI Design Principles and Techniques*; Wiley Pub, 2002.

(70) Wakui, T. Method for Evaluation of Human Induced Pluripotent Stem Cell Quality Using Image Analysis Based on the Biological Morphology of Cells. *J. Med. Imaging* **2017**, *4* (4), 1.

(71) Sirenko, O.; Hesley, J.; Rusyn, I.; Cromwell, E. F. High-Content High-Throughput Assays for Characterizing the Viability and Morphology of Human iPSC-Derived Neuronal Cultures. *Assay Drug Dev. Technol.* **2014**, *12* (9–10), 536–547.

(72) Nagasaka, R.; Gotou, Y.; Yoshida, K.; Kanie, K.; Shimizu, K.; Honda, H.; Kato, R. Image-Based Cell Quality Evaluation to Detect Irregularities under Same Culture Process of Human Induced Pluripotent Stem Cells. *J. Biosci. Bioeng.* **2017**, *123* (5), 642–650.

(73) Kerz, M.; Folarin, A.; Meleckyte, R.; Watt, F. M.; Dobson, R. J.; Danovi, D. A Novel Automated High-Content Analysis Workflow Capturing Cell Population Dynamics from Induced Pluripotent Stem Cell Live Imaging Data. *J. Biomol. Screen.* **2016**.

(74) Healy, L.; Ruban, L. *Atlas of Human Pluripotent Stem Cells in Culture*; Springer US: Boston, MA, 2015.

(75) Maddah, M.; Shoukat-Mumtaz, U.; Nassirpour, S.; Loewke, K. A System for Automated, Noninvasive, Morphology-Based Evaluation of Induced Pluripotent Stem Cell Cultures. *J. Lab. Autom.* **2014**, *19* (5), 454–460.

(76) Tokunaga, K.; Saitoh, N.; Goldberg, I. G.; Sakamoto, C.; Yasuda, Y.; Yoshida, Y.; Yamanaka, S.; Nakao, M. Computational Image Analysis of Colony and Nuclear Morphology to Evaluate Human Induced Pluripotent Stem Cells. *Sci. Rep.* **2014**, *4*, 6996.

(77) Koh, J.; Hogue, J. A.; Wang, Y.; DiSalvo, M.; Allbritton, N. L.; Shi, Y.; Olson, J. A.; Sosa, J. A. Single-Cell Functional Analysis of Parathyroid Adenomas Reveals Distinct Classes of Calcium Sensing Behaviour in Primary Hyperparathyroidism. *J. Cell. Mol. Med.* **2016**, *20* (2), 351–359.

(78) Wang, Y.; DiSalvo, M.; Gunasekara, D. B.; Dutton, J.; Proctor, A.; Lebhar, M. S.; Williamson, I. A.; Speer, J.; Howard, R. L.; Smiddy, N. M.; et al. Self-Renewing Monolayer of Primary Colonic or Rectal Epithelial Cells. *CMGH* **2017**, *4* (1), 165–182.e7.

(79) Malo, N.; Hanley, J. A.; Cerquozzi, S.; Pelletier, J.; Nadon, R. Statistical Practice in High-Throughput Screening Data Analysis. *Nat. Biotechnol.* **2006**, *24* (2), 167–175.

(80) Mishra, K. P.; Ganju, L.; Sairam, M.; Banerjee, P. K.; Sawhney, R. C. A Review of High Throughput Technology for the Screening of Natural Products. *Biomed. Pharmacother.* **2008**, *62* (2), 94–98.

(81) Zhang, X. D. Illustration of SSMD, Z Score, SSMD*, Z* Score, and T Statistic for Hit Selection in RNAi High-Throughput Screens. *J. Biomol. Screen.* **2011**.

(82) Zhang, X. D. A Method for Effectively Comparing Gene Effects in Multiple Conditions in RNAi and Expression-Profiling Research. *Pharmacogenomics* **2009**, *10* (3), 345–358.

(83) Zhang, X. D. A New Method with Flexible and Balanced Control of False Negatives and False Positives for Hit Selection in RNA Interference High-Throughput Screening Assays.

(84) Meyer, R. D.; Cook, D. Visualization of Data. *Curr. Opin. Biotechnol.* **2000**, *11* (1), 89–96.

(85) DiSalvo, M.; Harris, D. M.; Kantesaria, S.; Peña, A. N.; Allbritton-King, J. D.; Cole, J. H.; Allbritton, N. L. Characterization of Tensioned PDMS Membranes for Imaging Cytometry on Microraft Arrays. *Anal. Chem.* **2018**, acs.analchem.8b00176.

(86) Gunasekara, D. B.; DiSalvo, M.; Wang, Y.; Nguyen, D. L.; Reed, M. I.; Speer, J.; Sims, C. E.; Magness, S. T.; Allbritton, N. L. Development of Arrayed Colonic Organoids for Screening of Secretagogues Associated with Enterotoxins. *Anal. Chem.* **2018**, *90* (3), 1941–1950.

CHAPTER 2: CHARACTERIZATION OF TENSIONED PDMS MEMBRANES FOR IMAGING CYTOMETRY ON MICRORAFT ARRAYS[1]

2.1 Introduction

Thin membranes are critical components in physical sensors, bioanalytical devices, and micro-electromechanical systems (MEMS) devices, often exhibiting unique properties that depend on their material composition and geometry. Microscale elastomeric membranes, specifically those made from polydimethylsiloxane (PDMS), have been widely adopted for their desirable properties since PDMS is gas permeable, optically clear, and biocompatible. Additionally, PDMS is able to undergo large reversible deformations, reseal naturally after punctures, and be rapidly prototyped. PDMS membranes are found as central components for many devices in diverse roles including adaptive lenses, soft cell culture surfaces, selective gas separators, and tunable optical gratings.[1–4] For microdevices, specifically, PDMS membranes have been used as biocompatible coatings, observation windows, and microfiltration interfaces.[5–8] Thin PDMS membranes have also become established as substrates for microarrays, since they are readily paired with optical assays and various cell types.[9,10] The beneficial properties of PDMS membranes enables them to act as critical design elements in a remarkably wide range of applications.

One drawback shared by most thin films and membranes, including PDMS membranes, is their low mechanical rigidity that limits their durability and makes control over their spatial orientation challenging. Membrane design and performance have been recognized to be device-

[1] Reprinted with permission from *Anal. Chem.*, 2018, 90 (7), pp 4792–4800, DOI:10.1021/acs.analchem.8b00176. Copyright 2018 American Chemical Society.

and application- dependent.[11] Some strategies adopted to address the deflection of PDMS microarrays and membranes include thickening the membrane or otherwise incorporating solid substrates or support beams.[6,9] However, these strategies come with tradeoffs: thicker membranes have poorer imaging and gas transport properties, and it is not always possible to include auxiliary supports to the membranes without reducing the functionality of the membrane. For optical applications, in particular, there is a need to use exceptionally thin substrates that maintain flatness. For example, Raman microscopy of cells relies on the detection of inherently weak spectra and benefits from situating samples on thin substrates to enable the use of low working distance, high numerical aperture objectives that improve the signal-to-noise ratio.[12] Yet, the deformation of such thin PDMS substrates would make the focused acquisition of signals from multiple positions on the membrane practically infeasible. Overall, it is challenging to control PDMS membrane deflection without imposing limitations on the desired function of the membrane.

Microraft arrays are specialized microarrays with applications in cytometry and cell sorting.[13,14] These arrays are particularly sensitive to deformation because they rely on a thin, free-standing PDMS membrane as a substrate. Microraft arrays are uniquely capable of efficiently sorting of cells based on complex spatiotemporal phenotypes without impacting cell viability.[15,16] The arrays also have applications in sorting small sample sizes or extremely rare cells as well as fragile cell types such as primary cells.[17,18] Microraft arrays contain $\geq 10^3$ microscale magnetic polystyrene, cell-culture elements called "microrafts," each situated within a square microwell in a thin PDMS membrane. However, the PDMS microarray membrane – which is 80 times as wide as it is thin – experiences deflection under the load of cell culture media and the resulting curved microarray surface poses significant challenges for microscopy imaging, cytometry, and cell sorting (Figure 2.1). Microraft arrays can function as cell sorting devices but only if the bottom of

the membrane is freely accessible by the microneedle used to isolate individual microrafts (Figure 2.1C). Thus, the use of support structures or the addition of pressurization below the membrane to oppose the deflection are not viable options. Previous approaches to compensate for the deflection have included manual refocusing of the array during imaging, using low numerical aperture (NA) and magnification objectives for imaging, using cyclic olefic copolymer (COC) as the array substrate, and using glass supports; yet these approaches have not been universally effective.

Few options exist to reduce the deformation of thin membranes. Examples include increasing the thickness/length ratio of the membrane, increasing material stiffness, or introducing tension to the membrane; however, for many microdevices, including microraft arrays, the membrane geometry and membrane material choice are tightly constrained design parameters. Herein is described a method to flatten thin membranes by storing thermal energy within the membrane during fabrication. Additionally, an analytical model was developed describing the deflection of square microarray membranes under a static load and was used to develop minimally deflecting microarrays. This tension model was used to guide materials selection and geometric and fabrication parameters for microraft arrays. The theoretical model was extensively validated against experimental measurements of microarrays fabricated on a variety of thin PDMS membranes. Finally, the tension model was incorporated into automated microscopy imaging of cells arrayed on a thin membrane substrate, enabling rapid and accurate focusing for automated cytometry. The fabrication method for membranes with thermally induced tension and the modeling approach for pre-tensioned membranes have wide applicability to the fabrication and optimization of microdevices using vulcanizable thin films, particularly when paired with optical-based assays.

2.2 Materials and Methods

2.2.1 Materials

Sylgard 184 PDMS was prepared from a silicone elastomer kit (Dow Corning, Midland, MI). EPON Resin 1002-F was purchased from Hexion, Inc. (Columbus, OH). Octyltrichlorosilane (97%) was purchased from Sigma-Aldrich (St. Louis, MO). 30-kDa polyacrylic acid was purchased from Polysciences, Inc. (Warrington, PA). Wild-type H1299 cells originally from ATCC (Manassas, VA) were altered to stably express green fluorescent protein (GFP) in previous work.[19] RPMI-1640 culture media, fetal bovine serum (FBS), and penicillin/streptomycin were obtained from Thermo Fisher Scientific (Waltham, MA).

2.2.2 Microraft Array Fabrication

Microraft arrays utilizing a sacrificial glass backing to transfer the array membrane onto a media chamber were fabricated as reported previously.[18] 1002-F negative photoresist master templates consisting of 100 μm tall, 200×200 μm pillars on glass separated by 30 μm were fabricated and covalently modified with octyltrichlorosilane to reduce adhesion. Sacrificial rigid substrates for the microarrays were prepared by spin coating a thin layer of polyacrylic acid onto glass slides at 1500 rpm for 30 seconds. PDMS was poured into the master template and degassed before a sandwich was formed with the sacrificial rigid backing. The assembly was cured at ≥95 °C for 40 minutes. Demolding the glass-backed PDMS from the silanized template resulted in a microwell array, which was then dip-coated in magnetic polystyrene solution consisting of 18% mass/mass poly(styrene-*co*-acrylic acid) doped with Fe_2O_3 nanoparticles in gamma butyrolactone. Beads of polystyrene left in each well by discontinuous de-wetting from the hydrophobic PDMS formed microrafts after baking off the solvent at 95 °C. The microraft arrays were oxygen plasma treated (Harrick Plasma) for 3 minutes prior to being secured to polycarbonate cassettes using

PDMS glue, cured at 70 °C for 3 hours or room temperature for 48 hours. The sacrificial glass backings were removed by soaking the backing in DI water at 70 °C overnight or for 24 hours at room temperature to dissolve the PAA.

Control "non-transferred" microraft arrays were fabricated without the use of a sacrificial rigid substrate, i.e. the array was maintained as a freestanding membrane throughout the microfabrication process as previously reported.[14] Briefly, after degassing Sylgard 184 over 1002-F master templates, the PDMS was spin coated to the desired thickness and then cured, demolded, dip coated, baked, and secured to media chambers as described above.

2.2.3 Deformation Measurements

Deformation measurements of the microraft array were taken using an image-based "shape-from-focus" (SFF) routine on a motorized Olympus IX81 inverted microscope (4× objective, N.A. of 0.13, Olympus UPlanFLN). SFF aims to determine the shape of the surface of an object by estimating the best-focused depth of images on a surface.[20] For microraft arrays, the correct focus can be derived using the defined edges of the microwell and microraft features as focal markers. Image-based SFF was performed by autofocusing on images of the microarray at each position of a (x,y) coordinate grid spanning the array. The software autofocus was implemented as a bounded maximization of the image gray-level variance as a function of focal position using MATLAB's *fminbnd* function (Optimization Toolbox).[21] SFF autofocusing scans were automated by MATLAB scripts harnessing the open-source Micromanager API for control of microscopy hardware. Deformation measurements were acquired at 0, 3, and/or 6 mL media loading within a controlled 60% humidity environment to minimize evaporation. With use of a 2.2 × 1.7 mm FOV, point clouds consisting of 23 ×14 spatial positions spanning the whole microraft array were recorded within 30 minutes with a measurement standard deviation of 7.2 μm along the

focal (Z) axis. For higher magnifications, the SFF measurement time and measurement error may limit the accuracy of the method. Modifications to reduce measurement noise, such as measurement averaging, may be required.

2.2.4 Tensile testing

Tensiometry of bulk PDMS was performed according to ASTM D 412 – 06a standards, with the exception of the shape of the dogbone samples, which was rectilinear. The dogbone shape consisted of an 8 mm long, 2 mm wide strip with 10 mm long, 12 mm wide gripping regions at either end. Bulk 3 mm PDMS was die-cut into dogbones and loaded into an EnduraTEC ELF 3200 load frame (Bose). PDMS dogbones underwent 20% strain at 1% s^{-1} rate without pre-loading or fatigue testing. The Young's modulus was calculated from the linear slope of the engineering stress as a function of strain. All Young's modulus measurements were taken at room temperature using at least 9 measurements per condition, which included between 2-4 technical and 2-3 experimental replicates.

2.2.5 Cell Culture and Staining

Microraft arrays were prepared for cell culture by air plasma treatment for 5 minutes and sterilization with 75% ethanol. H1299 non-small cell lung carcinoma cells previously transfected with eGFP (H1299-GFP) were seeded on microraft arrays at approximately 2,000 cells/cm^2 and cultured for 5 days in 1:1 fresh:conditioned RPMI media with 10% fetal bovine serum and 1% penicillin/streptomycin until the cells reached a density of approximately 5-10 per microraft. Chemical fixation was performed by rinsing the arrays twice with 1× PBS and incubating them with 1 mL 4% paraformaldehyde at room temperature for 20 minutes. The arrays with fixed cells were rinsed three times with 1× PBS, incubated with 1:250 Hoechst 33342 at room temperature

for 15 minutes, and then rinsed three times with PBS. Arrays with fixed and stained cells were stored and imaged in 1× PBS with 0.1% sodium azide.

2.2.6 Automated image acquisition and analysis

Microrafts arrays were scanned using custom MATLAB microscopy automation software controlling a motorized inverted IX81 microscope with open-source Micro-manager drivers. Fluorescence imaging of EGFP and Hoechst 33342 was performed using FITC (Semrock FITC-3540B) and DAPI (Chroma ET-DAPI 49000) filter sets. Microrafts and cells were segmented from brightfield and fluorescence images using a combination of intensity thresholding and morphological filtering. Cell nuclei were counted using peak finding ("Fast 2D peak finder" MATLAB File Exchange File # 37388) on images of Hoechst 33342 fluorescence intensity. This function performs 2D median filtering to reduce salt-and-pepper noise followed by smoothing, such that there is a high probability there will be only one pixel in each peak that will correspond to a true local intensity maximum.

2.2.7 Statistics

Measurements are reported as the average ± 1 sample standard deviation unless otherwise noted. All statistical tests were performed at the 5% significance level.

2.3 Results and Discussion

2.3.1 Membrane-based microarray deformation properties under an external load

The deformation of microraft array membranes under cell culture media poses a substantial barrier to imaging cytometry since different regions of the array will reside in different focal planes (Figure 2.2A,B). To investigate the extent of microraft array deformation, microarrays were fabricated using two previously reported microfabrication strategies and subjected to deformation tests.[18,22] In the first fabrication strategy, PDMS pre-polymer was spin-coated on the surface of a

micropost array template (Figure 2.2Ci). After curing, the PDMS mold with imprinted microwells was removed from the template (Figure 2.2Cii). To form the rafts or elements within the microwells on the PDMS membrane, the arrays were dipcoated into a polystyrene solution, and baked overnight (Figure 2.2Ciii). The completed microraft array was attached to a plastic media chamber with PDMS glue and aqueous solution was placed onto the array (Figure 2.2Civ,v). In a second strategy, the PDMS pre-polymer was spin-coated on the surface of a micropost array template but prior to curing, a glass slide with a surface coating of a sacrificial layer (polyacrylic acid) was placed onto the exposed PDMS (Figure 2.2Ci). The assembly was then cured with the sacrificial layer in contact with the PDMS (Figure 2.2Cii). After curing, the microwell-imprinted PDMS was removed from the micropost template but remained in contact with the PAA-coated slide (Figure 2.2Ciii). A media chamber was attached to the PDMS surface and then the sacrificial PAA layer was removed by immersing the assembly in an aqueous solution to dissolve the PAA (Figure 2.2Civ,v). Microarrays fabricated without the sacrificial layer ("non-transferred arrays") demonstrated a maximal transverse deformation of 1722 ± 89 μm (± 1 standard deviation, N=3) under an aqueous load (3 mL over a 24×24 cm^2 area). However, microarrays transferred to media chambers using the sacrificial substrate ("transferred arrays") exhibited significantly lower deformations with a maximal transverse deformation of 143 ± 10 μm (N=3, $p<10^{-5}$ by unpaired two-tailed t-test). Curing the arrays with identical geometry and comprised of an identical material (PDMS) over a sacrificial layer on a glass slide led to a substantial flattening of the array.

2.3.2 Thermally-induced mechanical tension as a mechanism for microraft array bending resistance

It was hypothesized that mechanical tension stored within the PDMS membrane during curing on the glass slide might account for the more than 10-fold reduction in deformation for the

transferred membranes compared to that of the non-transferred membranes. The reduction in deformation in transferred membranes was independent of microraft or microwell features. No statistically significant difference was observed between the deformation of transferred featureless PDMS membranes, transferred PDMS microwell arrays, and transferred microraft arrays (deformations: 129 ± 2 μm, 160 ± 22 μm, and 143 ± 10 μm, respectively, N=3, $p>0.08$ by one-way ANOVA). To assess the presence of stored tension in transferred microarrays, transferred microarray membranes were peeled from their media cassette and then the membrane and cassette were re-glued. The average deformation of the "peel-and-replace" microarrays increased significantly after releasing and replacing them onto their media chambers (from 143 ± 10 μm to 1085 ± 103 μm, N=3 per condition, $p<0.005$ by paired two-tailed t-test). A similar increase in deformation was observed in membranes that were released from their solid substrates during microfabrication and then re-transferred to cassettes (deformation of 1293 ± 301 μm, N=3, $p<0.003$ by unpaired two-tailed t-test). In contrast, the deformation of non-transferred microarrays was unaltered when peeled and replaced (from 603 ± 45 μm to 511 ± 112 μm, N=3, $p>0.14$ by paired two-tailed t-test). Taken together, these experiments indicate that tension is stored within transferred membranes and that this tension is stored prior to membrane transfer onto cassettes. Additionally, attachment to the cassette prior to release from the glass slide is critical to retain the stored tension.

Hypothetically, mechanical tension results from the thermal expansion of the PDMS array during microfabrication, and this tension is stored in the membrane of the transferred arrays but not in the non-transferred arrays. If so, tension would be introduced specifically during the thermal curing of the polydimethylsiloxane (PDMS) microarray (Figure 2.2Cii). As the liquid PDMS pre-polymer heats on a mold, the material thermally expands until it gels, at which point the solid

PDMS microarray is held in an expanded state by adhesion to the sacrificial glass backing. Once cooled, tension is stored within the microarray while adhered to its substrate. After the microarray is transferred to a media chamber and the sacrificial substrate is removed, the tension continues to be stored within the membrane.

2.3.3 Development of a thermal-tension model for thin microarray deflection

The proposed mechanism of thermal expansion-driven tension generation and storage in transferred arrays was mathematically modeled using linear membrane theory. The internal tension of the membrane, caused by residual thermal stresses from the manufacturing process, resists the deformation induced by the hydrostatic loading from the media (Figure 2.3A). The transverse deflection of membranes, plates, and shells has been well studied.[23,24] Governing equations and solutions are known for both steady state and non-steady-state deflection phenomena with a variety of model geometries, loading types, and boundary conditions.[25] For thin membranes undergoing small strains, three potential physical bending regimes have been described extensively: 1) no pre-tension, with deformation consistent with plate theory, 2) large pre-tension, with deformation consistent with linear membrane theory, or 3) negligible pre-tension, with deformation consistent with nonlinear solutions.[23] In the case of microraft arrays, pre-tension in the membrane is the dominant component of transverse bending resistance. The deflection of microraft arrays is resisted by both a material bending resistance and resistance due to thermally induced mechanical tension within the membrane. From plate bending theory, small deflection of thin rectangular plates can be generally modeled by combining the Germain-Lagrange and 2D Poisson equations. The transverse displacement $Z_m(x, y)$ of the membrane under tension T with flexural rigidity D subject to a constant downward pressure with magnitude P thus satisfies the partial differential equation

$$(2.1) \quad T\left(\frac{\partial^2 Z_m}{\partial x^2} + \frac{\partial^2 Z_m}{\partial y^2}\right) + D\left(\frac{\partial^4 Z_m}{\partial x^4} + \frac{\partial^4 Z_m}{\partial y^2 \partial y^2} + \frac{\partial^4 Z_m}{\partial y^4}\right) = -P.$$

Assuming that the material parameters are independent of temperature for the experiments, the membrane tension term can be estimated using the relationship

$$(2.2) \quad T = \frac{Eh\alpha\Delta}{1-\nu}.$$

where Δ is the difference between the membrane cure temperature and its temperature during deformation measurements, E is the elastic modulus of PDMS, and ν is Poisson's ratio of PDMS. h is the geometrically averaged thickness of the PDMS membrane, which for square microwells of side length s, depth d into the membrane of thickness t, and distance between adjacent microwells w is given by:

$$(2.3) \quad h = \frac{(t-d)(s)^2 + t\left((s+w)^2 - (s)^2\right)}{(s+w)^2}.$$

The flexural rigidity term is given by

$$(2.4) \quad D = \frac{Eh^3}{12(1-\nu^2)}.$$

Mathematically, tension dominates flexural rigidity when $\frac{TL^2}{D} \gg 1$, where the nondimensionalizing factor L is the width of the array. Substituting for D and T,

$$(2.5) \quad \frac{TL^2}{D} = \frac{12\alpha\Delta(1+\nu)L^2}{h^2} \propto \left(\frac{L}{h}\right)^2.$$

Microraft array membranes are very thin relative to their width ($\frac{L}{h} \approx 80, \frac{TL^2}{D} \approx 2300$). Thus, the flexural rigidity of the membrane was neglected and the transverse displacement $Z_m(x, y)$ of the membrane under tension T subject to a constant downward pressure with magnitude P thus satisfies the linear partial differential equation

$$(2.6) \quad T\left(\frac{\partial^2 Z_m}{\partial x^2} + \frac{\partial^2 Z_m}{\partial y^2}\right) = -P$$

with homogeneous Dirichlet (no-displacement) boundary conditions at the edges of the square membrane with side length L, which are $Z_m(0,y) = Z_m(L,y) = Z_m(x,0) = Z_m(x,L) = 0$. The average hydrostatic loading pressure due to the media of volume V was estimated as

$$(2.7) \quad P = \frac{\rho g V}{L^2}$$

where ρ is the density of the loading liquid and g is the acceleration due to gravity. The partial differential equation (2.6) with boundary conditions was solved using the standard separation of variables technique resulting in the double Fourier series solution for the displacement field

$$(2.8) \quad Z_m(x,y) = -\frac{16PL^2}{T\pi^4} \sum_{n\ odd}^{\infty} \sum_{m\ odd}^{\infty} \frac{\sin\left(\frac{n\pi x}{L}\right)\sin\left(\frac{m\pi y}{L}\right)}{mn(m^2+n^2)} \ .$$

The infinite sums (over the positive odd integers only) converge rapidly and thus only a finite number of terms are needed for high accuracy. The spatial structure of the deflection is dictated solely by the infinite sum, whereas the overall amplitude is determined a multiplicative pre-factor depending on the experimental conditions. Using equation (2.8), the maximum displacement is predicted to occur at the center of the membrane:

$$(2.9) \quad Z_m(0.5L, 0.5L) = W \approx -0.0737 \frac{PL^2}{T} = -0.0737 \frac{\rho g V(1-\upsilon)}{Eh\alpha\Delta}.$$

Equations (2.8-2.9) are expected to be accurate for small deflections of dominantly pre-tensioned PDMS membranes with small and shallow microfeatures relative to the membrane thickness. It should be noted that for thin ($h \leq 300$ μm) microarrays under high load ($V \geq 6$ mL of media), the membrane deformation is greater than the array thickness and the use of linear membrane theory for modeling these arrays may produce significant errors. For a given loading, the maximal deflection was predicted to be reduced linearly by increasing the membrane's curing temperature, thickness, or Young's modulus. The full solution describing the deformation of pre-tensioned membranes was also linear, with a multiplicative pre-factor. The linearity of the solution makes it

highly tractable for modeling, because only one parameter needs to be fitted to fully describe the shape of the microarray under various conditions.

2.3.4 Modeling parameters

Since the Poisson's ratio and linear thermal coefficient of expansion (CTE) of Sylgard 184 PDMS have been shown to be relatively constant, a Poisson's ratio of 0.5 and CTE of 265 ppm/°C were used for modeling all microarray membranes.[26,27] In contrast, the Young's modulus of PDMS varies with the crosslinker concentration and cure temperature.[28–31] PDMS cure extent was controlled experimentally by fully curing the PDMS in all conditions with 40-minute cure times. Tensile load testing was used to measure the Young's modulus of bulk 10:1 and 5:1 PDMS cured at 95 °C. The measurements of Young's modulus, 1.88 ± 0.21 MPa for 10:1 PDMS and 1.47 ± 0.12 MPa for 5:1 PDMS, agree well with literature reports from similarly cured PDMS.[29,32] Additional measurements of the Young's modulus of 10:1 PDMS cured at 150 °C and 10:1 PDMS cured for 48 hours at 95 °C (2.09 ± 0.11 MPa and 1.91 ± 0.24 MPa respectively) were not statistically different from that of 10:1 PDMS cured for 40 minutes at 95 °C, indicating that the PDMS in this study was fully cured.

2.3.5 Discussion of modeling uncertainty

Uncertainty in the material and geometric parameters of microraft arrays exists due to the nature of the microfabrication methods used to make microraft arrays as well as the measurement methods utilized to probe these parameters. The derived equation predicting the maximal membrane deflection of microraft arrays, equation (2.9) relies on several uncertain parameters. Some are known with high certainty; values for the loading liquid density ρ, gravitational constant g, PDMS Poisson ratio v, and PDMS coefficient of thermal expansion α are relatively precise in the literature. Others, such as the measured equivalent membrane thickness h had significant

variation. A summary of parameter uncertainty is presented in Table 2.1. An estimated propagation of uncertainty was performed under the assumption of no correlation between parameters and that all parameters are constant except E and h:

$$\sigma_{Z_m} \approx \sqrt{\left|\frac{\partial Z_m}{\partial E}\right| \sigma_E^2 + \left|\frac{\partial Z_m}{\partial h}\right| \sigma_h^2}. \quad (2.10)$$

2.3.6 Validation of physical model of microraft array deflection

The proposed linear model of thermally tensioned microarray deflection was validated by a measurement of the deformation of microraft arrays under different fabrication, material, and loading conditions (Table 2.2). The first condition consisted of microarrays made using standard conditions: PDMS at the standard 10:1 base:crosslinker ratio, molded into 300 μm thick membranes and cured at 95 °C. The remaining conditions increased the crosslinker concentration, membrane thickness, and/or cure temperature. Grids of positional data of the surfaces of microraft arrays in Condition 1-8 were measured using automated microscopy (Figure 2.3B, C, Figure 2.4). In these experiments, the standard transferred microraft arrays exhibited a maximal deflection of 153 ± 24 μm (3 mL of media load, curing at 95 °C, Condition 1, Table 2.2). Array deformation was further reduced to 94 ± 2 μm in microarrays cured at 120 °C (Condition 2) and to 52 ± 5 μm for 1 mm thick microarrays (Condition 4). Membrane cure temperature was confirmed as a parameter influencing the deformation of transferred membranes.

The shape of all measured microraft array deflections were highly consistent with model predictions (Figure 2.3C). For all 25 tested microarrays, the deflection increased by a factor of 2.00 ± 0.18 as the media load doubled from 3 mL to 6 mL, validating the predicted linear load-deflection relationship in equation (2.8). Linear changes in microarray deformation were also observed with effective membrane thickness as predicted (Figure 2.5A). Furthermore, the magnitude of microraft array deflection was highly consistent with that predicted by the model for

arrays made with 10:1 PDMS cured at temperatures below 150 °C (Figure 2.3D) using experimental and literature parameter values. For these 12 arrays, the average % absolute difference between measured and predicted maximal deflection was relatively low: 14% and 15% for 3 and 6 mL loading, or an absolute difference of 15 and 30 μm. For comparison, the estimated uncertainty in a prediction of maximal deformation was 19 and 37 μm for Condition 1 arrays under 3 and 6 mL liquid loads (Table 2.1).

In contrast, microarrays cured at temperatures at or above 150 °C or made from 5:1 PDMS deviated significantly from model predictions (Figure 2.3E). The average % absolute difference between measured and predicted deflection for these arrays (Conditions 6 -8) was 72% and 74%, or 73 and 151 μm, for 3 mL and 6 mL loading, respectively. Transferred microarrays cured at temperatures at 150 °C or 175 °C showed diminished returns in deflection resistance as temperature increased, which was not predicted by the model (Figure 2.5B). One likely explanation is that the PDMS membranes cured at high temperatures began to solidify before reaching the desired cure temperature so that they effectively cured at a lower temperature and stored proportionally less tension. Liquid Sylgard 184 PDMS sets (defined by 67% gelation) exponentially faster with increasing temperature, with previous reports indicating that similar PDMS membranes cured at 130 °C or lower when cured within a 150 °C environment.[33] Finite-element-modeling could potentially be used to compute effective thermal expansion temperatures. However, at cure temperature of 175 °C or greater, thermal degradation and stress defects in PDMS membranes were observed that might have further reduced the accuracy of the model under these conditions.

The deformation of PDMS microarrays with increased crosslinker ($\leq$5:1 base:crosslinker) was less than that predicted by the model. Increasing the crosslinker concentration to more than 1

part in 10 is not recommended by the manufacturer, and it has been suggested that at higher crosslinker concentrations, the crosslinker saturates the polymerization sites and forms void spaces within the PDMS which may cause tensile measurements of material stiffness to underestimate the effective material stiffness.[34,35] Indeed, the measured tensile modulus of bulk 5:1 PDMS was reproducibly and consistently lower than that of 10:1 PDMS in agreement with literature reports.[28,36–38] Yet, reports of PDMS modulus measured by other methods such as nanoindentation, compression, and buckling that are less sensitive to polymer orientation than tensile tests indicate a higher effective modulus.[38,39] In this scenario, it is likely that the strength of thin PDMS membranes lies in in the polymer network strength, and tensile measurements of Young's modulus are not always accurate predictors of holistic polymer network strength. Given the undefined nature of high-crosslinker PDMS, these microarrays were not modelled further.

Overall, the above validations demonstrate that the deformation of transferred microraft arrays was reduced in all cases by increasing the microarray thickness, cure temperature, or crosslinker concentration and that the deformation was accurately predicted for transferred membranes with 10:1 PDMS cured at or below 120 °C. It should be noted that changing the cure temperature of PDMS membranes has been shown to alter the crosslinking density and gas permeability through the material.[40] The optimal permeability of PDMS membranes to CH_4, N_2, and CO_2 has been shown to occur at cure temperature of 75 °C, with greater than 50% decreases in permeability at 150 °C. Nevertheless, for applications that do not require optimal gas transport, increasing the cure temperature of PDMS membranes while adopting a transferred membrane microfabrication method is an accessible way to reduce membrane deflection.

2.3.7 Reductions to microraft array deformation facilitate automated cytometry

To demonstrate the impact of large reductions in membrane deflection on automated image acquisition and analysis under realistic conditions, a deflection-resistant microraft array (Condition 9, Table 2.2) was seeded with H1299-GFP cells and subsequently imaged along a planar focal surface (Figure 2.6). The array exhibited a maximal deflection of 72 μm under the load of 6 mL of culture media. The appearance of images acquired along a planar surface from the deformation resistant array ranged from focused to visibly de-focused, with an average absolute defocusing of 43.5 μm. Quantitative image analysis successfully identified 85.5% of microrafts and exhibited a relative error of -2.7% in quantifying total cell nuclei compared to ground truth. In contrast, a control non-transferred array fabricated without stored tension deflected 1,427 μm resulting in an average absolute de-focusing of 400.0 μm when imaged along a flat plane, which allowed only 67.9% of microrafts to be identified. Of the in-focus microrafts on the non-transferred array, the total nuclear count was quantified with -62.0% error relative to ground truth. Overall, in these single-sample experiments the transferred membrane fabrication method reduced microraft array deformation by a factor of 19, resulting in a 23-fold improvement in the accuracy of basic cellular cytometry using automated imaging. However, even when paired with a high depth of field objective (4× magnification, NA = 0.13, depth of field (DOF) ≈ 40 μm), neither microarray had deformations small enough for microfeatures or adhered cells to be visualized in focus throughout the entire array along one focal plane.

2.3.8 Fitting deformation models to membrane shape data

While the deflection of microraft arrays can be significantly reduced with alterations to the material, geometric, and fabrication parameters, the minimum possible deflection magnitudes (around 50 μm) are still greater than the depth of focus of even the lowest magnification objectives

that are useful for image-based cell cytometry. A method capable of imaging along the curved focal plane of microraft arrays would improve the quality of the images. It is possible to determine the focal surface of microraft arrays by autofocusing at every imaging position. However, this tactic becomes unfeasible at magnifications above 4× due to the time required to autofocus with typical autofocus routines and microscopy hardware. With a focusing translation speed of 2 mm/s, stage translation speed of 7 mm/s, and image acquisition speed of 10 s^{-1}, the imaging times required to focus throughout a single 1 sq. inch microraft array at 4×, 10×, and 20× magnification are estimated at 0.4, 2.5, and 9.5 hours, respectively. Over these timescales, the media above the PDMS microarrays evaporates altering the load on the array. Not only does this prevent accurate deformation measurements but also leads to cell toxicity from the increased media osmolarity as the media evaporates over the prolonged analysis times. Thus a method was developed based on the physically-motivated tension model of deformation to rapidly predict focal positions throughout microraft arrays.

A series of parameters were added to the physical model describing membrane deflection in equation (2.8) to enable fitting to real-world microarray data. In practice, the precise material and geometric parameters of a given microarray is seldom known exactly. Furthermore, in optical assays, arrays are typically placed with small tilts and focal offsets relative to the measurement coordinate system of microscope stages. Essentially, sample measurements were fit to a deflection model with constraints placed upon the orientation of the microarray in space. A lumped-parameter approach describing the transverse displacement of microraft arrays was adopted to account for unknown material and/or geometric microarray parameters:

$$(2.11)\quad Z_m^{lumped}(x,y,A) = A\sum_{n\,odd}^{\infty}\sum_{m\,odd}^{\infty}\frac{\sin\left(\frac{n\pi x}{L}\right)\sin\left(\frac{m\pi y}{L}\right)}{mn(m^2+n^2)},$$

where the aggregate parameter *A* is a linear scale factor. Membrane tilts and offsets relative to the coordinate system of the microscope stage were compensated for by modifying equation (2.11) with a uniform planar offset to form the fitting equation

(2.12)

$$Z_m^*(x, y, A, x_0, y_0, z_0, a, b) = Z_m^{lumped}(x - x_0, y - y_0, A) + \left(z_0 + a \times (x - x_0) + b \times (y - y_0)\right),$$

where fit parameters x_0 and y_0 are the translations in x and y required to center the array and z_0, *a*, and *b* are the coefficients of a flat plane that de-trends the membrane onto the X-Y plane of the microscope stage. By considering membranes under no media load as flat planes, measured focal points $Z_m^{measured}(x,y)$ on the membrane of the microarray were fit to equation (2.12) in a least-squares manner:

$$\min_{A,x_0,y_0,z_0,a,b} \sum_{x,y} (Z_m^{measured}(x, y) - Z_m^*(x, y, A, x_0, y_0, z_0, a, b))^2. \quad (2.13)$$

The fitting minimization in equation (2.13) was implemented as an unconstrained multivariate minimization using MATLAB's *fminsearch* function.[41] Initial guesses of the fit parameters were $x_0 = y_0 = 0$, $z_0 = \max(Z_m^{measured}(x,y))$. Guesses for microraft array tilt angles *a* and *b* were produced from a least squares fit of a flat plane to the measured transverse displacement ($Z_m^{measured}$), and the initial guess for the deformation scale (*A)* was the range of tilt-corrected displacements (Z_m^*). The rapidly converging infinite sum in equation (2.11) was implemented using odd *m* and *n* from 1 to 25. The search tolerances were 0.001 μm^2 and 0.1 for the function value and fitting parameters, respectively.

A priori information about the microraft array spatial orientation can be incorporated into equation (2.13) to improve fitting robustness. The orientation information included array focal height on the microscope stage, array tilt angles, and the coordinate of the center of microraft array

deformation. When these parameters, symbolized as z_0, a, b, x_0, and y_0, respectively, were treated as constants in equation (2.13), the fitting equation was simplified to reducing the fit to a univariate minimization for the array deformation A:

$$(2.14)\quad \min_{A} \sum_{x,y} (Z_m^{measured}(x,y) - Z_m^*(x,y,A))^2.$$

The fitting minimization in equation (2.14) was implemented as a bounded minimization using MATLAB's *fminbnd* function.[21]

The measured, unfitted maximal deflection of the microraft arrays was estimated from focal point data as the difference between the highest and lowest point of de-trended measurements of the array surface position. The 95th percentile was used to estimate the highest and lowest positions in order to minimize the effect of for measurement noise on the estimate of maximal deflection.

2.3.9 Optimization of membrane shape data measurement density

The location and number of deflection measurements that are necessary to obtain an accurate prediction of deflection at all locations of a microarray membrane using equation (2.13) were investigated. A training set of microarray shapes was generated by measuring the deformations of four transferred microraft arrays (Condition 1) under 3 and 6 mL liquid load using a 23×14 measurement grid (approximately 0.6 measurements/mm^2). This training set was subsampled from 23×14 down to various measurements resolutions and patterns ranging from 9 to 57 points in size (Figure 2.7). Each subsampled pattern of measurements was fit to a deformation model using equations (2.11-2.13), and the resulting model was then used to predict the original 23×14 grid of microarray surface positions. The mean absolute difference between the original and interpolated data varied with the number and patterning of measurement points (Figure 2.7A). Averaging over 4 arrays with average maximal deflection of 330 μm, the difference between the

original and interpolated reached a minimum of 3.4% with 25 or more measurement points. A measurement pattern of 19 points, or 6% of the original 23×14 grid, was selected as an optimal tradeoff between speed and accuracy (Figure 2.8A "Pattern 1").

A disadvantage of the above approach is that the measurement pattern requires focal measurements spanning the entire microarray, and acquiring these measurements becomes more time-inefficient as the arrays scale in size. For the 2.3×2.3 cm microraft arrays in this study, about 13% of the time spent determining a focal surface was used translating the microscope stage between the 19 imaging points, which were on average 6.7 mm away from each other. This fraction of time would increase to ~40% for a hypothetical 10×10 cm array. Thus, more concentrated patterns of measurements were also of interest (Figure 2.8A "Pattern 2" and "Pattern 3"). Overall, *in silico* testing revealed diminishing returns on prediction accuracy with increased numbers of focal measurements.

2.3.10 Rapid determination of microarray imaging surfaces using the physical model

To assess the performance of this focal prediction method, automated microscopy and image analysis were used to acquire and analyze images of a microraft array that was scanned at focal positions predicted using three different focal measurement patterns (Figure 2.8). The first measurement pattern consisted of 19 points spanning the entire array ("Pattern 1"). The second and third patterns each consisted of a 5×5 grid of points concentrated at the center ("Pattern 2") or edge ("Pattern 3"). There was a 13-fold reduction in the time required to determine the focal positions for imaging of the microraft array using Patterns 1-3, compared to the time taken to run an autofocus routine for each of the 312 images prior to imaging ("ground truth" method). The median absolute focal differences were 12, 14, and 20 μm when imaging at focuses calculated from Pattern 1, 2, or 3 measurements, respectively, compared to imaging to the ground truth

method. Focus predictions using Pattern 1 measurements were the most precise, with 88% and 99.6% of the focusing errors less than 40 µm (1× DOF) and 80 µm (2× DOF), respectively (Figure 2.9). In all cases, the focal differences were small relative to the array's maximal deflection of 282 µm.

Automated image analysis was used to quantify the differences in the acquired images (Figure 2.10). 100% of the microrafts that could be identified in ground truth autofocused images could also be identified in images acquired at modeled focal planes based off Patterns 1-3. The median relative differences in individual microraft nuclear and cytoplasmic fluorescence areas between modeled and ground truth approaches were less than 4% for Patterns 1-3. A summary of the quantitative impact of modeling focal surfaces on cytometric analysis is presented in Table 2.3. For Pattern 1, the cell count per microraft was accurate for 80% of microrafts and <5% of microrafts erred by more than 1 count when on average there were 6.1 cells per microraft. Overall, accurate imaging cytometry was achieved on the arrays.

2.3.11 Rapid determination of microarray imaging surfaces using other shape models

The performance of other shape modeling approaches to enable cytometric microscopy in combination with transferred microrarrays was compared to that of the tension shape model. Thin plate splines, cubic interpolants, and biharmonic interpolants were used to calculate the focal planes for microscopic cytometry of the same array tested by the pre-tension shape model. Of these, only thin plate splines were able to fit data from Patterns 1-3 without massive prediction errors of focal positions outside the 10 mm working distance of the objective. Imaging using thin plate splines to predict focal points from Pattern 1-3 measurements resulted in 2-3 fold more error in cytoplasmic or nuclear area quantification and up to 3 fold more microrafts with errors in cell count greater than 1 cell compared to the tension model (Figure 2.11, Table 2.4). The use of

various interpolating splines to predict focal planes did not enable quantitative cytometry of cells on the microraft arrays, with accurate nuclear counts obtained for less than half the microrafts when using Pattern 3 and thin-plate splines.

2.4 Conclusions

Few options are available to modulate the deformations of membranes – especially in the case of microraft array membranes whose membrane thickness and material strength cannot be substantially modified while maintaining the microarray's functionality as a cytometry and cell sorting surface. Microfabrication methods can imbue thermal pre-tension into membranes, and storing this tension drastically reduced the deflection of microraft arrays. Thermal stress has been reported as problematic for microdevices in the contexts of membrane shrinkage and in warpage of thin electronics.[42,43] Instead, with membrane-transfer microfabrication, thermal membrane stress can be positively harnessed to consistently generate membranes with ≥10 fold more resistance to small loads of cell culture media. Using the membrane transfer microfabrication method, membrane curing temperature was demonstrated to become a novel parameter to linearly reduce deformation of pre-tensioned membranes. The linearity of the mathematical model facilitated computational fitting of theoretical deformation models to real-world shape data from membranes. The modeling approach was sufficiently accurate that microscopy images of thermally pre-tensioned microarrays acquired along the curved focal plane predicted by the model were well focused qualitatively and quantitatively. Storage of thermally induced tension in PDMS membranes does not impose changes to the membrane design geometry. The combination of 1) modeling the deformation of microarrays, and 2) microfabrication methods to store tension in membranes is of wide utility and extends to a variety of microdevices, sensors, and MEMS devices utilizing freestanding thin membranes.

2.5 Figures

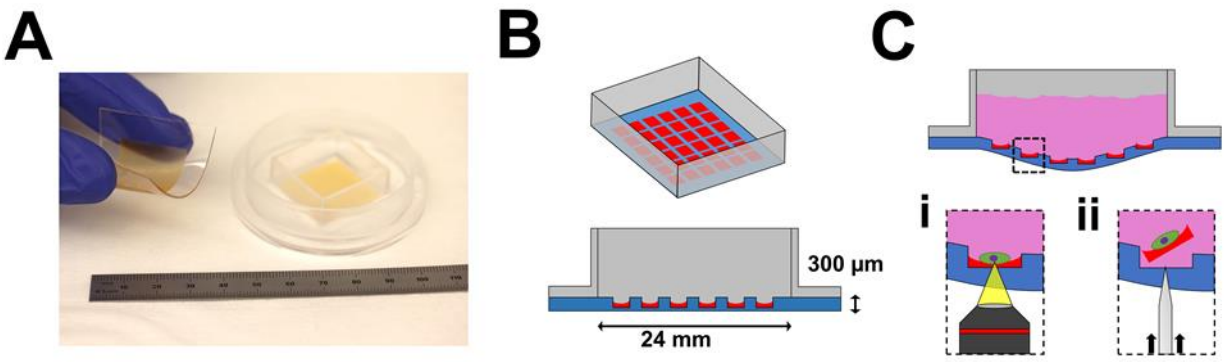

Figure 2.1 Introduction to microraft arrays. (A) Photograph of a freestanding microraft array membrane (left) and a finalized microraft array attached to a media chamber cassette (total ruler length shown = 11 cm). (B) Isometric view (top) and cut-away view (bottom) of a simplified schematic of a microraft array device (not drawn to scale). Approximately 12,000 microrafts, each 200×200×70 µm in size, are molded into a thin 24×24×0.3 mm PDMS membrane, which spans a square chamber. Microrafts: red; PDMS: blue; media chamber: grey. (C) The PDMS membrane deforms under the load of liquid media (pink). The two main functions of the microarray are microscopic cytometry (i) and cellular isolation (ii), which require access to the bottom of the membrane to position an objective near the array for imaging (i) or actuate a microneedle to dislodge microrafts for isolation (ii).

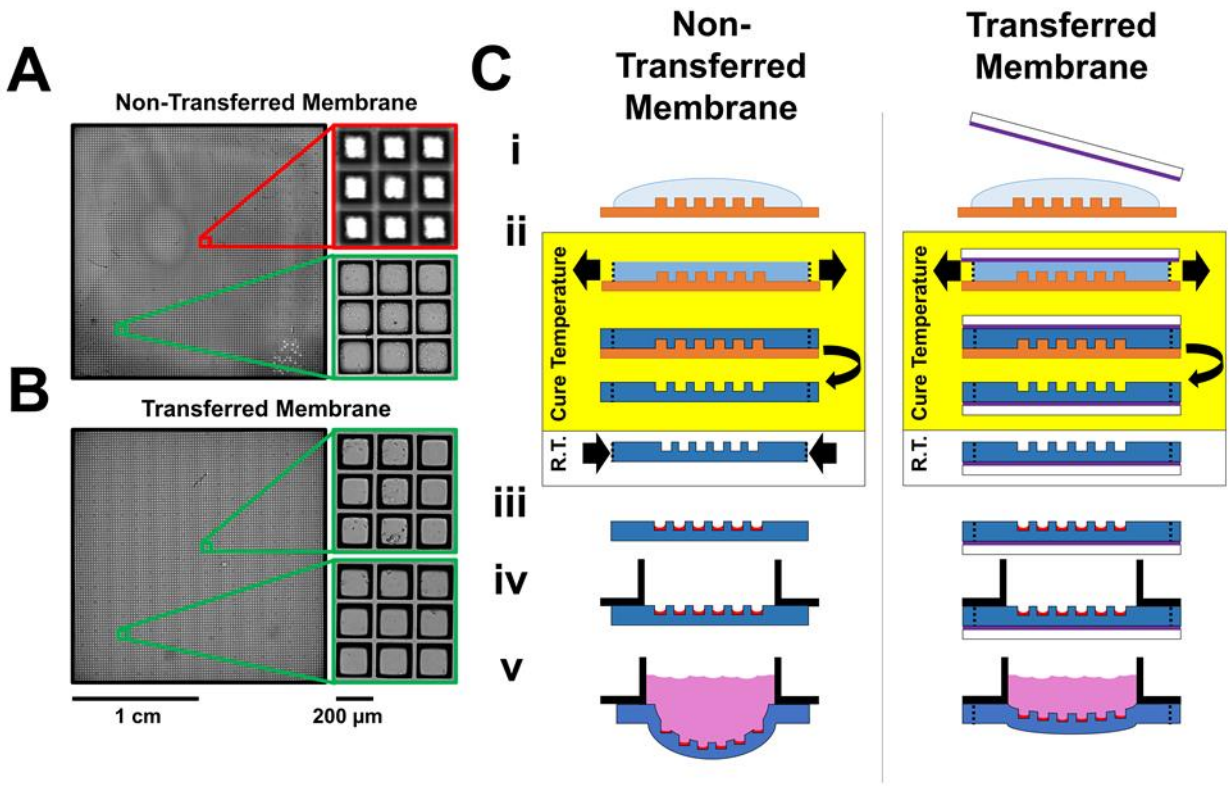

Figure 2.2 Deformability of non-transferred and transferred microraft arrays. (A-B) Transmitted light microscopy images of microraft arrays made from non-transferred (A) and transferred (B) arrays. The arrays were imaged in a single microscopy focal plane (4× magnification, NA = 0.13, DOF ≈ 40 µm). Red borders mark images visually judged to be out of focus while green borders mark images that were judged as in focus. (C) Schematic of non-transferred and transferred microraft arrays. i: PDMS (blue, darker shades indicate cured PDMS) is shaped with a micromold (orange). A glass slide (white) with a sacrificial coating (purple) is pressed onto the uncured PDMS for the transferred array fabrication strategy. ii: PDMS thermally expands prior to solidification, then shrinks after cooling (non-transferred) or remains expanded after cooling (transferred). iii: Microrafts (red) are microfabricated. iv: A media chamber (black) is glued to the array and for transferred membranes, the solid support is then removed. v: Aqueous media (pink) is placed onto the array.

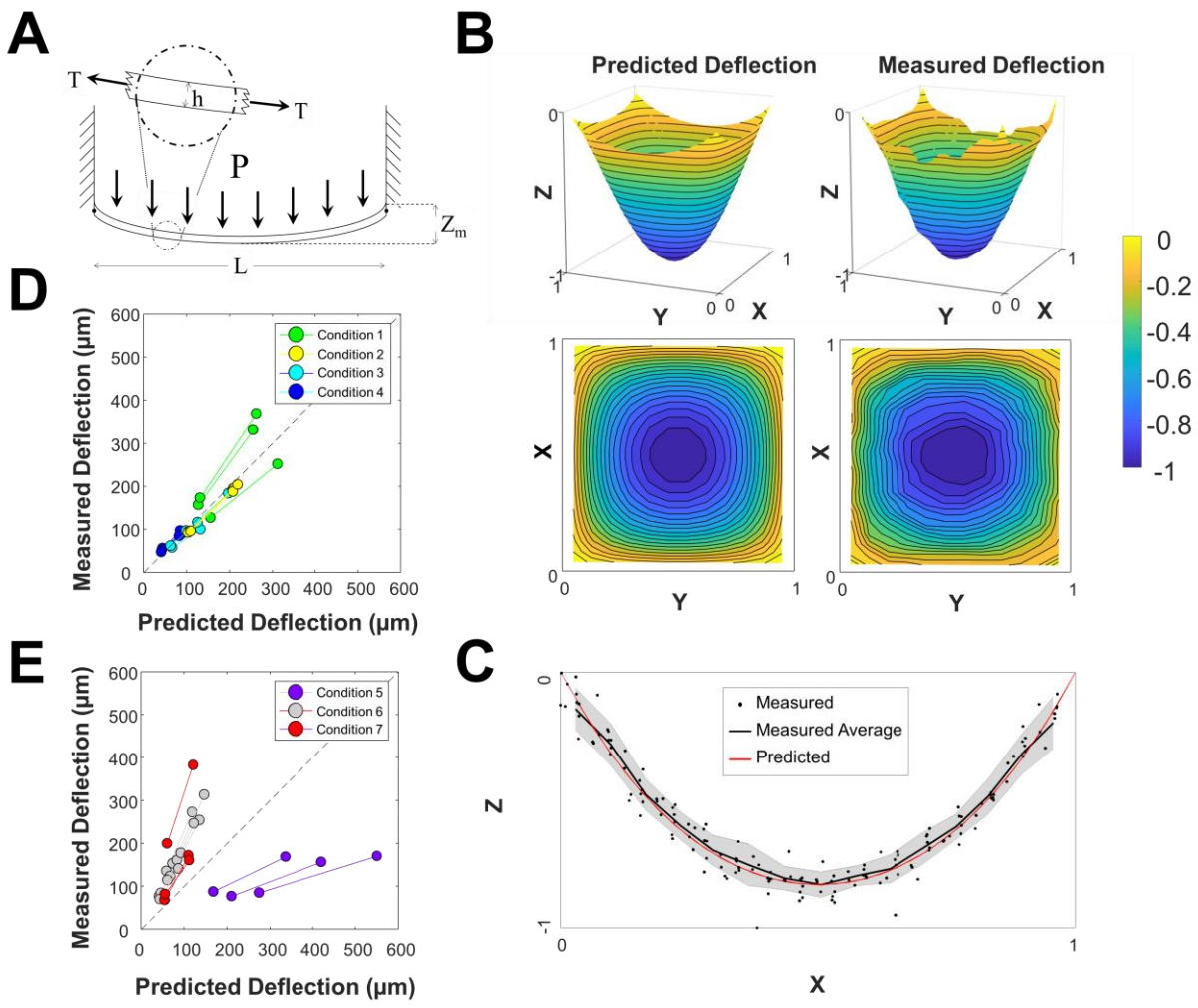

Figure 2.3 Validation of physical model of transferred microraft array deflection. (A) Free-body diagram of transferred microraft arrays (not to scale). Transferred microraft arrays were modeled as simply supported plates of side length L of homogenous thickness h under thermally-induced tension T with uniformly distributed load P. (B) Visualization of the predicted and measured shape of transferred microraft arrays. For visualization purposes, the X, Y, and Z dimensions were scaled to unit distances. (C) Measured and predicted cross-section of microarrays (N = 23 arrays). The grey-shaded region represents a single standard deviation of the experimental data. (D) Comparison of the predicted and measured magnitudes of maximal microraft deflection of microraft arrays for conditions 1-4 of Table 2.2. (E) Comparison of the predicted and measured

magnitudes of maximal microraft deflection of microraft arrays fabricated under conditions 5-7 of Table 2.2. The paired data points indicate paired deformation measurements recorded at 3 mL and 6 mL loading.

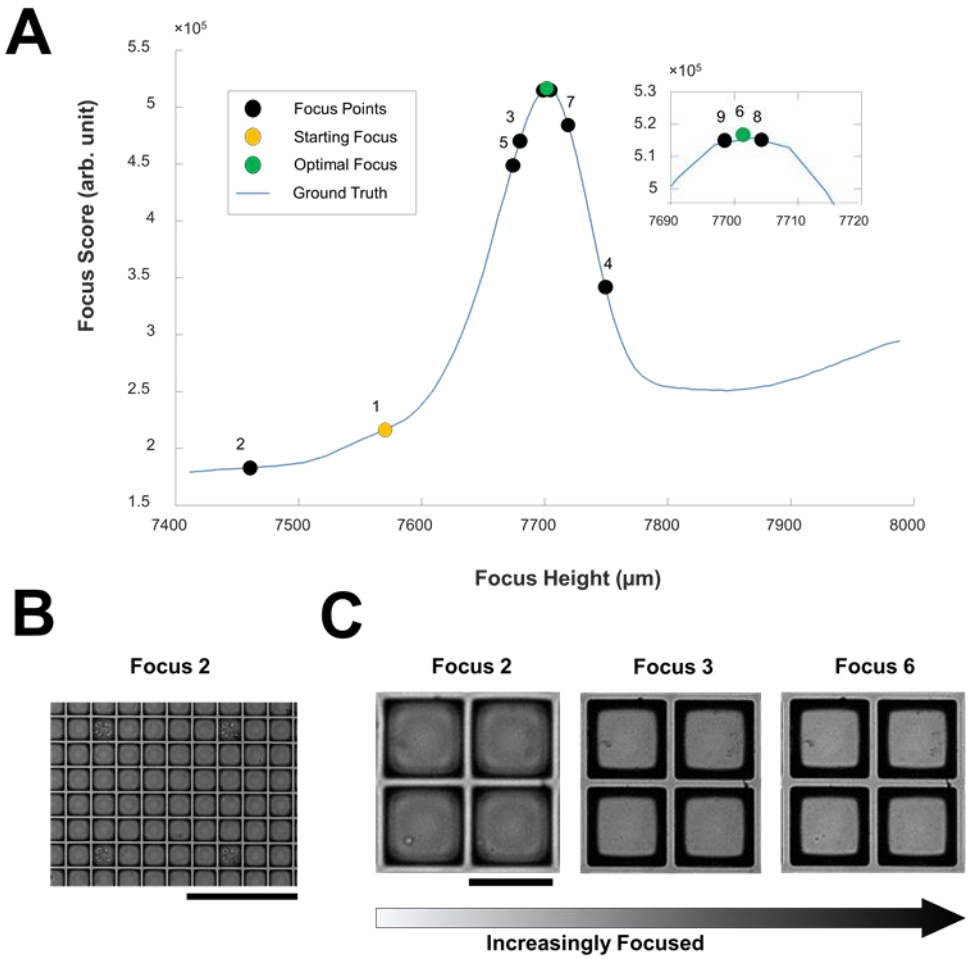

Figure 2.4 Example focal plane measurements of the microraft array surface. A microraft array was imaged in an initial plane (plane 1) in bright-field. The grayscale pixel intensity standard deviation ("Focus Score") was measured and then Brent's algorithm was used to determine the next plane for imaging.[21] This process continued iteratively until a maximal focal score was obtained at plane 6 when using a tolerance, or smallest allowable iteration step, of 2 μm. (A) Focal score *vs* the imaged plane is shown for an example autofocus process. The Y axis of 7400-8000 μm is the measured distance from the lowest position available to the microscope objective (0 μm). A high-resolution set of focus measurements taken every 4 microns is included for visualization purposes (blue ground truth trace). (B) A representative bright-field microscopy field of view

during focusing. Scale bar is 1 mm. (C) Cropped images at intermediate focal planes as well as the best focus plane showing 4 microrafts. Scale bar is 200 μm.

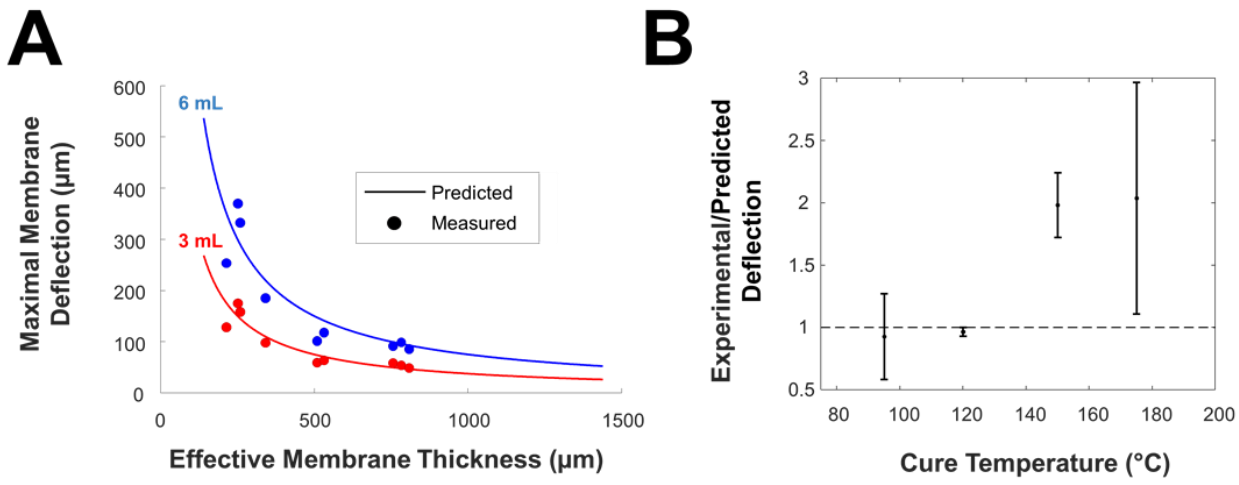

Figure 2.5 Modeling of the microarray deflection at various array thickness and cure temperatures. (A) Fold-difference between experimental and predicted microraft array deflection as a function of PDMS cure temperature for conditions 1-4 and 6-8 of Table 2.2. The dotted line represents agreement between measured and predicted array deformations. (B) Measured and predicted maximal microarray deflection as a function of PDMS thickness and volume of media placed onto the array for conditions 1, 3, and 4 of Table 2.2.

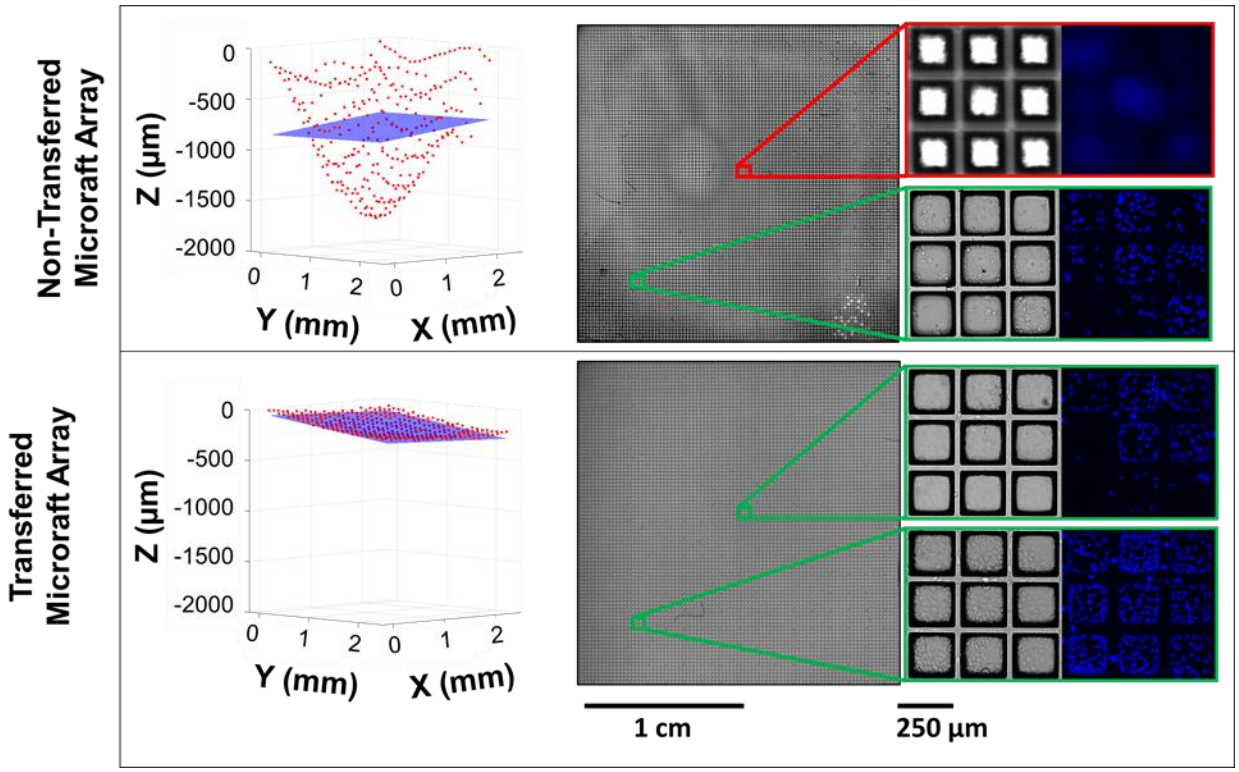

Figure 2.6 Comparison between transferred and non-transferred microraft arrays. (Left panels) Deflection (red) and imaging plane generated from a 1st order polynomial surface fit to the deflection (blue) of microraft arrays. (Middle panel) Widefield view of the microraft array. (Right panels) Bright-field and fluorescence microscopy of H1299 cells adhered to microrafts. Green: Visually judged to be in-focus; red: de-focused; blue: nuclear Hoechst 33342 fluorescence.

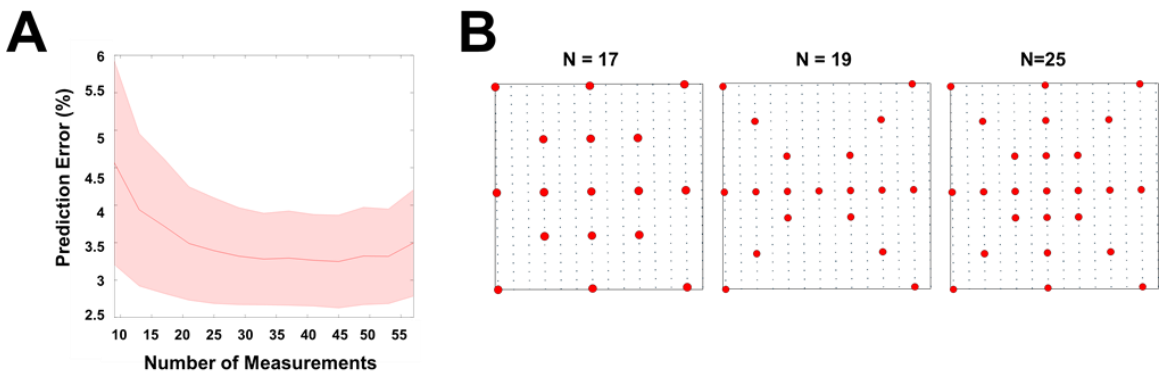

Figure 2.7 Determination of optimal number and pattern of measurements for surface modeling of microraft arrays. (A) The theoretical convergence to minimum error of shape fitting (Y axis) using a variety of patterns and different numbers of measured focal planes (X axis). The mean convergence percent is indicated by the red curve while the shaded error bars represent 1 standard deviation over n=4 datasets. (B) Representative patterns using 17, 19, and 25 measured focal planes are shown. Measurement points are in red, microraft array edges are in black, and the small black points represent all focal plane measurements contained in the datasets from (A).

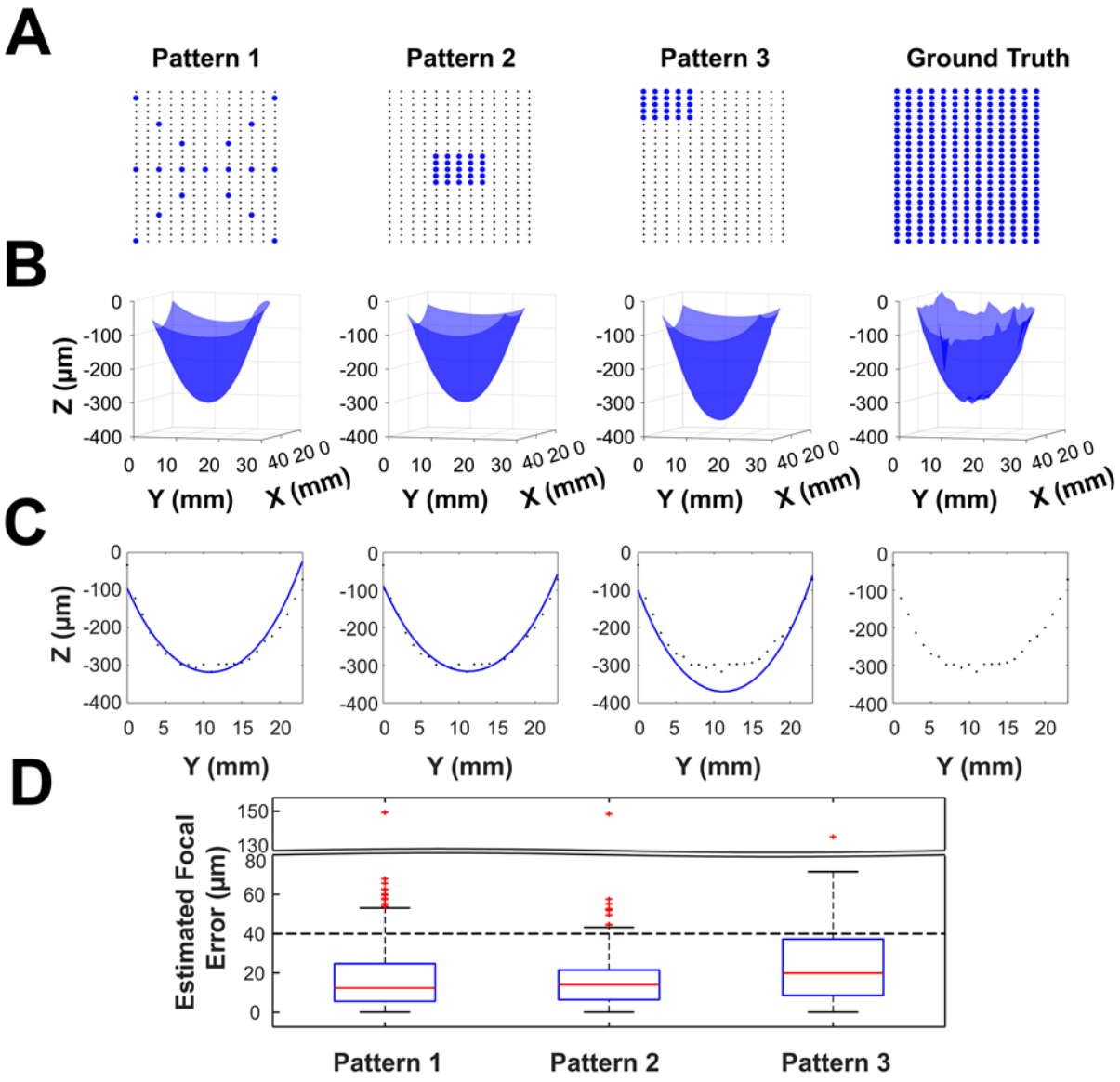

Figure 2.8 Fitting performance using different patterns of focal plane measurement. (A) Three measurement patterns for shape fitting, as well as a 322-point measurement used as ground truth. (B) 3D visualizations of shape models fit to the data and the ground-truth point clouds of focal measurements. (C) X-Z cross-sectional views of the shape fit (blue curve) though the array center. The black dots on each graph depict the ground truth focal measurement. (D) Differences, in microns, between the ground truth focal measurements and focal predictions using the thermal tension model. Dashed line represents 40 µm, 1× depth of field of the microscope objective.

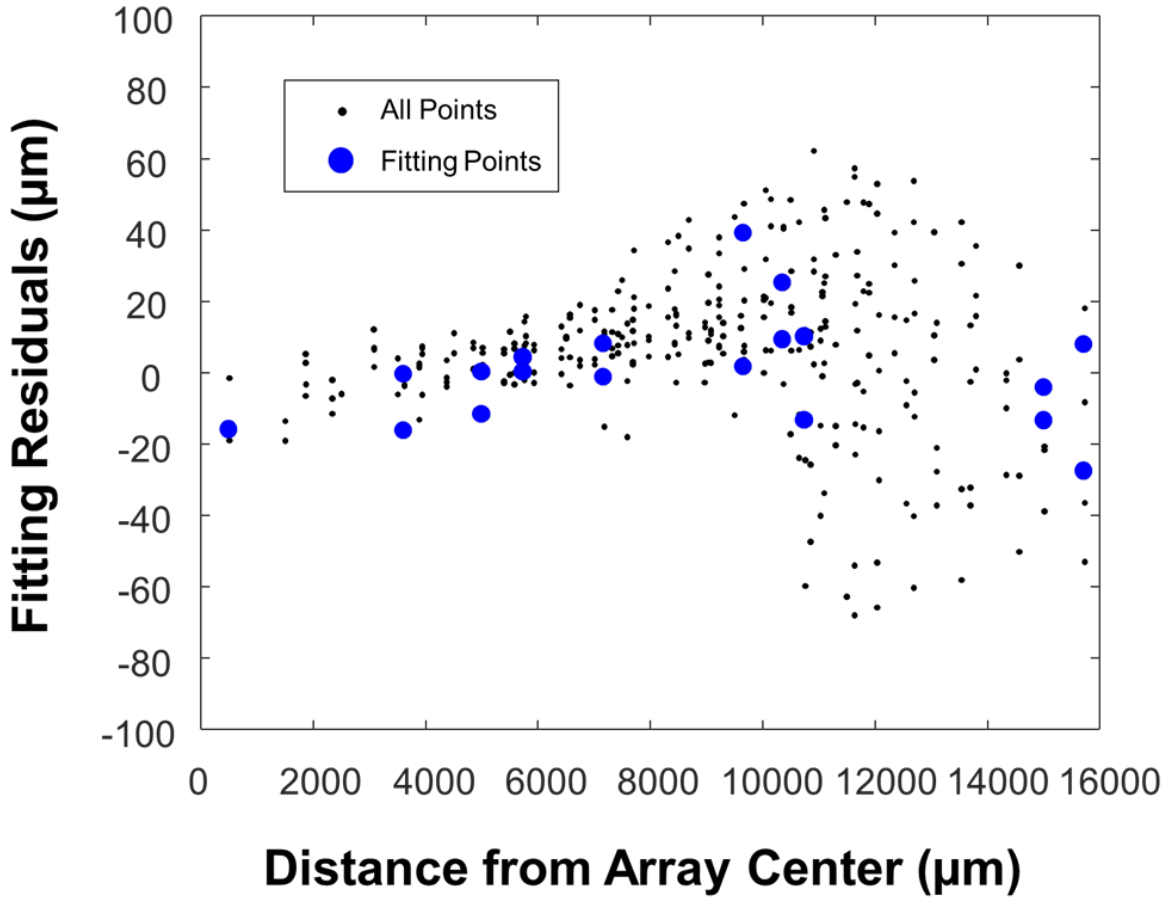

Figure 2.9 Fitting residuals. Shown are the residuals as a function of distance from the microarray center using Pattern 1 focal measurements to predict a 312-point grid of focus locations throughout a microraft array.

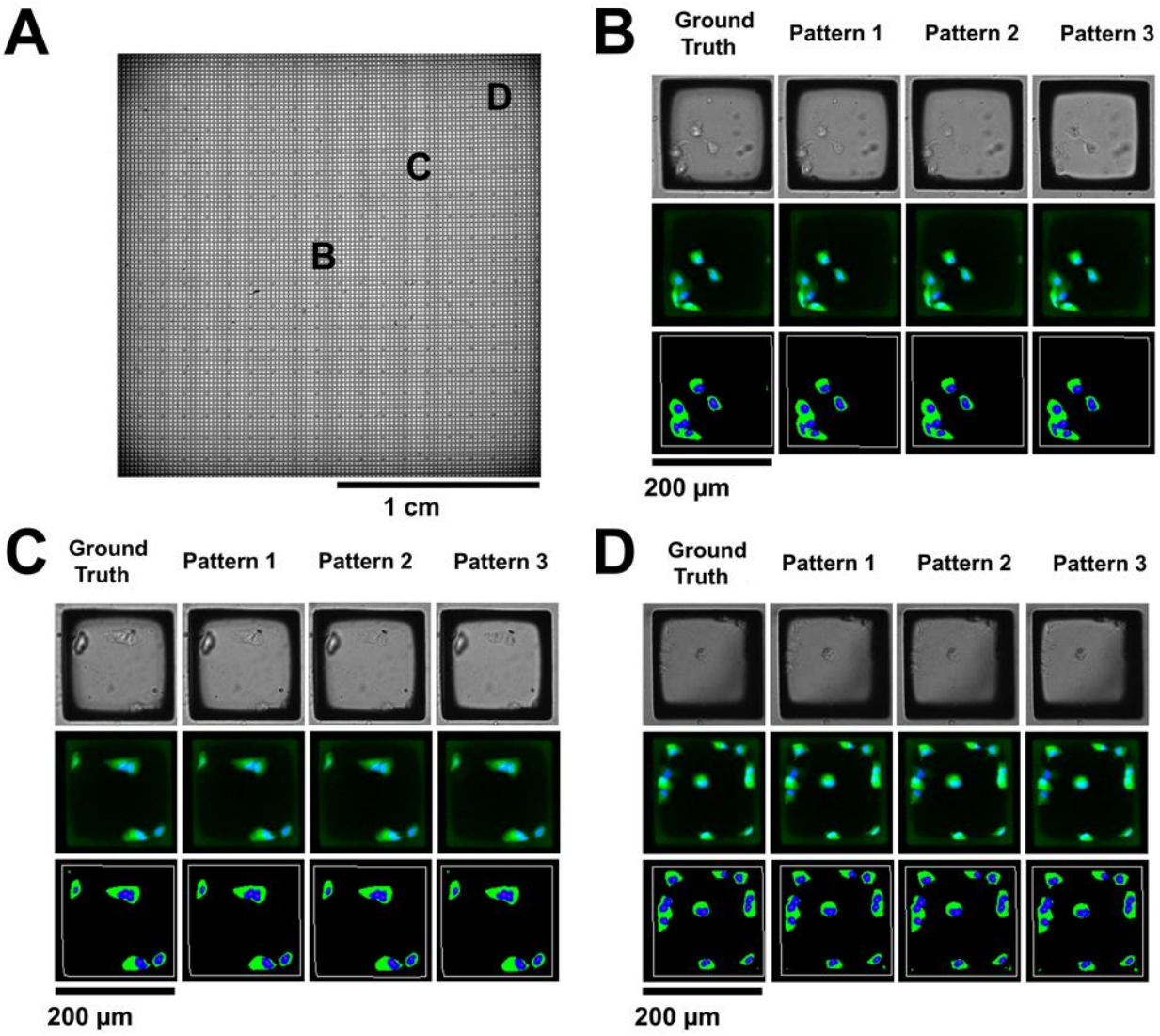

Figure 2.10 Application of physical model to automated cytometry. (A) Whole-array stitched bright-field image of a microraft array seeded with H1299-EGFP cells. (B-D) Images from select regions of the array as indicated in panel A. Close-up bright-field (top row) and composite fluorescence (middle row) images of representative individual microrafts are shown at the three locations. Green: cytoplasmic EGFP fluorescence. Blue: nuclear Hoechst 33342 fluorescence. Also shown are visualizations of identified microrafts (white outline), cell cytoplasm (green) and nuclei (blue) (bottom row) after analysis of the bright-field and fluorescence images.

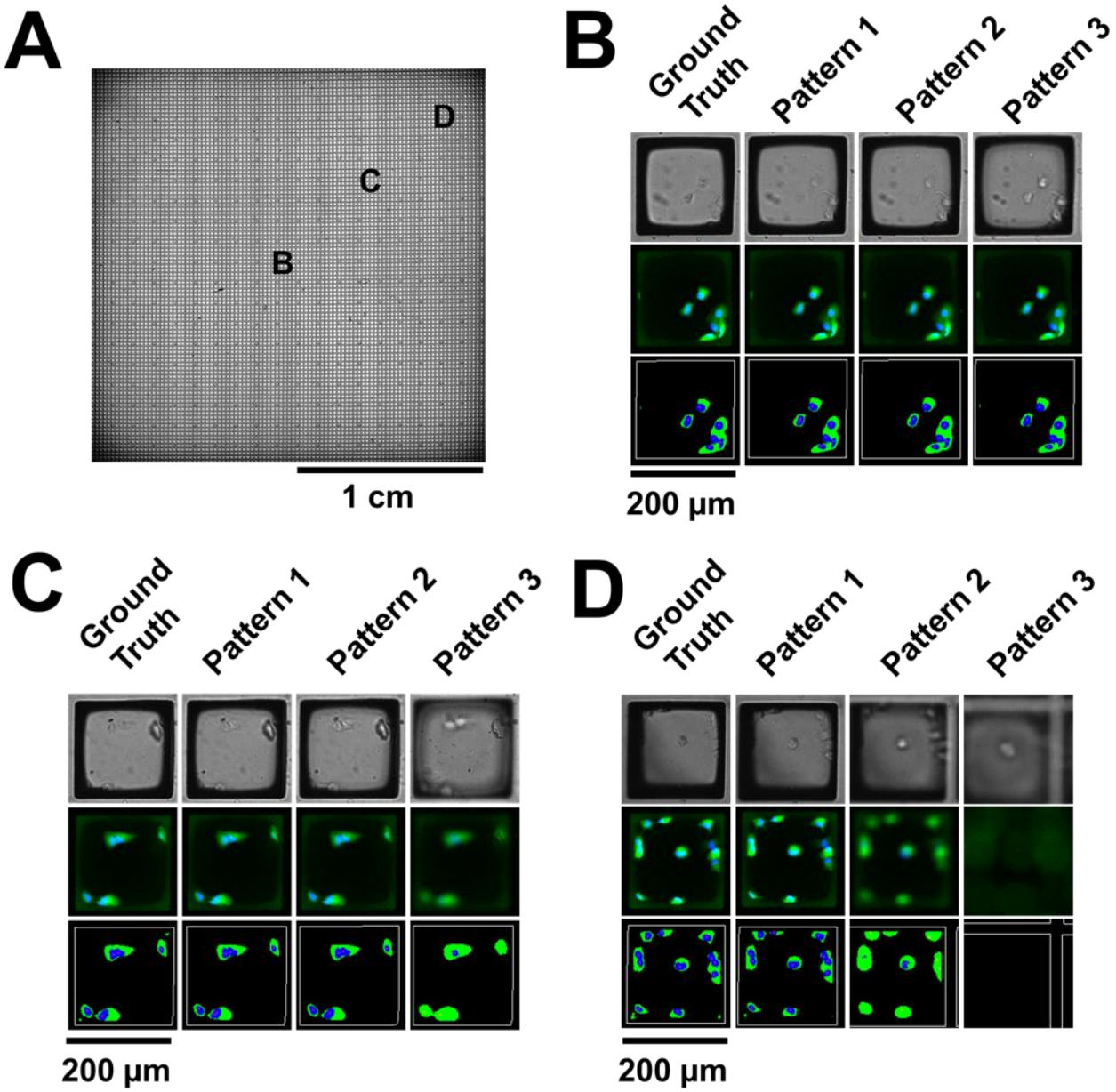

Figure 2.11 Application of gold-standard thin plate spline model to automated imaging. (A) Whole-array stitched bright-field images of a microraft array seeded with H1299-EGFP cells. (B-D) Images from select regions of the array as indicated in panel A. Close-up bright-field (top row) and composite fluorescence (middle row) images of representative individual microrafts are shown at the three locations. Green: cytoplasmic EGFP fluorescence. Blue: nuclear Hoechst 33342

fluorescence. Also shown are visualizations of identified microrafts (white outline), cell cytoplasm (green) and nuclei (blue) (bottom row) after analysis of the bright-field and fluorescence images.

2.6 Tables

Table 2.1 Uncertainty in modeling parameters.

Parameter	Value*	Standard Uncertainty	Relative Standard Uncertainty (%)
E	1.88 MPa	0.21 MPa	11%
h	264 μm	22 μm	8%
Δ	58 °C	2 °C	3%
V	3 mL	0.005 mL	0.2%
α	265 ppm/°C	~	~
ν	0.50	~	~
ρ	1000 kg/m^3	~	~
g	9.80665 m/s^2	~	~

*For a representative transferred array (Condition 1, Table 2.2)

Table 2.2 Transferred microraft array experimental conditions.

Condition	Description	Nominal PDMS Thickness (μm)	Temperature Difference (°C)*	PDMS Base:Cross-linker	Maximal Deformation** (μm)
1	Standard Conditions	300	58	10:1	153 ± 24
2	120°C Cure	300	83	10:1	94 ± 2
3	2× Thickness	600	58	10:1	72 ± 21
4	3× Thickness	1000	58	10:1	52 ± 5
5	2× Crosslinker	300	58	5:1	84 ± 6
6	150°C Cure	300	113	10:1	122 ± 32 (N=4)
7	175°C Cure	300	138	10:1	116 ± 72
8	150°C Cure, 2× Thickness	600	113	10:1	89 ± 23
9	2× Thickness and Crosslinker, 120°C Cure	600	83	5:1	72 (6 mL, N=1)
10	4× Crosslinker	300	58	2.5:1	111 ± 31
11	Non-transferred Array	300	58	10:1	1722 ± 89

*Difference between fabrication temperature and experimental temperature (37 °C)
**Mean ± standard deviation, N=3 and liquid load V=3 mL unless otherwise noted in parentheses

Table 2.3 Comparison of cytometry performance.

Focusing Pattern	Modeling Time (s)	Median Relative Absolute Error (%)				Microraft Analysis Efficiency (%)	Correct Cell Counts (%)	Incorrect* Cell Counts (%)
		Microraft Area	Cytoplasmic Area	Nuclear Area	Cell Count			
Ground Truth	1336.4	0.0	0.0	0.0	0.0	100.0	100.0	0.0
Pattern 1	101.3	0.5	1.1	2.0	0.0	100.7	79.7	15.7
Pattern 2	116.0	0.8	1.7	3.0	0.0	100.8	78.0	16.3
Pattern 3	109.0	0.9	2.2	3.4	0.0	100.4	73.2	19.8

*Error of 1 cell

Table 2.4 Comparison of cytometry performance using thin-plate spline modeling.

Focusing Pattern	**Modeling Time (s)**	**Median Relative Absolute Error (%)**				**Microraft Analysis Efficiency (%)**	**Correct Cell Counts (%)**	**Incorrect* Cell Counts (%)**
		Microraft Area	Cytoplasmic Area	Nuclear Area	Cell Count			
Ground Truth	1336.4	0.0	0.0	0.0	0.0	100.0	100.0	0.0
Pattern 1	101.3	0.8	2.7	3.1	0.0	101.5	74.6	18.7
Pattern 2	116.0	1.6	4.4	5.9	0.0	100.2	53.1	25.3
Pattern 3	109.0	1.6	6.8	9.0	12.5	93.5	43.2	24.6

*Error of 1 cell

2.7 REFERENCES

(1) Schneider, F.; Draheim, J.; Brunne, J.; Waibel, P.; Wallrabe, U. Characterisation of Adaptive Fluidic Siliconemembrane Lenses. *SAIEE Africa Res. J.* **2010**, *101* (1), 21–25.

(2) Palchesko, R. N.; Zhang, L.; Sun, Y.; Feinberg, A. W. Development of Polydimethylsiloxane Substrates with Tunable Elastic Modulus to Study Cell Mechanobiology in Muscle and Nerve. *PLoS One* **2012**, *7* (12), e51499.

(3) Nour, M.; Berean, K.; Griffin, M. J.; Matthews, G. I.; Bhaskaran, M.; Sriram, S.; Kalantar-Zadeh, K. Nanocomposite Carbon-PDMS Membranes for Gas Separation. *Sensors Actuators, B Chem.* **2012**, *161* (1), 982–988.

(4) Ma, T.; Liang, H.; Chen, G.; Poon, B.; Jiang, H.; Yu, H. Micro-Strain Sensing Using Wrinkled Stiff Thin Films on Soft Substrates as Tunable Optical Grating. *Opt. Express* **2013**, *21* (10), 11994.

(5) Peterson, S. L.; McDonald, A.; Gourley, P. L.; Sasaki, D. Y. Poly(dimethylsiloxane) Thin Films as Biocompatible Coatings for Microfluidic Devices: Cell Culture and Flow Studies with Glial Cells. *J. Biomed. Mater. Res.* **2005**, *72A* (1), 10–18.

(6) Chen, X.; Hou, S.; Chu, J.; Xiong, Y.; Xiong, P.; Liu, G.; Tian, Y. Observation Interface of PDMS Membrane in a Microfluidic Chip Based on One-Step Molding. *Micromachines* **2017**, *8* (3), 64.

(7) Fan, X.; Jia, C.; Yang, J.; Li, G.; Mao, H.; Jin, Q.; Zhao, J. A Microfluidic Chip Integrated with a High-Density PDMS-Based Microfiltration Membrane for Rapid Isolation and Detection of Circulating Tumor Cells. *Biosens. Bioelectron.* **2015**, *71*, 380–386.

(8) Ma, B.; Zhou, X.; Wang, G.; Dai, Z.; Qin, J.; Lin, B. A Hybrid Microdevice with a Thin PDMS Membrance on the Detection Window for UV Absorbance Detection. *Electrophoresis* **2007**, *28* (14), 2474–2477.

(9) Charnley, M.; Textor, M.; Khademhosseini, A.; Lutolf, M. Integration Column: Microwell Arrays for Mammalian Cell Culture. *Integr Biol* **2009**, *1*, 625–634.

(10) Jackman, R. J.; Duffy, D. C.; Ostuni, E.; Willmore, N. D.; Whitesides, G. M. Fabricating Large Arrays of Microwells with Arbitrary Dimensions and Filling Them Using Discontinuous Dewetting. *Anal. Chem.* **1998**, *70* (11), 2280–2287.

(11) Espinosa, H. .; Prorok, B. .; Fischer, M. A Methodology for Determining Mechanical Properties of Freestanding Thin Films and MEMS Materials. *J. Mech. Phys. Solids* **2003**, *51* (1), 47–67.

(12) Chrimes, A. F.; Khoshmanesh, K.; Stoddart, P. R.; Mitchell, A.; Kalantar-zadeh, K. Microfluidics and Raman Microscopy: Current Applications and Future Challenges. *Chem. Soc. Rev.* **2013**, *42* (13), 5880.

(13) Gach, P. C.; Wang, Y.; Phillips, C.; Sims, C. E.; Allbritton, N. L. Isolation and Manipulation of Living Adherent Cells by Micromolded Magnetic Rafts. *Biomicrofluidics* **2011**, *5* (3), 32002–3200212.

(14) Wang, Y.; Phillips, C.; Xu, W.; Pai, J.-H.; Dhopeshwarkar, R.; Sims, C. E.; Allbritton, N. L. Micromolded Arrays for Separation of Adherent Cells. *Lab Chip* **2010**, *10* (21), 2917–2924.

(15) Attayek, P. J.; Hunsucker, S. A.; Wang, Y.; Sims, C. E.; Armistead, P. M.; Allbritton, N. L. Array-Based Platform to Select, Release, and Capture Epstein-Barr Virus-Infected Cells Based on Intercellular Adhesion. *Anal. Chem.* **2015**, *87* (24).

(16) Welch, J. D.; Williams, L. A.; DiSalvo, M.; Brandt, A. T.; Marayati, R.; Sims, C. E.; Allbritton, N. L.; Prins, J. F.; Yeh, J. J.; Jones, C. D. Selective Single Cell Isolation for Genomics Using Microraft Arrays. *Nucleic Acids Res.* **2016**, *44* (17), 8292–8301.

(17) Attayek, P. J.; Hunsucker, S. A.; Sims, C. E.; Allbritton, N. L.; Armistead, P. M. Identification and Isolation of Antigen-Specific Cytotoxic T Lymphocytes with an Automated Microraft Sorting System. *Integr. Biol. (Camb).* **2016**, *8* (12), 1208–1220.

(18) Gracz, A. D.; Williamson, I. A.; Roche, K. C.; Johnston, M. J.; Wang, F.; Wang, Y.; Attayek, P. J.; Balowski, J.; Liu, X. F.; Laurenza, R. J.; et al. A High-Throughput Platform for Stem Cell Niche Co-Cultures and Downstream Gene Expression Analysis. *Nat. Cell Biol.* **2015**, *17* (3), 340–349.

(19) Wang, Y.; Phillips, C. N.; Herrera, G. S.; Sims, C. E.; Yeh, J. J.; Allbritton, N. L. Array of Biodegradable Microrafts for Isolation and Implantation of Living, Adherent Cells. *RSC Adv.* **2013**, *3*, 9264–9272.

(20) Krotkov, E. Focusing. *Int. J. Comput. Vis.* **1988**, *1* (3), 223–237.

(21) Brent, R. P. *Algorithms for Minimization without Derivatives*; Prentice-Hall: Englewood Cliffs, N.J., 1972.

(22) Xu, W.; Luikart, A. M.; Sims, C. E.; Allbritton, N. L. Contact Printing of Arrayed Microstructures. *Anal Bioanal Chem* **2010**, *397* (8), 3377–3385.

(23) Komaragiri, U.; Begley, M. R.; Simmonds, J. G. The Mechanical Response of Freestanding Circular Elastic Films Under Point and Pressure Loads. *J. Appl. Mech.* **2005**, *72* (2), 203.

(24) Timoshenko, S.; Woinowsky-Krieger, S. *Theory of Plates and Shells*; Engineering societies monographs; McGraw-Hill, 1959.

(25) Begley, M. R.; Mackin, T. J. Spherical Indentation of Freestanding Circular Thin Films in the Membrane Regime. *J. Mech. Phys. Solids* **2004**, *52* (9), 2005–2023.

(26) Lee, T. I.; Kim, M. S.; Kim, T. S. Contact-Free Thermal Expansion Measurement of Very Soft Elastomers Using Digital Image Correlation. *Polym. Test.* **2016**, *51*, 181–189.

(27) Mark, J. E. Polymer Data Handbook. Oxford University Press: New York 1999.

(28) Hocheng, H.; Chen, C. M.; Chou, Y. C.; Lin, C. H. Study of Novel Electrical Routing and Integrated Packaging on Bio-Compatible Flexible Substrates. *Microsyst. Technol.* **2010**, *16* (3), 423–430.

(29) Johnston, I. D.; McCluskey, D. K.; Tan, C. K. L.; Tracey, M. C. Mechanical Characterization of Bulk Sylgard 184 for Microfluidics and Microengineering. *J. Micromechanics Microengineering* **2014**, *24* (3), 35017.

(30) Khanafer, K.; Duprey, A.; Schlicht, M.; Berguer, R. Effects of Strain Rate, Mixing Ratio, and Stress–strain Definition on the Mechanical Behavior of the Polydimethylsiloxane (PDMS) Material as Related to Its Biological Applications. *Biomed. Microdevices* **2009**, *11* (2), 503–508.

(31) Liu, M.; Sun, J.; Sun, Y.; Bock, C.; Chen, Q. Thickness-Dependent Mechanical Properties of Polydimethylsiloxane Membranes. *J. Micromechanics Microengineering* **2009**, *19* (3), 35028.

(32) Schneider, F.; Draheim, J.; Kamberger, R.; Wallrabe, U. Process and Material Properties of Polydimethylsiloxane (PDMS) for Optical MEMS. *Sensors Actuators A* **2009**, *151*, 95–99.

(33) Wong, E. J. Modeling and Control of Rapid Cure in Polydimethylsiloxane (PDMS) for Microfluidic Device Applications. *Ph.D. Thesis* **2010**.

(34) Mata, A.; Fleischman, A. J.; Roy, S. Characterization of Polydimethylsiloxane (PDMS) Properties for Biomedical Micro/Nanosystems. *Biomed. Microdevices* **2005**, *74*, 281–293.

(35) Winter, H. H.; Chambon, F. Analysis of Linear Viscoelasticity of a Crosslinking Polymer at the Gel Point. *J. Rheol. (N. Y. N. Y).* **1986**, *30* (2), 367–382.

(36) Seghir, R.; Arscott, S. Extended PDMS Stiffness Range for Flexible Systems. *Sensors Actuators A. Phys.* **2015**, *230*, 33–39.

(37) Seo, J. H.; Sakai, K.; Yui, N. Adsorption State of Fibronectin on Poly(dimethylsiloxane) Surfaces with Varied Stiffness Can Dominate Adhesion Density of Fibroblasts. *Acta Biomater.* **2013**, *9* (3), 5493–5501.

(38) Wilder, E. A.; Guo, S.; Lin-Gibson, S.; Fasolka, M. J.; Stafford, C. M. Measuring the Modulus of Soft Polymer Networks via a Buckling-Based Metrology. *Macromolecules* **2006**, *39* (12), 4138–4143.

(39) Wang, Z.; Volinsky, A. A.; Gallant, N. D. Crosslinking Effect on Polydimethylsiloxane Elastic Modulus Measured by Custom-Built Compression Instrument. *Journal of Applied Polymer Science*. 2014.

(40) Berean, K.; Ou, J. Z.; Nour, M.; Latham, K.; McSweeney, C.; Paull, D.; Halim, A.; Kentish, S.; Doherty, C. M.; Hill, A. J.; et al. The Effect of Crosslinking Temperature on the Permeability of PDMS Membranes: Evidence of Extraordinary CO2 and CH4 Gas Permeation. *Sep. Purif. Technol.* **2014**, *122*, 96–104.

(41) Lagarias, J. C.; Reeds, J. A.; Wright, M. H.; Wright, P. E. Convergence Properties of the Nelder--Mead Simplex Method in Low Dimensions. *SIAM J. Optim.* **1998**, *9* (1), 112–147.

(42) Lee, S. W.; Lee, S. S. Shrinkage Ratio of PDMS and Its Alignment Method for the Wafer Level Process. *Microsyst. Technol.* **2008**, *14* (2), 205–208.

(43) Kim, C.; Lee, T.-I.; Kim, M. S.; Kim, T.-S. Mechanism of Warpage Orientation Rotation due to Viscoelastic Polymer Substrates during Thermal Processing. *Microelectron. Reliab.* **2017**, *73* (Supplement C), 136–145.

CHAPTER 3: AUTOMATED SENSING AND BIOPSY OF HUMAN INDUCED PLURIPOTENT STEM CELL COLONIES ON MICRORAFT ARRAY

3.1 Introduction

Induced pluripotent stem cells (iPSCs) are adherent cells that are of significant interest due to their potential to revolutionize research in disease modeling, drug screening, tissue engineering, and personalized medicine. *In vitro* iPSC generation, maintenance, and assay greatly rely upon the ability to sense the microscale location, growth, morphology, and health of adherent cells. Generally, this information is acquired optically with detectors varying from the human eye to scientific cameras and photomultiplier tubes (PMTs), and sensing modalities such as transmitted light, fluorescence, phase contrast, and differential interference contrast (DIC) microscopy. Most protocols recommend that daily transmitted or phase microscopy images of the iPSCs be obtained, from which an experienced individual can observe nuclear-to-cytoplasmic ratios, colony border definition, cellular compaction, apoptotic cells, and other morphologies.[1] In broad terms, these observations are used to assess the effects of experimental conditions and infer biological cell pluripotency and viability. Regular optical monitoring of iPSCs is key even in optimized culture conditions, because differentiated cells have the capability to cause a differentiation cascade in pluripotent cells and should be identified for removal at the earliest stage to maintain high-quality cultures.[2] Accuracy in iPSC sensing is critical, not only to ensure safety in clinical applications, but also to prevent failed cultures and reduce the costs of culture optimization.[3,4] Thus, detecting and characterizing iPSCs using optical data is crucial at all stages of iPSC culture.

A major challenge for iPSC applications is the inconsistency of iPSC cultures.[5,6] The lack of standardized protocols for iPSC culture and handling is a key source of inconsistencies and is due, in part, to the subjectivity of the interpretation of biological image data between individuals. Individual bias can arise when inferring holistic iPSC culture health from individual high magnification images. Furthermore, the expertise, labor, and time requirements are a barrier to continual monitoring of iPSCs. The inconsistencies in iPSC culture introduced by qualitative optical evaluation of iPSCs can be compounded by the use of commonly used iPSC splitting methods. Currently, chemical, enzymatic, or mechanical dissociation of a colony followed by the re-plating of each colony fragment into separate culture vessels, remains the gold-standard method for most iPSC applications. While chemical or enzymatic dissociation are generally quick and effective methods to generate fractions of a cellular population, these methods can perturb cells, can result in cytotoxicity or chromosomal abnormalities, and are unable to isolate fractions of cells with spatial and size specificity. [7–10] In contrast, cells can be mechanically dissociated from surfaces using cutting, scraping, and aspirating instruments with high cell viability and the ability to biopsy specific colony sections for isolation. However, even in experienced hands, mechanical dissociation methods are time intensive, low-throughput, and inconsistent.

Automated cell handling technologies coupled with computer vision can address the limitations of manual culture and colony splitting methods. Automated systems have the potential to vastly improve the throughput, precision, and consistency of iPSC sensing and handling while eliminating human bias. Computerized analysis enables precise and unambiguous analysis of microscopy data of biological samples.[11,12] Recently, methods have been reported to detect and classify patches of iPSCs from transmitted light microscopy data.[13,14] While these methods are sensitive to minute differences in colony shapes and textures, their robustness remains unexplored.

To date, various automated systems making use of image analysis have been reported for iPSC handling, such as tissue choppers, liquid handlers, laser micro-dissectors, and suction aspirators.[15–19] Yet, these systems generally rely on the use of phase contrast or fluorescence intensity-based methods to approximate the location of large iPSC colonies, and no system has demonstrated long-term label-free culture and handling of human iPSCs (hiPSCs).[20] With the dramatically increasing number of studies involving hiPSCs for clinical applications, there is a need for automated, unbiased approaches to the maintenance and handling of the cells.

One path for improvement for handling hiPSCs involves automated microtechnologies.[21,22] Microtechnologies have numerous advantages: low sample volumes, optical clarity, opportunity for control over *in vitro* culture environment, and wide customizability in design. Various microdevices have been developed for the propagation, differentiation, and analysis of stem cells.[23–26] One viable approach to splitting cells is to discretize the culture surface into individual, releasable elements. For example, micropallet arrays have been reported for several colony-splitting applications.[27–29] However, they require complex microfabrication, expensive lasers, and materials with unknown hiPSC compatibility and fluorescent labeling of cells. Overall, a method of performing large scale, gentle, automated hiPSC splitting with high efficiency, without the use of exogenous cellular labels, and with accessible technologies has not been demonstrated. In particular, microtechnologies for hiPSCs lack robust label-free automated sensing methods to track colony growth of cells adhered to microfeatures. The identification of colonies is a necessary and important precursor to automated colony biopsy.

Herein is described the development of a colony tracking method that is robust even with uneven backgrounds and shifts in sample position between time-lapse points. To demonstrate utility, this computer vision approach was applied to monitor hiPSC colonies in culture on

microraft arrays. Microraft arrays are microwell arrays with individually addressable, micromolded releasable magnetic culture elements.[30] Microraft arrays have previously been automated for the isolation of rare non-adherent cells.[31,32] An automated system was developed to detect and excise biopsies of hiPSC microcolonies growing on quad microraft arrays. Quad microraft arrays are specialized microraft arrays in which each microraft has been discretized into a 2×2 colony culture and biopsy site.[33] The main advances of the automated system involve the use of: 1) automated bright-field image analysis to guide the ejection of microrafts with adhered cells from the array; 2) quad microrafts to control colony spreading; and 3) the application of small forces to break cell-cell adhesions to split adhered colonies. The automation of this system was optimized for speed, accuracy, and robustness to be capable of performing 683 microraft releases (without cells) with >99% efficiency and 100% accuracy within 2 hours. With expanding colonies on the microrafts the system dislodged 231 colony biopsies in under 80 minutes with 97.5% efficiency which were subsequently harvested from the microarray for cell culture of highly viable colonies. This novel approach to sensing hiPSC microcolonies and automating microraft arrays extends to the sensing and biopsy on other microarrays.

3.2 Methods and Materials

3.2.1 Microraft array microfabrication

Microraft arrays with a cluster (‘quads’) of 4 microrafts per cluster were fabricated as previously reported.[33] Briefly, two-layered photolithography was employed to fabricate an array template. PDMS molds off the template produced microwell arrays, which were dip-coated in 9% m/m magnetic polystyrene and cured to form microraft arrays. The arrays were plasma treated for 5 min before being attached to polystyrene cassettes using PDMS glue. All arrays were transferred to the cassettes using the membrane transfer strategy previously reported.

3.2.2 Stem cell culture

HiPSCs (SC102A, System Biosciences) were cultured on tissue culture-treated cultureware coated with HESC-qualified Matrigel (Corning) according to the manufacturer's instructions. MTeSR-1 (StemCell Technologies) was used as the culture medium and was replaced daily for all cultures. Cells were passaged as multicellular clumps by dissociation with EDTA (Corning) at 500 µM or ReLeSR for 3-4 minutes at 37ºC. When culturing low numbers of cells (<10 cells/mm^2) on microraft arrays, up to 1:1 conditioned media:fresh media was used to enhance cell survival. Karyotype analysis of cells from the manufacturer indicated an impurity of about 10% female hiPSCs of unknown identity; thus, all hiPSCs used in this work were maintained under 10 passages from the manufacturer to ensure stability and reproducibility throughout the duration of the experiments. The SC102A cell line has since been discontinued.

3.2.3 Immunostaining

Cell viability was assessed by incubating cells in culture medium (30 min, 37ºC) with 0.16 µM Hoechst 33342 counterstain (Thermo Scientific) and 8 µM CellEvent Caspase-3/7 Green (Invitrogen) to stain apoptotic cells. Cell samples assessed for pluripotency were fixed with 4% paraformaldehyde (Sigma) pH 7.4 for 15 min and washed with 3% bovine serum albumin (BSA, Fisher Bioreagents). Cells were permeabilized using 0.5% TritonX-100 (Fisher Bioreagents) for 20 min and washed with 3% BSA followed by 7.5% glycine (Sigma) to ensure quenching of the fixative. Permeabilized cells were blocked with an immunofluorescence buffer [IFB; comprised of 0.05% Tween-20 (Sigma), 0.2% Triton-X 100, 1% BSA, and 0.05% NaN_3 (VWR)]. After 90 min, cells were incubated with 1:200 primary antibodies:IFB overnight at 4ºC. The primary antibodies included a human anti-Oct4 rabbit polyclonal and human anti-Tra-1-60 mouse monoclonal antibody (Abcam). After overnight incubation, cells were washed with IFB and

incubated with 1:500 secondary antibodies:IFB for 45 min. Secondary antibodies used included Alexa Fluor 647 anti-rabbit (Jackson ImmunoResearch) and Alexa Fluor 488 anti-mouse (Thermo Fisher). The cells were washed with 1× phosphate buffered saline (PBS, Gibco) and incubated with 0.16 μM Hoechst 33342 for 15 min. Stained cells were stored in 0.1% NaN_3 at 4ºC prior to imaging. Unless otherwise specified, solutions were prepared v/v in 1X PBS and incubation steps were performed at room temperature (25 ºC).

3.2.4 Microscopy

Imaging was performed using a motorized Olympus IX81 microscope with motorized stage (ASI MS-2000), motorized focus drive (Olympus), and camera (Hamamatsu Flash 4.0 V2). The microscope was situated within a plexiglass incubator that maintained a temperature of 37 ºC, with 60% humidity and 5% CO_2. All microscopy was automated using a MATLAB GUI that interfaced with the automated components using Micromanager's MMCore Java API.

3.2.5 Automated microraft release

A motorized microneedle device was utilized to dislodge microrafts as previously reported. The device used a stainless steel microneedle (8 mm total length, 100 μm sheath diameter, 500 μm taper length, and approximately 5 μm tip diameter) seated with epoxy in an acrylic window. The window was incorporated onto a cantilever that was actuated up and down by means of a stepper motor (Hayden Kirk). The mobile needle assembly was placed on an objective sleeve fitted to Olympus microscopes (24 mm diameter). The microneedle device was controlled using an Arduino Uno integrated circuit with a motorshield attachment (Adafruit) and was automated by MATLAB code using the Arduino software package to communicate to the Arduino by serial commands over USB.

For automated microraft release experiments, a 2” diameter, ½” thick N52 disk magnet (K&J Magnetics) was used to collect all biopsies. To illuminate the array during biopsy, an electroluminescent sheet (EL Luminates Inc.) powered by an inverter was used. MATLAB code was used for all hardware automation.

3.2.6 Manual Biopsy

A 30G ½ hypodermic needle was used to engrave grid lines into hiPSC colonies viewed under an inspective microscope. A 20 µL micropipette was used to aspirate sections of the colonies and transfer the biopsies to new culture vessels.

3.3 Results and Discussion

3.3.1 Development of a cell-growth array to support automated colony sensing and biopsy on a microscale format

Quad microraft arrays were fabricated that discretized colony growth sites into four 200 µm × 200 µm microraft surfaces (Figure 3.1). The microrafts were cup-shaped – flat and highly transparent in the middle but with steep rising walls at the edges (Figure 3.1 B-C). The microraft surface had a slope of 59.2 degrees from horizontal at the steepest, as measured from confocal microscopy cross-sections of rhodamine-doped microrafts. Due to their shape, these microrafts had high contrast at their edges under brightfield imaging, a feature with the potential to facilitate their automatic detection and the subsequent tracking of adhered cells. To encourage colony expansion within quads but delay growth outside of a quad, each of the microraft subunits within a quad were minimally separated by a 30 µm PDMS barrier and each quad was separated from others by 50 µm tall, 100 µm wide barriers (Figure 3.1 D-E).

3.3.2 Colony Growth Sensing and Tracking

The specific detection of adherent cells in brightfield microscopy images is inherently challenging. In contrast to fluorescence microscopy, transmitted light microscopy can have a significant, non-homogeneous background signal. When in focus, adherent cells have very low contrast due to their flatness on their culture surface; partially out of focus cells are bordered by a halo of signal. Adherent hiPSCs were detected from brightfield images using a combination of brightfield detection techniques (Figure 3.2).[34,35] First, the uneven microraft background was estimated and removed from each image. Second, a standard deviation projection was performed using background-subtracted images acquired from three different focal planes. The resulting images had high signal where cells were located, which allowed texture filters to identify cellular locations.

Microraft arrays are an inherently uneven background under transmitted light microscopy due to the dark borders of the microfeatures, well edges, cellular and material debris, defects, bubbles, and bulb variations. Large-scale variations in array illumination were estimated by 1) dividing the images into 200 × 200 μm segments, 2) setting all pixel intensities within each segment to the mean intensity of all the pixels within their segment, and 3) smoothing the result using a Gaussian filter with a smoothing kernel of 8 μm standard deviation. An illumination-corrected image was generated by normalizing each image by its Gaussian background and matching the mean intensity to a reference image (i.e. the initial time point image).

Each image of the microraft array was registered translationally and rotationally to its position- and focus- matched initial timepoint image using the single-step DFT algorithm (MATLAB File Exchange #18401) iterated over -0.5 to 0.5 degree angular rotations.[36] The microarray background was estimated as the illumination-corrected and registered initial timepoint

image of the array prior to seeding. Alternatively, a microarray background could be estimated from the average projection of the illumination-corrected and registered images from multiple timepoints of the array after seeding. After a pixelwise subtraction of the background, a pixelwise standard deviation projection (SDP) was used to increase the specificity of the signal from the cells. A top-hat background subtraction using a linear structuring element of 33 microns was used to remove the non-specific signal from microrafts, which appeared as straight lines in SDP images. While the SDP sensitively showed the position of objects on the microarray, the signal did not label the entire cell and could not segment contiguous sheets of cells by intensity thresholding. However, areas of the array with cells had markedly high texture compared to bare areas, which exhibited a homogenous signal in the SDP images. To quantify colony area, cell-covered surfaces were differentiated from bare array surfaces using a local entropy texture filter on the SDP images. A local entropy filter calculates the average amount of information within a local neighborhood with pixel intensities i and intensity probability p_i.

$$-\sum p_i \log p_i \quad (3.1)$$

To optimize this method, the three focal planes at which to image to acquire optimal SDP images were investigated. Brightfield images of hiPSCs were acquired at their plane of best focus and at 50 additional focal planes, spaced apart by 2 μm, above and below the surface. Each of the 220 combinations of 3 focal planes separated by at least 20 μm were used to construct an SDP image. Colony segmentations derived from intensity-thresholding of these SDPs were compared against hand-drawn colony segmentations for pixelwise accuracy. The optimal focal planes were identified from the mean of the top 10 focal plane sets to be z = [-129.4, -48.8 -0.5] ± [16.8, 20.9, 14.1] μm where z = 0 was the optimal focal plane of the brightfield image using a diagonal Laplacian focal method and negative values are downward.[37] Three focal planes, one above, one

below, and the last at the same focal plane of the sample, provided the most accurate SDP signal. For consistency, z = [-115, -57.5, 0] were the focal planes used for all experiments. To validate the optimized method, brightfield segmentations were compared against segmentations obtained from fluorescence microscopy of stained cells. The brightfield segmentation method had a true positive rate (sensitivity) of 87.4%, true negative rate (specificity) of 98.8%, accuracy of 97.9%, and precision of 86.0%.

With the use of the brightfield detection method, various quantitative culture data were extracted from an image data of hiPSCs (Figure 3.3). An array seeded with fragments of hiPSC tissue (on average 4 cells per fragment) was cultured for 7 days (2 days with Y-27632 Rock inhibitor) and imaged daily (Figure 3.3 A-B). Initially, the cells clumps adhered randomly throughout the array, with 15.5% and 13.3% of the array covered on microrafts and PDMS borders regions, respectively. After the removal of Rock inhibitor from the medium, cells were no longer able to grow on PDMS, which was reflected by an 8-fold greater increase in cell coverage over microrafts in comparison to increase in coverage over the PDMS in subsequent days of culture. Furthermore, the removal of Rock inhibitor allowed colonies on microrafts to begin to resume their normal compactness, which caused a dramatic reduction in array coverage to 6.8% on microrafts and 0.4% on the PDMS (Figure 3.3 D). After one day recovering from the lack of Rock inhibitor with less than 15% increase in array coverage, the cells began to rapidly divide and expand over microrafts. The array coverage increased exponentially with a doubling time of 29 hours. For culture days 4-7, >70% of the colony growth occurred on microrafts (as compared to the PDMS surface). Colonies that filled their microraft began to expand over the PDMS to adjacent quads. One day 5, 6, and 7 of culture, 5.8%, 23.8%, and 60.1% of microrafts with colonies had expanded outside of their quad. These colonies covered >90% of their underlying microraft

surfaces on average. HiPSC colonies expanded rapidly over the arrays and by 7 days of culture, the majority (57%, or 427 out of 745) of colonies spanned 2 or more microrafts (Figure 3.3 C).

3.3.3 Evaluation of HiPSC Culture on Quad Microraft Arrays

The health of iPSCs in culture on quad microraft arrays was investigated as a prerequisite for effective colony biopsy. HiPSCs passaged as clumps of cells onto Matrigel-coated quad microraft arrays rapidly grew and expanded over microraft culture sites. HiPSCs on microraft arrays expressed Oct4 (97.8 ± 4.3%) and Tra-160 pluripotency markers (Figure 3.4 A). 3.6% of cells on the microarray were Caspase-3/7^{+} (a marker of early apoptosis) compared to cells on standard cultureware with 0.76 ± 0.20% (N = 3 biological replicates) of Caspase-3/7^{+} cells.

3.3.4 Biopsy of HiPSCs using quad microraft arrays

Quad microrafts without adhered cells released similarly to previously reported microrafts when dislodged by a microneedle. On average, quad microrafts required 1.23 ± 0.57 (N=30) microneedle actuations to be fully dislodged compared to the 1.27 ± 0.45 actuations for previously reported, 200×200μm microrafts. One average, the quad microrafts traveled 4.1× more slowly towards a magnet which can be attributed to the small mass of quad microrafts compared to the previously reported standard (approximately 20 μm *versus* 40 μm). Nevertheless, however, there was a 100% efficiency in releasing quad microrafts from the array using a microneedle and subsequently collecting them using a magnetic wand.

Microrafts bearing cells were released using a motorized release device that was manually aimed at microrafts using a stage joystick. In all cases, microrafts were released from the array with its primary cell-load adhered to the microraft. Colonies were broken along microraft edges if their cells extended off the microraft (Figure 3.5 A). Microrafts with large sheets of outgrowing cells on multiple sides were difficult to release, and were largely impossible to remove without

dislodging adjacent microrafts and cells. To improve upon this, the array was incubated in EDTA for 4 minutes to diminish cell-cell adhesion prior to biopsy. Unexpectedly, the EDTA preferentially also weakened the cell-PDMS adhesions so that cells on the PDMS were detached from the array during this process. Cells on microrafts were not released suggesting that the adhesions to the Matrigel-coated polystyrene was significantly stronger that for PDMS. Based on these results, the possibility of removing the cells attached to the PDMS from the array prior to biopsy using EDTA was promising. To accomplish this, hiPSCs in culture on a microraft array at day 6 of culture were treated with EDTA for 6 min, followed by 3x flushing with DMEM/F12 media or gentle scraping. Quantitatively, the cellular area was reduced by 60.4 ± 26.4% on the PDMS outer borders (N = 472 borders with >75% initial coverage), and 17.6 ± 31.8% on the microrafts (N = 1316 microrafts with >75% initial coverage).

The self-renewal, pluripotency, and viability of biopsies removed from arrays was investigated. Biopsies from the microrafts adhered to fresh Matrigel-coated polystyrene dishes and expanded rapidly with high yield and quality (Figure 3.5 C). Expanded and passaged colonies from microraft biopsies, expressed Oct4 and Tra-1-60 (Figure 3.5 D). Immediately after biopsy, a small quantity of caspase-3/7^{+} cells were found at the microraft periphery (2.99% +- 2.53%, N = 3), indicating a small amount of apoptotic cells at the biopsied edge (Figure 3.5 B). In comparison, when the hiPSCs were cut using a hypodermic needle, 7.56% ± 3.33% (N = 5) and 7.89% ± 1.35% (N = 6) of cells were caspase-3/7^{+} in the biopsy and mother colony, respectively, compared to a background of 1.90 ± 1.14% of unmanipulated cells within the same culture and 0.29% ± 0.25% of cells from unprocessed cultures (Figure 3.4 B). A two-way ANOVA with multiple comparison testing found that, overall, cells in the microraft biopsy group had statistically significant lower caspase-3/7^{+} cells than cells in the mechanical biopsy group ($p<0.01$). Specifically, the population

marginal mean caspase-3/7 staining was statistically significantly higher in both the mother and daughter colonies cut manually than in unmanipulated cells on the microraft array ($p<0.01$ for both comparisons). No other statistically significant differences were found between group. These results indicate that mechanical splitting of colonies induces cell apoptosis above background levels, whereas microraft biopsy resulted in low amounts of cell death and produced highly viable, pluripotent colony splits.

3.3.5 Automated microraft isolation system

An automated system was developed consisting of a quad microraft array culture and biopsy platform arranged on the stage of a motorized microscope (Figure 3.6). To enable rapid microraft collections, ejected microrafts were collected into a capture plate situated directly above the array using a powerful disk magnet. To provide visual feedback to the automated system, an electroluminescent sheet was incorporated between the magnet and array to illuminate the array for image acquisition of microrafts during isolation. Lastly, a motorized microneedle was sleeved around the microscope objective for automated microraft release.

The automation began by determining the position of the microarray on the stage. Of utmost importance was determining the focal planes required for high-quality microscopy of the array. Thus, the system first rapidly generated a model of the microraft array shape using previously reported autofocus routines.[38] Using this model, the system was able to effectively focus on all positions of the arrays using a 4× objective. Roughly every 15 minutes, the system acquired new focal data to update the model and compensate for drift microarray deformation (i.e. due to evaporative loss of media from the array).

Next, the system scanned the array under brightfield microscopy and located all visible quad culture sites on the microarray using automated segmentation. To maximize speed, microraft

segmentation was performed in parallel with image acquisition. Briefly, after Otsu's intensity thresholding of the dark borders of microrafts, a series of morphological processing was performed on each image to remove cells, debris, and other anomalies from the microraft segmentation (Figure 3.7 A). [39] The individual microraft locations within a quad were inferred from the quad segmentations. The microraft segmentation was robust and was not significantly impaired by the presence of cell colonies, with >99.5% of microrafts detected even when overgrown with dense hiPSC colonies. Lastly, each microraft was assigned a unique ID number, in the form (Row#, Column#), to enable individual microraft tracking over different days. Since the microrafts are not situated in a perfect grid but rather a distorted one, an algorithm was developed to assign the identities to microrafts. The algorithm determines the angle of the array, and traces rows and columns across known microraft locations using morphological processing (Figure 3.7 B). The result is free from missing microrafts, and starting from the lop left coordinate, the grid is crawled through until all possible identities are assigned. To link identities despite shifts in the arrays coordinates, user feedback on the array offsets was queried by a GUI. To demonstrate the robustness of the identification process, fractions of the known microraft locations were removed randomly. The identifier with user input correctly assigned unique ID#s to >96% of microrafts with up to 56% of the rafts removed from the array.

With the 4-dimensional (X, Y, Z, and-time) coordinates of microrafts known, the system optimized the order of the targets to minimize the total travel distance. While this optimization has no deterministic solution, strategies exist to simply achieve relatively optimized paths. The nearest neighbor algorithm (NN), for example, provides a solution by iteratively determining and traveling to the closest target. While recently reported algorithms, such as genetic algorithms, can provide significantly more optimized paths, their computation time is approximately minutes to hours for

large datasets. Thus, a random nearest-neighbor search pattern (MATLAB File Exchange # 35488), raster scan pattern, and random pattern were investigated in the context of microraft arrays (Figure 3.8). For a hypothetical microarray with a grid of 40 × 40 quad culture sites, random lists of target microrafts were chosen and the order of the list was optimized by each algorithm. When releasing a fraction of the microrafts on the array, the nearest neighbor algorithm was up to 4.03× shorter than raster and 7.79× shorter than random pathing. To release 1% (64 microrafts), total travel distances of 0.71, 0.46, and 0.15 meters was required, with a total traversal time of 103.94 s, 80.42 s, and 31.86 s (stage linear translation speed of ~6 mm/s) (Figure 3.8 B-C). Thus, nearest-neighbor ordering was utilized for all automated microraft release experiments.

The automated system next proceeded to aim a microneedle at each target microraft to attempt to dislodge it from the microarray (Figure 3.9). The microneedle release process was iterative: each attempt, the system re-located the microraft before repositioning the microneedle for release. The process continued until <20% of microraft material was detected within the microwell, or until 8 attempts were performed. Because the microraft array is based on a thin, flexible PDMS substrate, there was some play when puncturing the membrane. Thus, needle puncture depth was increased closer to the center of the array (Figure 3.9 A).

3.3.6 System Characterization

To demonstrate the precision and throughput of the release process, 683 microrafts were released from an array in the pattern of university logos (Figure 3.10). There was >99% efficiency of correctly released microrafts, with 0% of off-target microrafts released. An average of 1.89 ± 0.04 ejection attempts per microrafts were performed by the system. In total, 112 minutes were required from release, including software startup times (Table 3.1). The system measured and compensated for 2.5 ± 3.0 μm of displacement error in the stored microraft locations. 93.6% of the

microrafts were dislodged after 2 attempts. Image analysis of PDMS membranes punctured by the system indicate that there was little to no variation in microneedle puncture location across the microarray (13.9 ± 9.5 μm displacement with approximately 15 μm uncertainty in measurement method). Overall, the system was rapid, robust, and high throughput when releasing microrafts from quad microraft arrays.

3.3.7 Automated HiPSC biopsy

A large variety of bioassays depend on the ability to split a sample of cells into two or more sections; one for consumption by a cell-destructive assay or for quality control, and the other to retain for continued culture or for biobanking. As a proof-of-concept of the automated system, it was applied to split daughter cells from microarrays while leaving intact mother cells on the array. Every quad colony site was considered for release as long as it contained > 1 microraft with more than 50% cell coverage, a criterion which was selected to maximize biopsy survival and outgrowth rate. For quads with multiple possible biopsy targets, the system selected the microraft with the least cellular outgrowth, with the assumption that these microrafts would be the most readily released microrafts. For hiPSC colony biopsy, it was found that applying force near the microraft edge at the middle of colonies was effective at breaking apart the colony. To accommodate this, the initial needle impact was automated such that it aimed 5 μm from the spot on the raft periphery with the most edge cells. Furthermore, the automation was set only to dislodge the microrafts outside of their microwells, which was detected by either >80% reduction in microraft material present, >33% change in microraft material detected outside of its well, or the centroid of the dislodged microraft being >70 μm away from its initial location.

An array seeded with hiPSCs was cultured for 5 days with daily imaging. After pre-processing the array with EDTA, the automated system was set to attempt to dislodge one microraft

bearing cells from every quad containing two or more microrafts with cells. A total of 231 microrafts were automatically identified as targets, with 140, 36, and 55 targets from colonies with cells spread over 2, 3, and 4 microrafts, respectively. Manual inspection confirmed 230 of these targets were accurately selected. The system effectively dislodged the target microrafts over a period of 77 minutes, with 97.5% or 225 targets dislodged from their microwell (Figure 3.11). On average, 4.2 ± 1.6 dislodgement attempts were made per sample. Despite releasing an additional 0.48 adjacent microrafts per target, 73.6% or 170 of microraft targets were effectively biopsied while also leaving behind microrafts containing more mother cells. For 12% or 28 of targets, the entire targeted microcolony and adhered microrafts were removed. For the remaining 14.3% or 33 targets, one microraft was removed from the array but peeled the colony off from the remaining microrafts in the quad, leaving no cells behind on the microarray. Although a proportion of microrafts were completed ejected from the array, gentle rinsing with media was necessary to completely dislodge the microrafts that were still attached to the array by strands of ECM or cellular adhesions. The dislodged biopsies were transferred to Matrigel-coated cultureware by serological pipette. Although washing was nearly 100% effective at dislodging the microrafts, a substantial loss (estimated at 40% of all released microrafts) was observed after using a pipette to transfer the biopsies. Regardless, the transferred microrafts were highly viable and rapidly spread off of their microraft carriers. After 5 days of culture, the colonies consisted of dense, rapidly dividing cells. In total there was a yield of 110 colonies and 48 empty microrafts.

3.4 Conclusion

Microraft arrays are versatile tools for cytometry and cellular isolation. This work demonstrates the capabilities of microraft arrays for monitoring, maintaining, and isolating colonies of adherent cells, like hiPSCs. Specialized quad microraft arrays were designed to support

the culture of viable and pluripotent hiPSCs, as well as the spatial organization of cultured microcolonies for up to one week. Additionally, the array design enables colonies of cells spanning multiple microraft subunits to be biopsied using the indirect force of a microneedle applied at the bottom of one of the microrafts. This approach to hiPSC colony biopsy generated viable, pluripotent colony fragments and resulted in less cell damage than well-established cutting approaches using hand-manipulated cutting instruments.

The automated image analysis scheme developed for detecting hiPSC colonies was capable of locating microrafts and hiPSCs atop the 3D surface of the microrafts with high sensitivity and specificity. The automatic tracking of microrafts on the array over time allowed for the simple extraction of temporal metrics from thousands of microrafts per device. The hiPSC sensing method, which consisted of a background subtraction, standard deviation projection, and texture detection, is applicable to the robust brightfield detection of essentially any cell or colony type from images with arbitrary spatiotemporal backgrounds.

To demonstrate the utility of hiPSC sensing and biopsy, an automated system was developed to perform microraft imaging, analysis, and release processes. The use of visual feedback in the form of transmitted light images throughout the microraft release process was critical to maximize the speed and robustness of the automated system. As a proof-of-concept, the quad microraft array-based automated system was used to successfully identify and biopsy >200 mature hiPSC microcolonies for subsequent culture. Future research will focus on addressing the limitations of the technology by reducing the number of off-target microraft releases during splitting and eliminating manual liquid handling of the split colony fractions.

The ability to automate colony biopsy enables a wide range of automated bioassays. For example, automated microraft biopsy has the potential to act as an efficient front-end to cell-

destructive assays such as PCR, RNA-seq, and intracellular immunohistochemical staining of the released or biopsied cells while still maintaining the living mother colony for other applications. In the context of hiPSCs, automated biopsy could be applied for biological quality control, pruning of differentiated colonies, and passaging. Of particularly high impact would be to apply the system for automated genetic sorting using colony biopsies by screening the released colonies for particular gene sequence. Automated genetic sorting of hiPSCs would be indispensable for purifying cells at various stages of clinical and research pipelines, including: somatic cell reprogramming, induction or repair of disease-causing mutations, and evaluation of differentiation potential. Future work will focus on ways to encode the identity of biopsies, such that genetic data acquired from biopsies can be related back to the mother colonies from which the biopsies were taken.

3.5 Figures

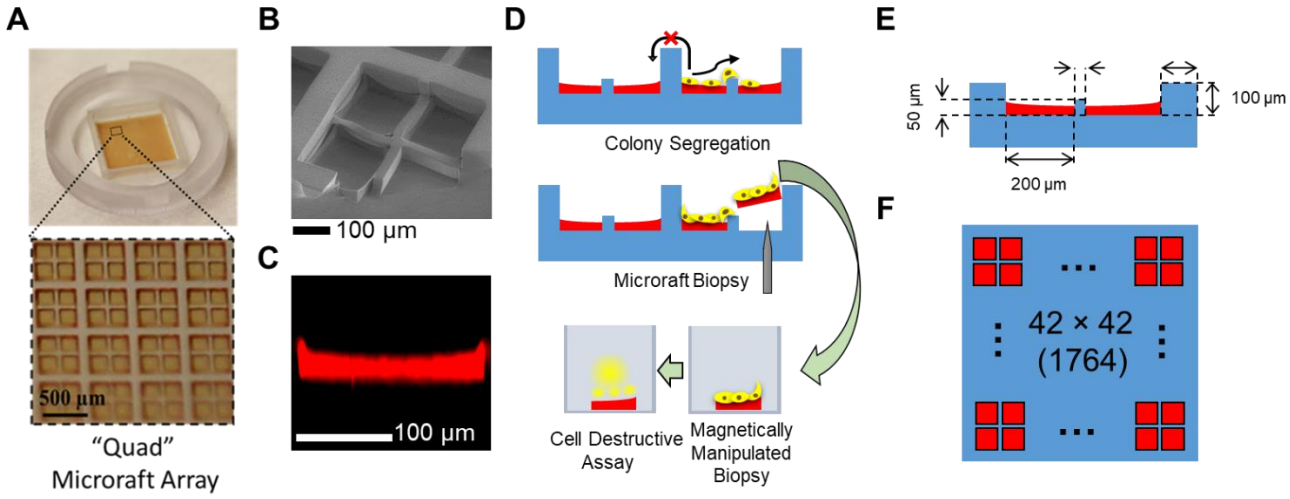

Figure 3.1 Quad microraft array design. (A) Photograph of a quad microraft array. (B) ESEM of one quad culture site on a microraft array. One microraft subunit and a portion of the lower PDMS barriers have been removed. (C) Confocal cross-section of one microraft subunit of a quad colony site. (D) Schematic of the intended quad microarray function. Top: proliferating cells spread over the surface of quad culture sites, physically impeded from expanded outside of their culture site by tall PDMS barriers; Middle: microcolonies are biopsied by ejecting underlying microrafts from the microarray; Bottom: Biopsies and their microraft carriers are magnetically manipulated for downstream applications. (E) Dimensions of quad microraft culture sites. (F) Footprint of quad microraft arrays, consisting of a uniform rectilinear grid of 42 × 42 quads.

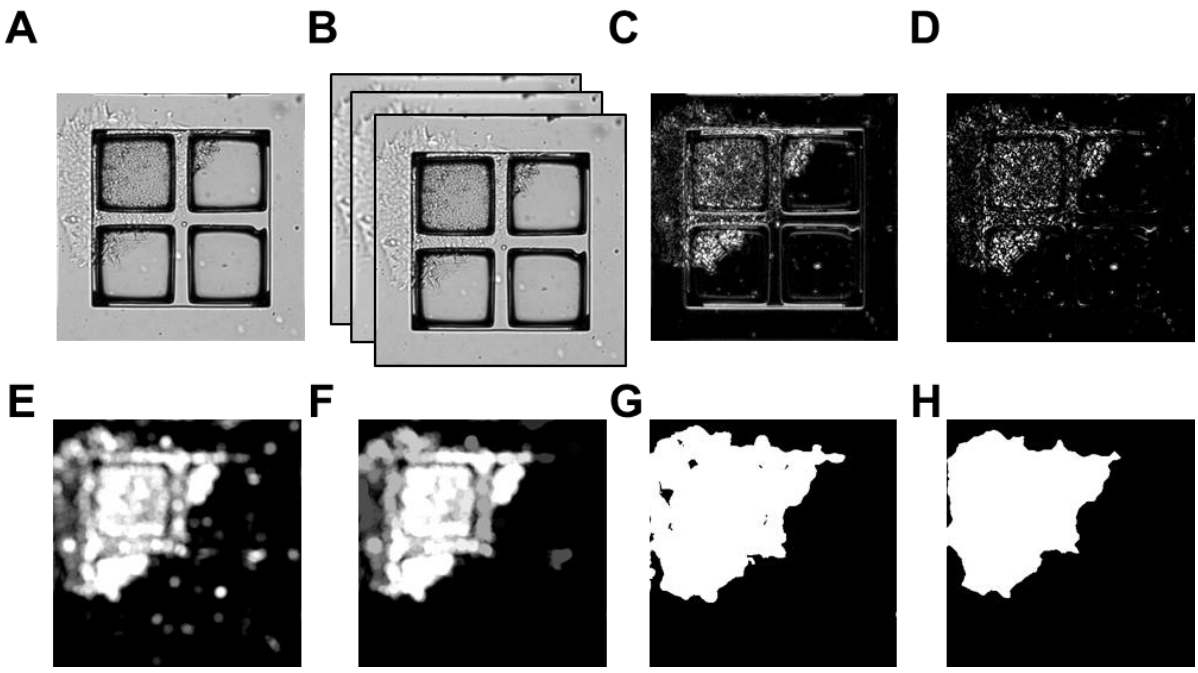

Figure 3.2 Automated brightfield detection of hiPSCs. (A) Illumination-, flat-field-, and registration- corrected brightfield images of a quad culture site with an adhered iPSC microcolony. (B) Corrected brightfield images were acquired at three focal planes. (C) Standard deviation intensity projection. (D) SDP image processed by a top-hat background subtraction. (E) Local entropy texture filtering of the background-subtracted SDP. (F) Result of a size-exclusion by reconstruction. (G) Intensity thresholded binary mask. (H) Colony segmentation after morphological processing of the binary mask.

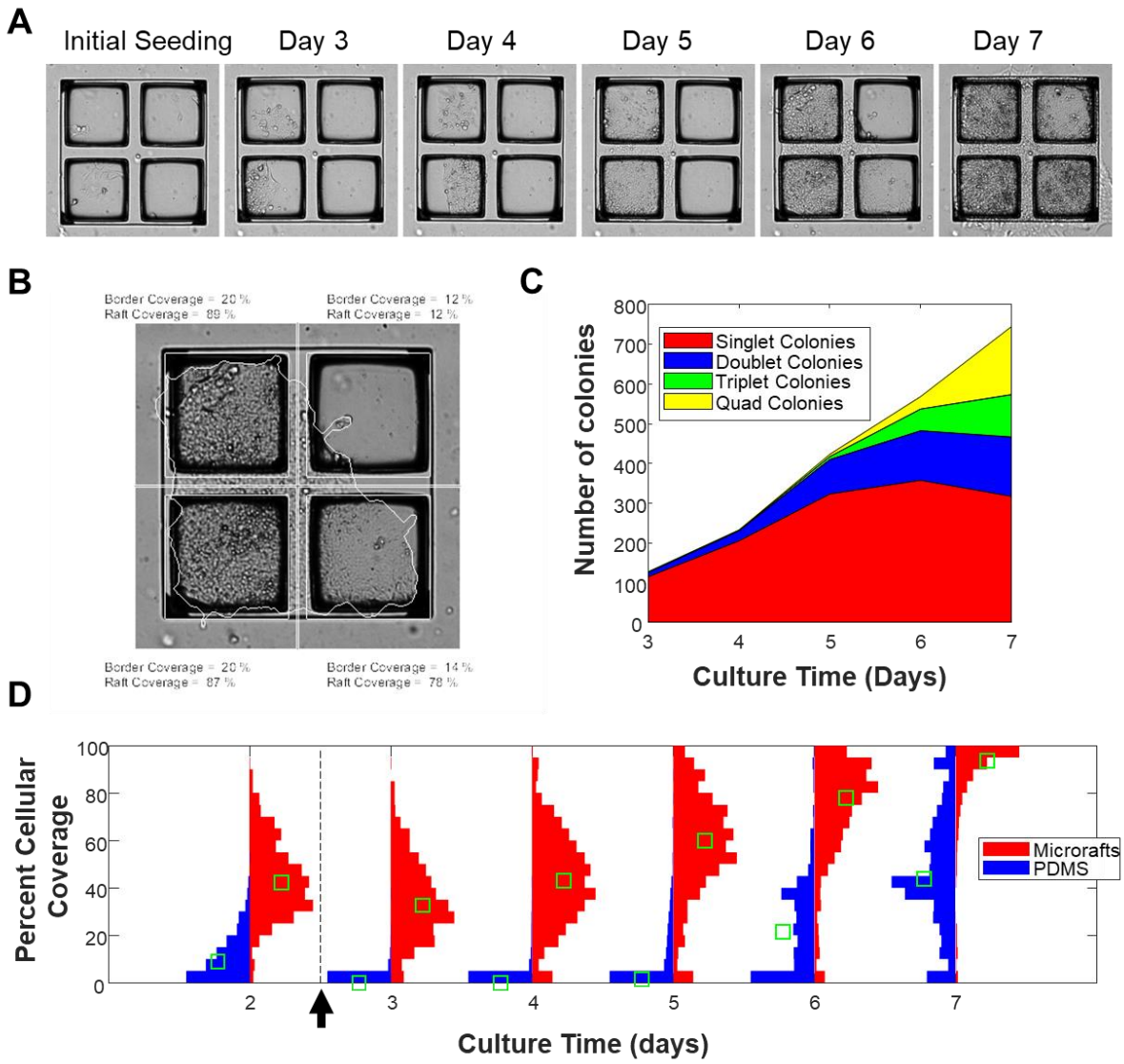

Figure 3.3 Cytometry of hiPSCs microcolonies on microraft arrays. (A) Timelapse brightfield microscopy of a representative hiPSC microcolony in culture on a quad microraft array. Microraft scale: 200 µm. (B) Detail of a brightfield image and overlaid segmentations (white) of microrafts, PDMS surfaces, and the hiPSC microcolony. Microraft scale: 200 µm. (C) Classification of microcolonies over time. Microcolonies spread over 1, 2, 3, or 4 microraft subunits of their associate quad culture site ("singlet", "doublet", "triplet", or "quad" colonies, respectively). (D)

Progression of microcolony size over microraft and PDMS surfaces of the microarray. Arrow and dashed line: Removal of Rock inhibitor from the culture medium.

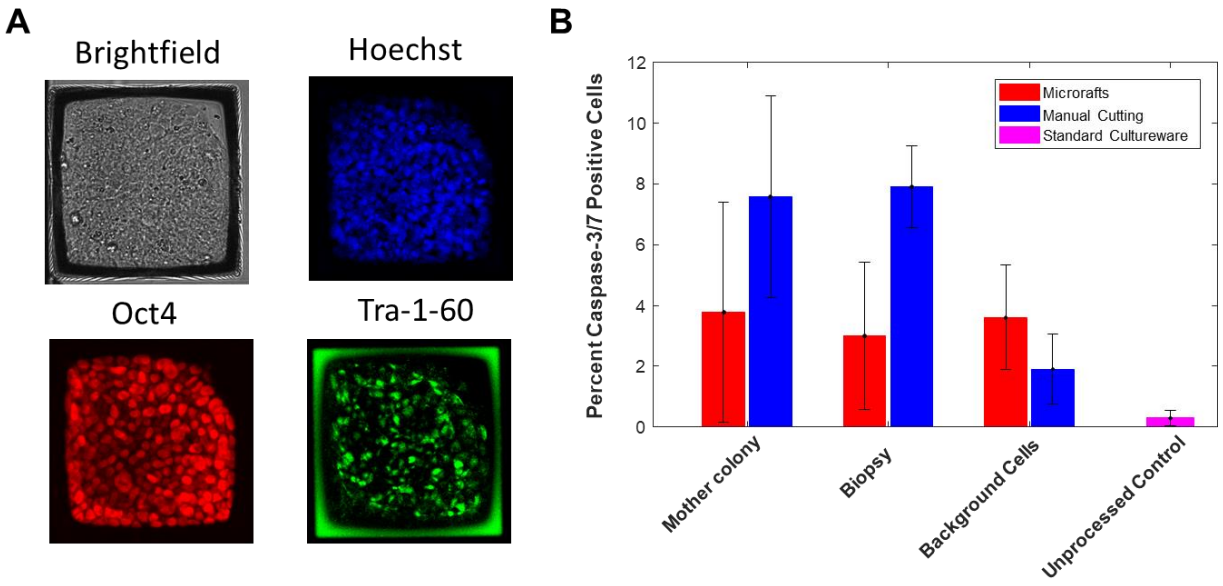

Figure 3.4 Pluripotency and viability of hiPSCs culture on quad microraft arrays. (A) Confocal average intensity projections of Oct4 and Tra-1-60 pluripotency markers compared to brightfield and Hoechst nuclear counterstain. (B) Quantitative comparison of cell apoptosis on mother colonies, biopsies, and unprocessed cells acquired using either microraft biopsy or manual mechanical cutting of hiPSCs.

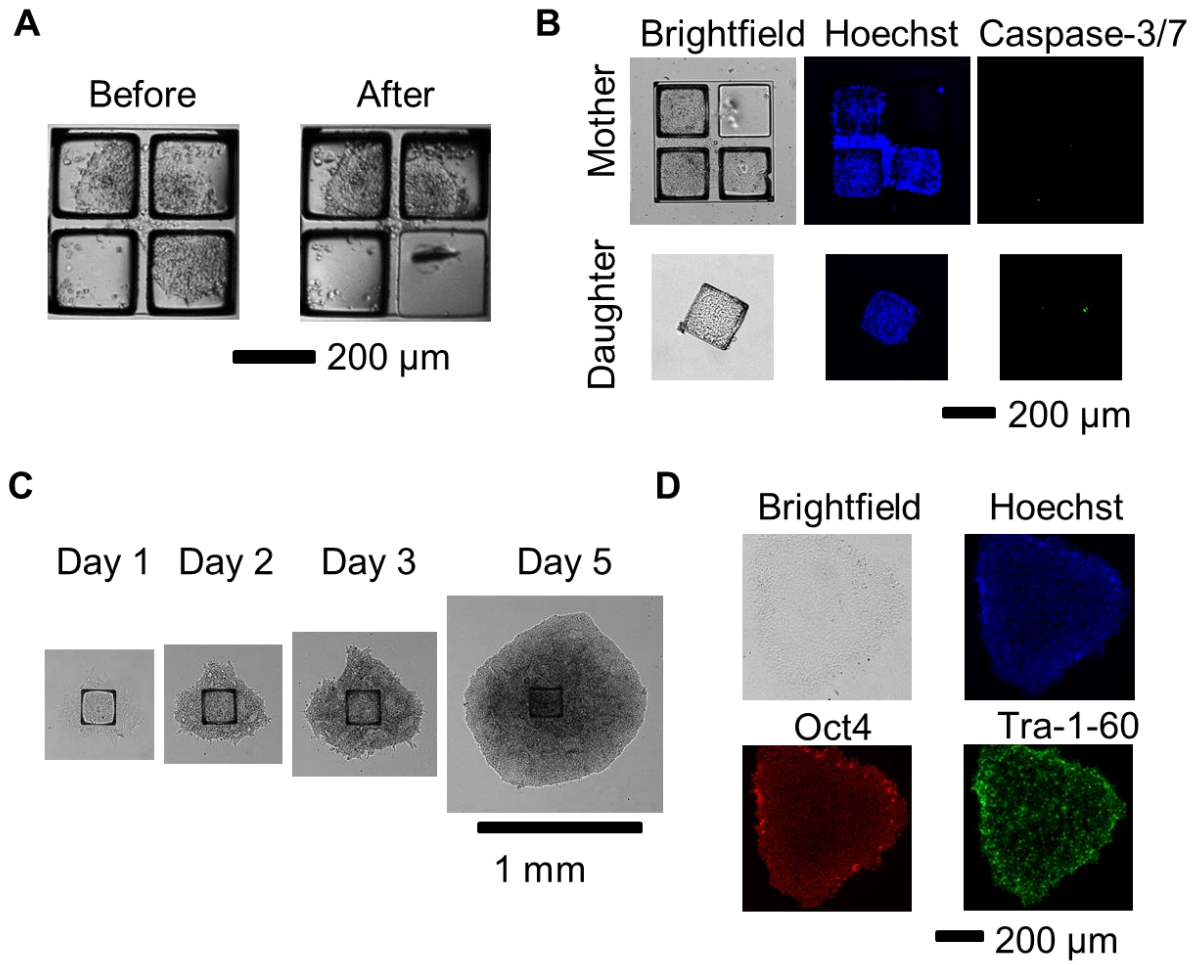

Figure 3.5 HiPSC biopsy using quad microraft arrays. (A) Brightfield microscopy of a microcolony before and after microneedle ejection of the lower right microraft subunit. (B) Caspase-3/7 viability assay of hiPSCs split by microrafts. (C) Timelapse images of a representative colony biopsy. (D) Immunohistochemistry for markers of pluripotency.

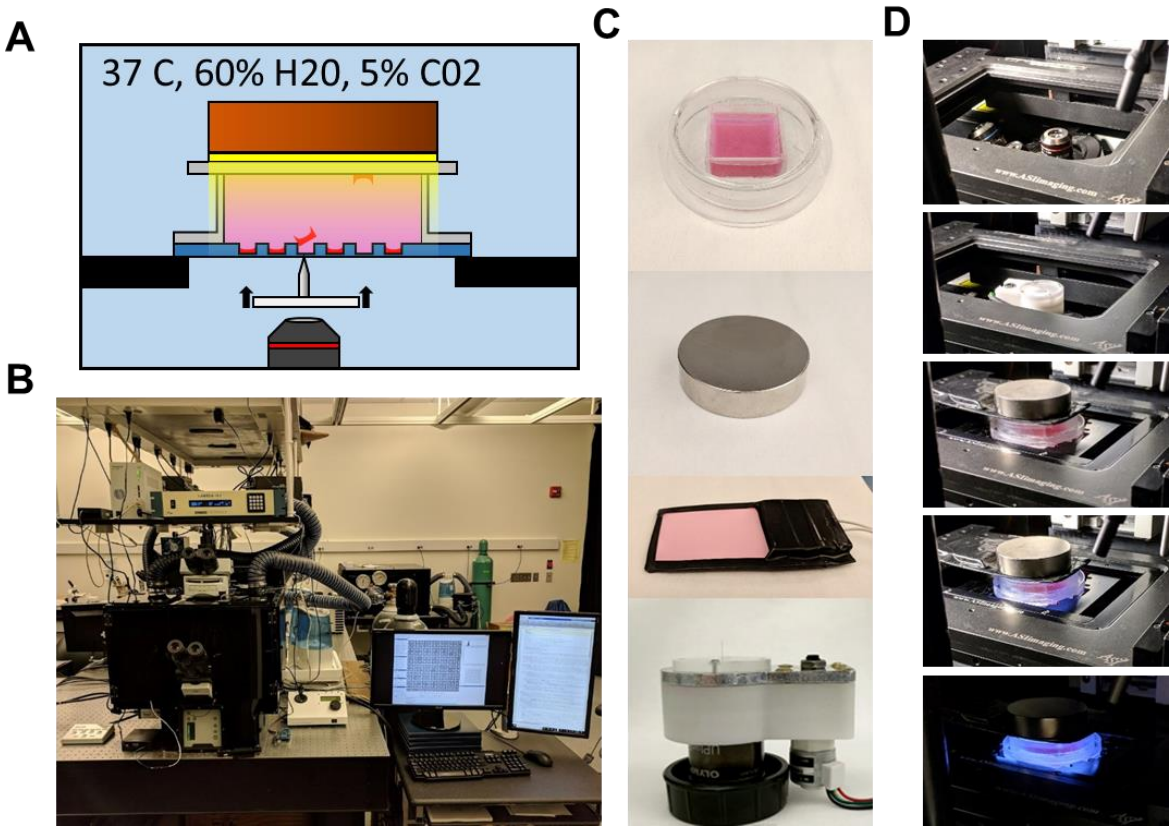

Figure 3.6 Automated microraft release system. (A) Schematic of automated microraft release approach. Superparamagnetic microrafts (red) are positioned over a microneedle using a motorized X-Y stage, after which the microneedle is actuated to dislodge the microrafts from the PDMS microarray substrate (blue). Dislodged microrafts are pulled upwards through liquid media (pink) by a magnet (brown) placed above the microdevice. An electroluminescence panel (yellow) illuminates the microarray, enabling an inverted microscope to collect visual feedback about the location of microrafts throughout the process. (B) Motorized IX81 microscope, incubator, and PC setup. (C) From top to bottom: quad microraft array, neodymium disk magnet, electroluminescent light panel, and motorized microneedle device. (D) Assembly of hardware on the motorized microscope, in sequence from top to bottom.

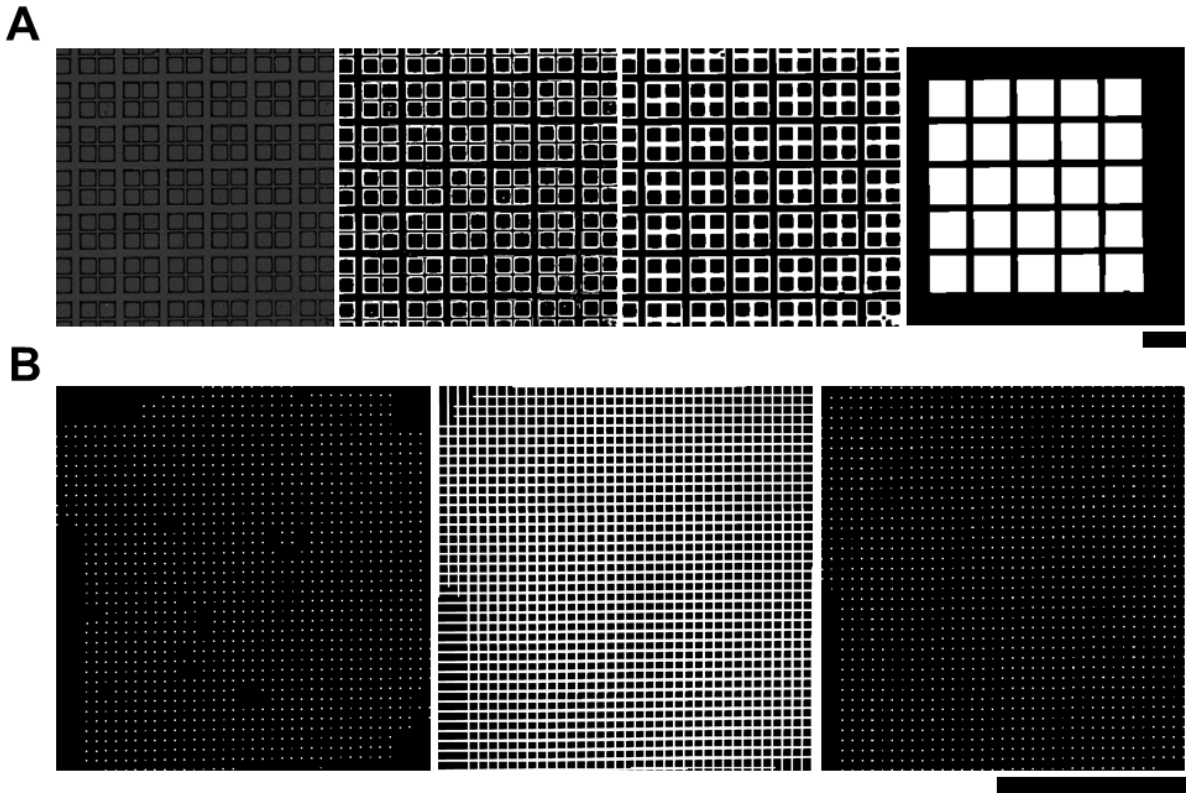

Figure 3.7 Automated detection and identification of quad microrafts. (A) From left to right: Brightfield image of quad microrafts, intensity-thresholded binary mask, morphologically closed mask, and morphologically processed segmentation of microraft quads. Scale: 500 μm. (B) From left to right: Binary representation of the located microrafts in a quad microraft array with each quad represented by a white dot, morphological dilation using 0- and 90- degree linear structuring elements, and final adjusted microraft locations with interpolated microrafts. Scale: 10 mm.

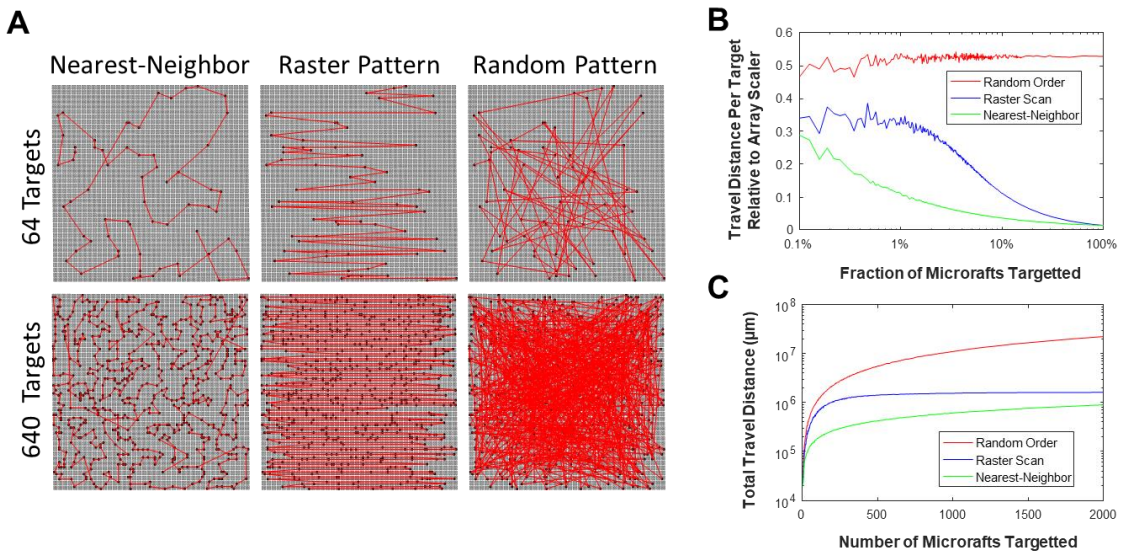

Figure 3.8. Pathing optimization between microraft targets. (A) Illustrative comparison between nearest neighbor, raster, and random pathing algorithms. Gray: microrafts; Black: targets; Red: transit path. (B) Distance traversed per target as a function of the fraction of microrafts targeted. (B) Total travel distance as a function of the number of microrafts targeted.

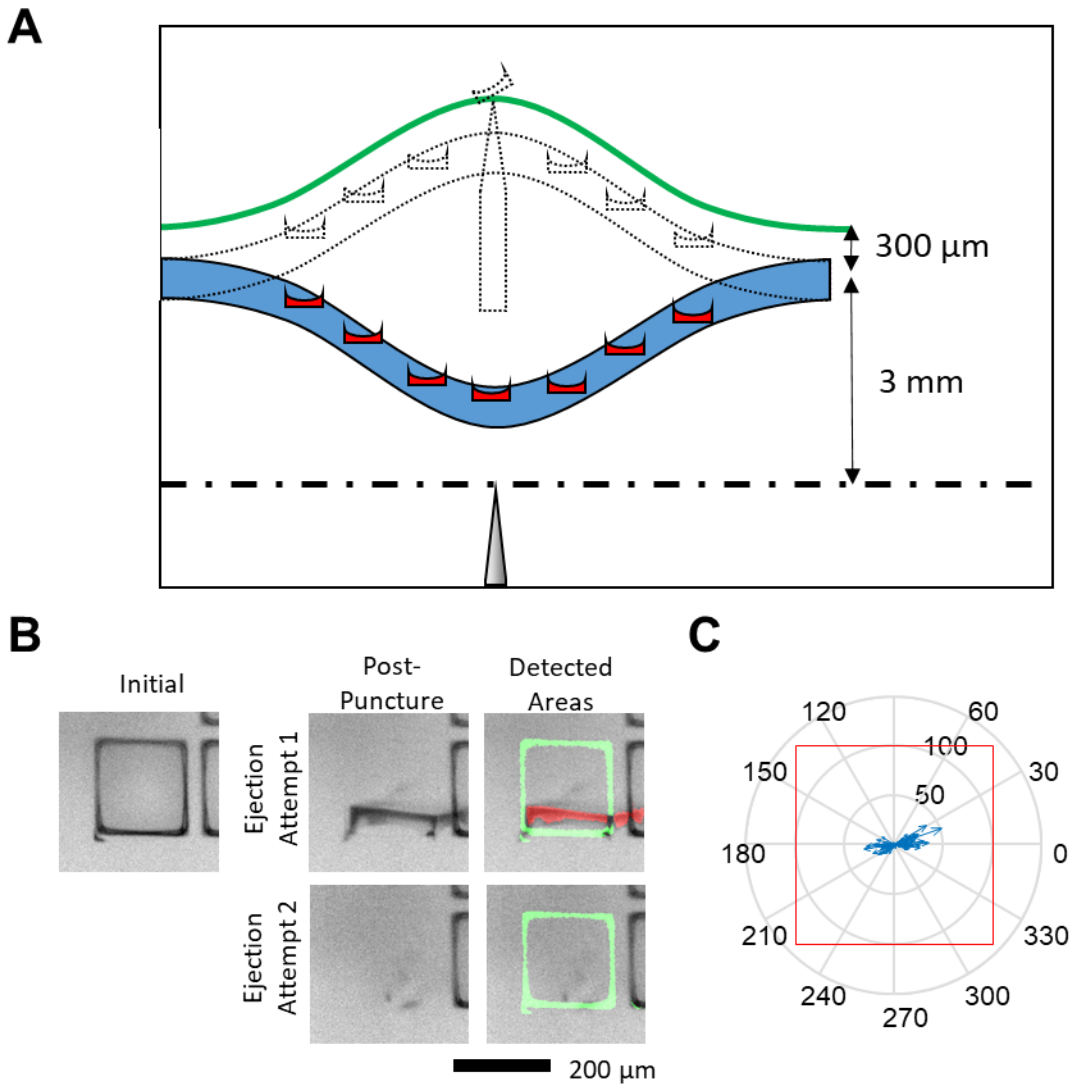

Figure 3.9. Automated microneedle release of quad microrafts. (A) Schematic of microneedle actuation strategy, as seen in a cross-section through the device. During stage translation, the microneedle is held 3 mm from the microarray (dash-dotted line). During microneedle actuation (dotted outline), to compensate for the increased vertical play in the membrane, the microneedle is translated further (green curve) to dislodge microrafts at the center of the microarray than those at the edge. (B) EL-illuminated brightfield images of a microraft target during the automated release process. Green: detection of dislodged microraft material; Red: detection of undislodged

microraft material. (C) Compass plot distribution of microneedle puncture errors. Distance in microns. For scale, the size of a microraft is shown in red.

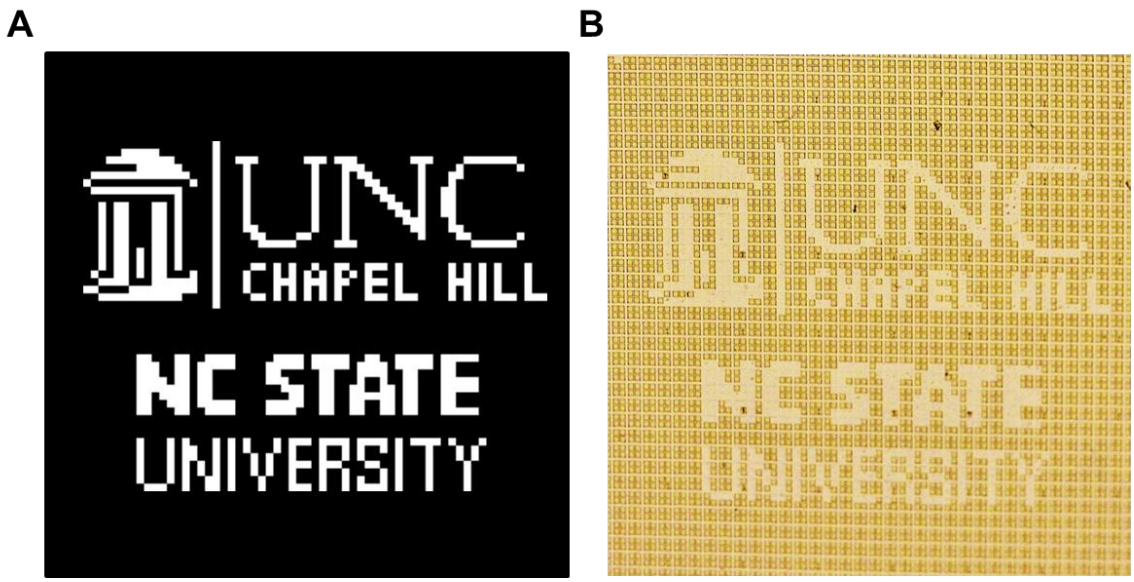

Figure 3.10 High-throughput automated release of quad microrafts. (A) Binary mask of university logos. (B) Photograph of the processed microarray.

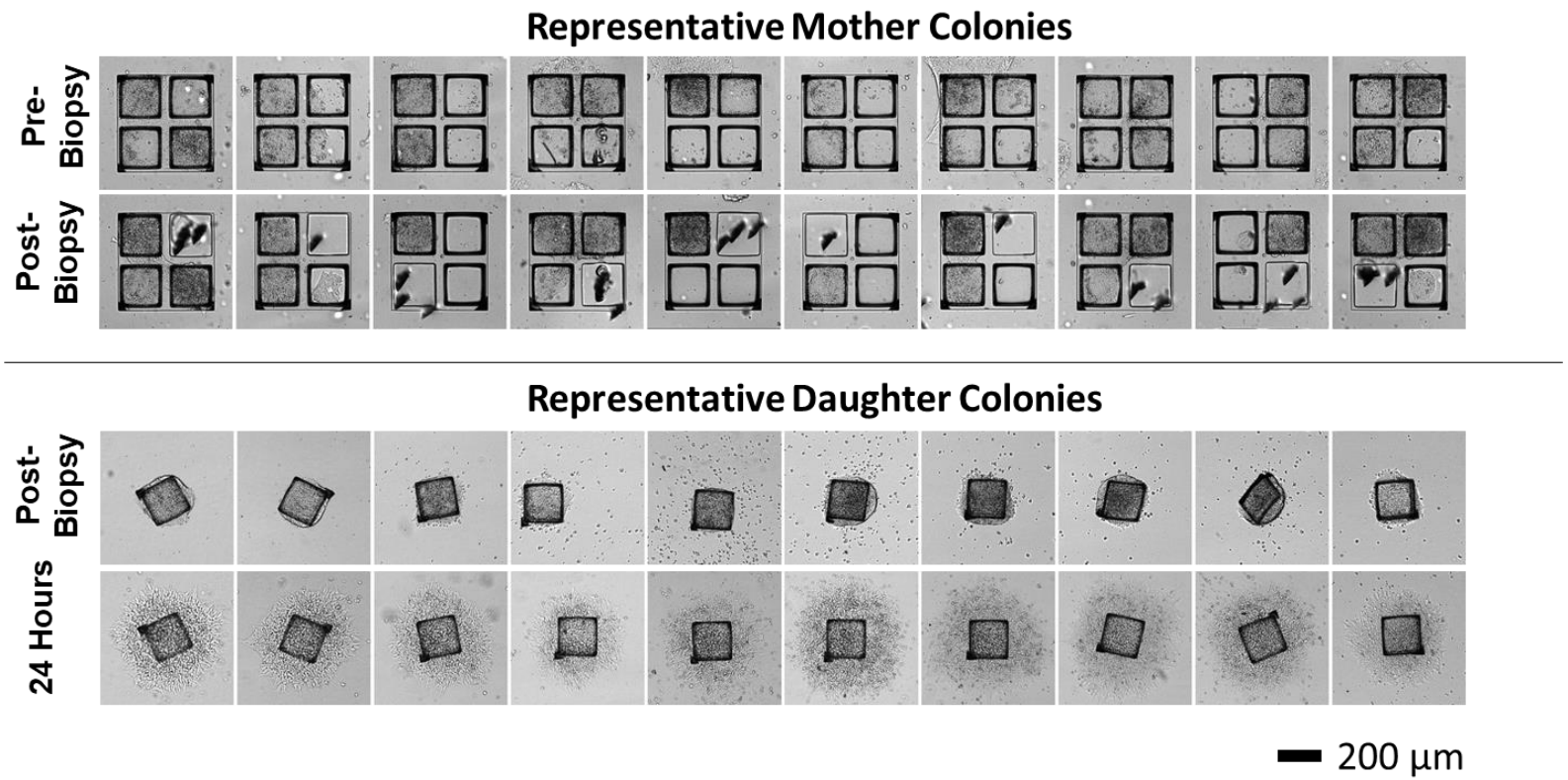

Figure 3.11 Automated hiPSC biopsy using quad microraft arrays. Brightfield microscopy images of representative mother and daughter colonies after microcolony splitting.

3.6 Tables

Table 3.1 Temporal breakdown of automated microraft release

	Total Time (min)	Iterations	Time per iteration (s)
Microarray shape modeling	2.6	1	154.5
Locating microrafts	1.7	1	103.8
Identifying microrafts	1.0	1	59.4
Autofocusing	6.9	28	14.8 ± 0.4
Needle positioning	5.3	683	0.5 ± 0.2
Needle actuation	37.4	1185	1.9 ± 0.04
Image guidance	56.6	1185	2.9
Total	111.5		

3.7 REFERENCES

(1) Ghaedi, M.; Niklason, L. E. Human Pluripotent Stem Cells (iPSC) Generation, Culture, and Differentiation to Lung Progenitor Cells; Humana Press, 2016; pp 1–38.

(2) van der Sanden, B.; Dhobb, M.; Berger, F.; Wion, D. Optimizing Stem Cell Culture. *J. Cell. Biochem.* **2010**, *111* (4), 801–807.

(3) Lawrenz, B.; Schiller, H.; Willbold, E.; Ruediger, M.; Muhs, A.; Esser, S. Highly Sensitive Biosafety Model for Stem-Cell-Derived Grafts. *Cytotherapy* **2004**, *6* (3), 212–222.

(4) Masuda, S.; Miyagawa, S.; Fukushima, S.; Sougawa, N.; Ito, E.; Takeda, M.; Saito, A.; Sawa, Y. Emerging Innovation towards Safety in the Clinical Application of ESCs and iPSCs. *Nat. Rev. Cardiol.* **2014**, *11* (9), 553–554.

(5) Silva, M.; Daheron, L.; Hurley, H.; Bure, K.; Barker, R.; Carr, A. J.; Williams, D.; Kim, H. W.; French, A.; Coffey, P. J.; et al. Generating iPSCs: Translating Cell Reprogramming Science into Scalable and Robust Biomanufacturing Strategies. *Cell Stem Cell* **2015**, *16* (1), 13–17.

(6) Van Der Sanden, B.; Dhobb, M.; Berger, F.; Wion, D. Optimizing Stem Cell Culture. *J. Cell. Biochem.* **2010**, *111* (4), 801–807.

(7) Beers, J.; Gulbranson, D. R.; George, N.; Siniscalchi, L. I.; Jones, J.; Thomson, J. A.; Chen, G. Passaging and Colony Expansion of Human Pluripotent Stem Cells by Enzyme-Free Dissociation in Chemically Defined Culture Conditions. *Nat Protoc* **2012**, *7*, 2029–2040.

(8) Amit, M.; Carpenter, M. K.; Inokuma, M. S.; Chiu, C.-P.; Harris, C. P.; Waknitz, M. A.; Itskovitz-Eldor, J.; Thomson, J. A. Clonally Derived Human Embryonic Stem Cell Lines Maintain Pluripotency and Proliferative Potential for Prolonged Periods of Culture. *Dev. Biol.* **2000**, *227* (2), 271–278.

(9) Brimble, S. N.; Zeng, X.; Weiler, D. A.; Luo, Y.; Liu, Y.; Lyons, I. G.; Freed, W. J.; Robins, A. J.; Rao, M. S.; Schulz, T. C. Karyotypic Stability, Genotyping, Differentiation, Feeder-Free Maintenance, and Gene Expression Sampling in Three Human Embryonic Stem Cell Lines Derived Prior to August 9, 2001. *Stem Cells Dev.* **2004**, *13* (6), 585–597.

(10) Draper, J. S.; Smith, K.; Gokhale, P.; Moore, H. D.; Maltby, E.; Johnson, J.; Meisner, L.; Zwaka, T. P.; Thomson, J. A.; Andrews, P. W. Recurrent Gain of Chromosomes 17q and 12 in Cultured Human Embryonic Stem Cells. *Nat. Biotechnol.* **2004**, *22* (1), 53–54.

(11) Kamei, K.; Ohashi, M.; Gschweng, E.; Ho, Q.; Suh, J.; Tang, J.; For Yu, Z. T.; Clark, A. T.; Pyle, A. D.; Teitell, M. A.; et al. Microfluidic Image Cytometry for Quantitative Single-Cell Profiling of Human Pluripotent Stem Cells in Chemically Defined Conditions. *Lab Chip* **2010**, *10* (9), 1113.

(12) Nketia, T. A.; Sailem, H.; Rohde, G.; Machiraju, R.; Rittscher, J. Analysis of Live Cell Images: Methods, Tools and Opportunities. *Methods* **2017**, *115*, 65–79.

(13) Tokunaga, K.; Saitoh, N.; Goldberg, I. G.; Sakamoto, C.; Yasuda, Y.; Yoshida, Y.; Yamanaka, S.; Nakao, M. Computational Image Analysis of Colony and Nuclear Morphology to Evaluate Human Induced Pluripotent Stem Cells. *Sci. Rep.* **2014**, *4*, 6996.

(14) Maddah, M.; Shoukat-Mumtaz, U.; Nassirpour, S.; Loewke, K. A System for Automated, Noninvasive, Morphology-Based Evaluation of Induced Pluripotent Stem Cell Cultures. *J. Lab. Autom.* **2014**, *19* (5), 454–460.

(15) Joannides, A.; Fiore-Hériché, C.; Westmore, K.; Caldwell, M.; Compston, A.; Allen, N.; Chandran, S. Automated Mechanical Passaging: A Novel and Efficient Method for Human Embryonic Stem Cell Expansion. *Stem Cells* **2006**, *24* (2), 230–235.

(16) Paull, D.; Sevilla, A.; Zhou, H.; Hahn, A. K.; Kim, H.; Napolitano, C.; Tsankov, A.; Shang, L.; Krumholz, K.; Jagadeesan, P.; et al. Automated, High-Throughput Derivation, Characterization and Differentiation of Induced Pluripotent Stem Cells. *Nat. Methods* **2015**, *12* (9), 885–892.

(17) Crombie, D. E.; Daniszewski, M.; Liang, H. H.; Kulkarni, T.; Li, F.; Lidgerwood, G. E.; Conquest, A.; Hernández, D.; Hung, S. S.; Gill, K. P.; et al. Development of a Modular Automated System for Maintenance and Differentiation of Adherent Human Pluripotent Stem Cells. *SLAS Discov. Adv. Life Sci. R&D* **2017**, *22* (8), 1016–1025.

(18) Terstegge, S.; Rath, B. H.; Laufenberg, I.; Limbach, N.; Buchstaller, A.; Schütze, K.; Brüstle, O. Laser-Assisted Selection and Passaging of Human Pluripotent Stem Cell Colonies. *J. Biotechnol.* **2009**, *143* (3), 224–230.

(19) Haupt, S.; Grutzner, J.; Thier, M. C.; Kallweit, T.; Rath, B. H.; Laufenberg, I.; Forgber, M.; Eberhardt, J.; Edenhofer, F.; Brustle, O. Automated Selection and Harvesting of Pluripotent Stem Cell Colonies. *Biotechnol Appl Biochem* **2012**, *59* (2), 77–87.

(20) Daniszewski, M.; Crombie, D. E.; Henderson, R.; Liang, H. H.; Wong, R. C. B.; Hewitt, A. W.; Pébay, A. Automated Cell Culture Systems and Their Applications to Human Pluripotent Stem Cell Studies. *SLAS Technol. Transl. Life Sci. Innov.* **2017**, 247263031771222.

(21) Toh, Y.-C.; Blagović, K.; Voldman, J. Advancing Stem Cell Research with Microtechnologies: Opportunities and Challenges. *Integr. Biol. (Camb).* **2010**, *2* (7–8), 305–325.

(22) Luni, C.; Gagliano, O.; Elvassore, N. Microfluidic Technology Enhances the Potential of Human Pluripotent Stem Cells. *Biochem. Biophys. Res. Commun.* **2016**, *473* (3), 10–14.

(23) Giobbe, G. G.; Michielin, F.; Luni, C.; Giulitti, S.; Martewicz, S.; Dupont, S.; Floreani, A.; Elvassore, N. Functional Differentiation of Human Pluripotent Stem Cells on a Chip. *Nat. Methods* **2015**, *12* (7), 637–640.

(24) Kim, L.; Vahey, M. D.; Lee, H.-Y.; Voldman, J. Microfluidic Arrays for Logarithmically Perfused Embryonic Stem Cell Culture. *Lab Chip* **2006**, *6* (3), 394–406.

(25) Moeller, H. C.; Mian, M. K.; Shrivastava, S.; Chung, B. G.; Khademhosseini, A. A Microwell Array System for Stem Cell Culture. *Biomaterials* **2008**, *29* (6), 752–763.

(26) Carlson-Stevermer, J.; Goedland, M.; Steyer, B.; Movaghar, A.; Lou, M.; Kohlenberg, L.; Prestil, R.; Saha, K. High-Content Analysis of CRISPR-Cas9 Gene-Edited Human Embryonic Stem Cells. *Stem Cell Reports* **2016**, *6* (1), 109–120.

(27) Shadpour, H.; Sims, C. E.; Thresher, R. J.; Allbritton, N. L. Sorting and Expansion of Murine Embryonic Stem Cell Colonies Using Micropallet Arrays. *Cytom. A* **2009**, *75* (2), 121–129.

(28) Gach, P. C.; Xu, W.; King, S. J.; Sims, C. E.; Bear, J.; Allbritton, N. L. Microfabricated Arrays for Splitting and Assay of Clonal Colonies. *Anal Chem* **2012**, *84* (24), 10614–10620.

(29) Pai, J. H.; Kluckman, K.; Cowley, D. O.; Bortner, D. M.; Sims, C. E.; Allbritton, N. L. Efficient Division and Sampling of Cell Colonies Using Microcup Arrays. *Analyst* **2013**, *138*, 220–228.

(30) Gach, P. C.; Wang, Y.; Phillips, C.; Sims, C. E.; Allbritton, N. L. Isolation and Manipulation of Living Adherent Cells by Micromolded Magnetic Rafts. *Biomicrofluidics* **2011**, *5* (3), 32002–3200212.

(31) Attayek, P. J.; Hunsucker, S. A.; Sims, C. E.; Allbritton, N. L.; Armistead, P. M. Identification and Isolation of Antigen-Specific Cytotoxic T Lymphocytes with an Automated Microraft Sorting System. *Integr. Biol. (Camb).* **2016**, *8* (12), 1208–1220.

(32) Attayek, P. J.; Hunsucker, S. A.; Wang, Y.; Sims, C. E.; Armistead, P. M.; Allbritton, N. L. Array-Based Platform to Select, Release, and Capture Epstein-Barr Virus-Infected Cells Based on Intercellular Adhesion. *Anal. Chem.* **2015**, *87* (24).

(33) DiSalvo, M.; Wang, Y.; Attayek, P. J.; Sims, C. E.; Allbritton, N. L. Development of Quad Raft Arrays for Directed Growth of Clonal Colonies. *18th Int. Conf. Miniaturized Syst. Chem. Life Sci. MicroTAS 2014* **2014**, 415–417.

(34) Chowdhury, A. S.; Paul, A.; Bunyak, F.; Cornelison, D. D. W.; Palaniappan, K. Semi-Automated Tracking of Muscle Satellite Cells in Brightfield Microscopy Video. *Proc. - Int. Conf. Image Process. ICIP* **2012**, 2825–2828.

(35) Selinummi, J.; Ruusuvuori, P.; Podolsky, I.; Ozinsky, A.; Gold, E.; Yli-Harja, O.; Aderem, A.; Shmulevich, I. Bright Field Microscopy as an Alternative to Whole Cell Fluorescence in Automated Analysis of Macrophage Images. *PLoS One* **2009**, *4* (10), e7497.

(36) Guizar-Sicairos, M.; Thurman, S. T.; Fienup, J. R. Efficient Subpixel Image Registration Algorithms. *Opt. Lett.* **2008**, *33* (2), 156.

(37) Thelen, A.; Frey, S.; Hirsch, S.; Hering, P. Improvements in Shape-From-Focus for Holographic Reconstructions With Regard to Focus Operators, Neighborhood-Size, and Height Value Interpolation. *IEEE Trans. Image Process.* **2009**, *18* (1), 151–157.

(38) DiSalvo, M.; Harris, D. M.; Kantesaria, S.; Peña, A. N.; Allbritton-King, J. D.; Cole, J. H.; Allbritton, N. L. Characterization of Tensioned PDMS Membranes for Imaging Cytometry on Microraft Arrays. *Anal. Chem.* **2018**, acs.analchem.8b00176.

(39) Otsu, N. A Threshold Selection Method from Gray-Level Histograms. *IEEE Trans. Syst. Man. Cybern.* **1979**, *9* (1), 62–66.

CHAPTER 4: AUTOMATED IMAGING OF ARRAYED COLONIC ORGANOIDS FOR SCREENING OF SECRETAGOGUES ASSOCIATED WITH ENTEROTOXINS[1]

4.1 Introduction

Infectious diarrheas caused by bacterial production of enterotoxins are common diseases worldwide. Enterotoxins, such as cholera toxin produced by the bacteria *Vibrio cholerae*, interact with intestinal epithelial cells to increase the movement of water and ions into the intestinal lumen, the consequence of which is severe diarrhea.[1] Cholera toxin acts through a series of steps that include binding of the toxin to the surface of epithelial cells, endocytosis and a series of enzymatic reactions that result in the release of the cholera toxin A1 (CTA1) chain which binds to the intracellular protein ADP-ribosylation factor 6 (Arf6) resulting in CTA1 activation.[2] Through an additional series of enzymatic steps, CTA1 increases the activity of the Gs alpha subunit (Gαs) proteins leading to increased adenylyl cyclase activity that results in an elevation in 3',5'-cyclic AMP (cAMP) concentration more than 100-fold higher than normal leading to increased activity of protein kinase A (PKA). Phosphorylation of the cystic fibrosis transmembrane conductance regulator (CFTR) chloride channel proteins by PKA then leads to ATP-mediated efflux of chloride ions resulting in the movement of H_2O as well as sodium, potassium and bicarbonate ions into the intestinal lumen.[1,3,4] The calcium activated chloride channel (CLCA) can also cause fluid migration in response to toxin-mediated increase in the concentration of intracellular Ca^{2+}.[5] Other enterotoxins also secreted by the *Vibrio* bacteria are known to activate the enteric nervous and

[1] Reprinted with permission from *Anal. Chem.*, 2018, 90 (3), pp 1941–1950, DOI:10.1021/acs.analchem.7b04032. Copyright 2017 American Chemical Society.

immune systems producing agonists such as prostaglandins, acetylcholine and histamine which can also participate in intestinal ion and water movement through intracellular cAMP or Ca^{2+} signaling.[1] The synergistic impact of enterotoxin-mediated effects combine to increase intestinal secretion yielding rapid and cumulative fluid loss of up to 2 liters per hour into the intestine causing severe dehydration that may result in death.[6]

To study intestinal ion secretion and fluid movement, tissue-cultured tumor cell lines are often used as surrogate intestinal cells. However, the genetic profile and functional properties of tumor cells do not match that of primary tissue.[7] Intestinal organoids derived from primary cells offer a more accurate functional model of *in vivo* tissue physiology compared to that of tumor cells.[8,9] Proliferative organoids are readily cultured from crypts or stem cells isolated from the intestine and are maintained by culture within a thick layer of hydrogel (typically Matrigel) in the presence of a medium rich in growth factors.[10] The organoids possess all cell types of the intestine including stem/proliferative cells, enterocytes and goblet cells. These cells form a monolayer surrounding a central lumen and are polarized so that their luminal surface faces into the central cavity while the basal cell surface makes contacts with the extracellular matrix proteins within the surrounding hydrogel. This cell polarity enables the organoids to retain many physiologic functions such as the transport of ions across the monolayer.[8,11] Contact between the basal, cell-surface proteins and the extracellular matrix is thought to be required to provide the correct mechanical and chemical environment for proper organoid formation, monolayer polarity, and ion transport function.[12,13,8]

Intestinal organoids have been used for nutrient[14], P-glycoprotein (P-gp)[15], and ion transport assays.[11] When ions are secreted by the monolayer, water follows by a passive mechanism termed osmosis. When sufficient numbers of ions are secreted, the increase in luminal

volume due to water movement results in the swelling of these spheroidal structures and an increase in the organoid's cross-sectional area. This area increase can be measured directly[16,11] or indirectly[17] when imaged by microscopy. This phenomenon has enabled intestinal organoids to be used in the study of drug effects, genetic mutation impact, and toxin effect on ion secretion in the organoids.[18–20,11,16] However, embedding the organoids fully within a hydrogel poses a number of challenges to increasing the assay throughput.[21] The organoids cultured in a Petri dish or multiwell plate are typically positioned at random locations along the x, y, and z axes of the thick hydrogel layer leaving the organoids in varying image planes when viewed by microscopy. This creates two challenges that severely limit assay speed: organoids that are out of focus when using a single image plane and organoids that overlap in the x-y plane when viewed from above or below by standard microscopy. Strategies to mitigate these weaknesses would increase the numbers of organoids per well that are suitable for assay and increase experimental throughput. A second disadvantage is that compounds and drugs must diffuse through the hydrogel to access the organoid. Interactions of the molecules with the Matrigel can impose a time delay in compounds reaching the organoid or decrease the concentration of the compound at the organoid's location. Thus, the compound-Matrigel interactions represent an uncontrolled variable in organoid experiments.

Herein is described the development of a method to create a planar array of colonoids with the colonoids located on the surface of a hydrogel and compatible with automated image-based assays. The properties of the surface-positioned colonoids were compared to hydrogel-embedded organoids. Software to perform organoid segmentation and separation of nearby organoids as well as identification of the colonoid location was implemented. An automated analysis pipeline identified and quantified the properties of organoids over time and was compared to manual

identification and measurement. Colonoid swelling in response to forskolin, cholera toxin and physiologic molecules was assessed to characterize the extent and heterogeneity of swelling in a population of organoids as well as the rate of fluid movement across the organoid wall. This approach should enable efficient, large-scale screening of the impact of drugs, toxins and other compounds on colonoid physiology.

4.2 Contributions to this work

This work was performed in equal contribution with Dr. Dulan Gunasekara, who performed the *in vitro* culture of cells, cell staining, and compound preparations, which are described primarily in Sections 4.3.1 – 4.3.5.

4.3 Experimental Section

4.3.1 Materials

Polystyrene 96-well plates were purchased from Denville Scientific, Inc, Holliston, MA. Transwells, Matrigel, EDTA, HEPES and gentamicin were purchased from Corning, NY. DMSO was acquired from Santa Cruz Biotechnology, Dallas, TX. Optimum cutting temperature (O.C.T.) formulation was obtained from Tissue-Tek®, Sakura Finetek USA, Inc. Torrance, CA. Na_2HPO_4, KH_2PO_4, NaCl, KCl, advanced DMEM/F-12 medium, dithiothreitol (DTT), GlutaMAX, penicillin and streptomycin were from Thermo Fisher Scientific, Waltham, MA. Epidermal growth factor (EGF), N-acetyl cysteine, sucrose, D-sorbitol, cholera toxin and subunit B, bradykinin, prostaglandin E2, adenosine, serotonin, acetylcholine and histamine were purchased from Sigma, St. Louis, MO. Vasoactive intestinal peptide was purchased from AnaSpec, Fremont, CA. Fetal bovine serum (FBS) was obtained from Atlanta Biologicals, Flowery Branch, GA. Collagenase Type iv was purchased from Worthington Biochemical Corporation, Lakewood, NJ. Information for staining and assay kits are provided in the relevant sections of the Experimental Section.

4.3.2 Isolation of crypts from mouse colon and initial culture

The cytomegalovirus enhancer plus chicken actin promoter (CAG)-DsRed mouse model in which all cells expressed the DsRed fluorescent protein, and wild-type (WT) mice were used for experiments.[22,23] All experiments and animal usage were in compliance with the University of North Carolina animal care protocol and were approved by the Institutional Animal Care and Use Committee (IACUC). Mice heterozygous for DsRed expression were bred on a CD-1 background and WT mice were bred on a C57BL/6 background. Mice (male and female ages 6-10 months) were humanely euthanized by a lethal dose of isoflurane followed by cervical dislocation under the UNC IACUC-approved protocol #13-200. A detailed procedure for crypt isolation and culture was previously reported.[24,25] Briefly, a colon was surgically extracted from a mouse following euthanasia. The colon was then opened longitudinally and incubated with EDTA (2 mM) and DTT (0.5 mM) in isolation buffer (5.6 mM Na_2HPO_4, 8.0 mM KH_2PO_4, 96.2 mM NaCl, 1.6 mM KCl, 43.4 mM sucrose, 54.9 mM D-sorbitol at pH 7.4) for 75 min at room temperature prior to isolation of crypts. Then the tissue was vigorously shaken in a conical tube with isolation buffer to release the crypts from the underlying stroma. Released crypts were pelleted by centrifugation and mixed with Matrigel (2500 crypts in 100 μL of Matrigel) on ice (4 °C). 10 μL of this mix was plated in wells of a 24-well plate, and the plate was immediately inverted to prevent any contacts between tissue pieces and the polystyrene surface. The Matrigel was then cured at 37 °C in a cell culture incubator for 15 min. These cultures were subcultured up to 5 times.

Both embedded and arrayed cultures were grown in medium rich in growth factors termed stem cell medium (SM). SM was prepared by diluting Wnt 3A, R-spondin 2 and Noggin conditioned medium in advanced DMEM/F-12 basal medium and adding necessary nutrients and buffers. Final concentrations of each growth factor were Wnt 3A (80 ng/mL), R-spondin 2 (38

ng/mL), Noggin (36 ng/mL), GlutaMAX (1×), HEPES (10 mM), N-acetyl cysteine (1.25 mM), murine EGF (50 ng/mL), penicillin (100 unit/mL), streptomycin (100 μg/mL), and gentamicin (50 μg/mL). The concentration of Wnt 3A was determined by Wnt 3A ELISA kit (LifeSpan BioSciences, Inc, Seattle, WA). R-spondin 2 and Noggin growth factor concentrations were measured as described previously.[22] The assay medium contained the same nutrients and buffers in similar concentrations to SM except Wnt 3A (26 ng/mL), R-spondin 2 (30 ng/mL), and Noggin (56 ng/mL).

4.3.3 Generation of arrayed colonoids

A planar biomimetic scaffold comprised of Matrigel (protein concentration 9.2 mg/mL) was prepared in a multiwell plate. For a 96-well plate, 75 μL of Matrigel was dispensed to each well, and for 12-well Transwells® 200 μL Matrigel was dispensed to produce a Matrigel layer 2.4 mm thick. The plate was centrifuged for 1.5 min using 2000 rcf at 1 °C. The plate was transferred to a 37 °C cell culture incubator for 10 min for Matrigel gelation. To grow organoids on these surfaces, colonoids grown in a Matrigel patty were isolated by incubation with collagenase (Type IV, 500 U/mL) to break up the Matrigel. After release of the colonoids from the hydrogel, the colonoids were gently, mechanically dissociated. Fragmented colonoids (≤50 μm in diameter) containing cells derived from a WT or CAG Ds-Red mouse were added to the surface of a Matrigel-filled well as a suspension (120,000 cells) in SM. The number of cells in the isolated colonoids was calculated using CellTiter-Glo® luminescence cell viability assay (Promega US, Madison, WI) according to the manufacturer's protocol. Over the first 24 h in culture, colonoid fragments (≤50 μm diameter) were allowed to adhere to the Matrigel layer. Over the course of the subsequent 2-3 days, these fragments developed into colonoids ≥100 μm in diameter. Arrays were imaged using a Nikon Eclipse TE300 inverted epifluorescence microscope with an estimated

objective depth of field of >59 μm (N.A. 0.13) for comparison with 3D embedded cultures. The viability of colonoids after culturing 72 h on an array was measured using propidium iodide (PI) as a marker of cells death and Hoechst 33342 as a counterstain. After 72 h of culture 100% of the colonoids were viable.

4.3.4 Colonoid characterization

Colonoids were grown on the surface of Matrigel layered onto the membrane of a 12-well Transwell® insert. After culturing the colonoids for 3-days, the array was fixed using 4% paraformaldehyde for 25 min. The array was incubated with 30% sucrose for 3 h and kept in O.C.T. formulation overnight. The membrane was cut out of the insert and the tissue was sectioned using a cryostat to obtain 10-μm thick slices. These slices were stained using fluorescently-labeled phalloidin for F-actin (ActinGreen™ 488, Molecular Probes, Thermo Fisher Scientific, Waltham, MA) and Hoechst 33342, then imaged by fluorescence microscopy.

4.3.5 Cell lineages in arrayed colonoids

To mark S-phase cells, 5-ethynyl-2'-deoxyuridine (EdU, 10 μM in SM) was incubated on the arrays for 4 h. The arrays were then fixed in 4% paraformaldehyde for 20 min and incubated with 0.5% Triton X-100 for 20 min to facilitate diffusion of the labeling reagents into the cells. EdU-marked cells were then stained using Click-iT EdU Alexa Fluor 647 imaging kit (Thermo Fisher Scientific, Waltham, MA). Next the goblet cells were stained using rabbit anti-mucin2 (α-Muc2, 1:200, Santa Cruz Biotechnology, Inc, Dallas, Texas, #sc-15334).[26] A secondary antibody, Alexa Fluor 488 α-rabbit (1:500, Jackson Immunoresearch, West Grove, PA, # 711-545-152), was used to fluorescently label the primary antibody. Stained colonoids were imaged using a Nikon Eclipse TE300 inverted epifluorescence microscope with an estimated objective depth of field of >11 μm (N.A. 0.3).

4.3.6 Automated fluorescence imaging of arrayed colonoids

Automated imaging of arrayed colonoids was performed using an Olympus IX81 inverted epifluorescence microscope with a 4× objective (Olympus UPlanFL N, N.A. of 0.13 with an estimated objective depth of field of 40 μm) and a CoolSNAP HQ2 CCD camera (Photometrics, Tucson, AZ) or Hamamatsu Flash 4.0 VZ (Hamamatsu, Japan). Colonoids in this study were fluorescently labeled, either by labeling with Hoechst 33342 to stain DNA or by using colonoids derived from CAG-DsRed mouse model in which all cells expressed the DsRed fluorescent protein. For fluorescence imaging of DSRed and Hoechst 33342, a Chroma ET-YFP 49003, and Chroma ET-DAPI 49000 were used, respectively. The microscope was equipped with a humidified incubation chamber maintaining an environment at 5% CO_2 and 37 °C. All automated image acquisition was controlled by a custom MATLAB program (MATLAB 2014b, The MathWorks, Inc., Natick, MA) harnessing Micro-Manager microscopy software. Individual wells within plates were imaged using overlapping fields of view (*i.e.* a 6 × 4 image tiling to covering a single well of a 96-well plate).

Despite the curved shape of the Matrigel substrate (a concave meniscus measuring 595 ± 84 μm from top to bottom over a 2 × 2 mm area, mean ± standard deviation, n=3), well-focused images of the colonoid arrays were obtained in an automated fashion. Two strategies were combined to compensate for any curvature of the Matrigel surface upon which the arrayed colonoids were cultured. First, prior to image acquisition, an autofocus scan of the colonoid array was performed to determine focal positions for each desired imaging region throughout the array. A software-based autofocus was used that maximized the standard deviation of the pixel intensity in fluorescence images of the colonoids. The image standard deviation was chosen as a more rapid and robust metric of fluorescence image sharpness than other, typically gradient-based, methods.

To further guarantee well-focused images, 40% image overlap was employed during mosaicking and only the highly focused, central non-overlapped portion of each image was used for subsequent analysis. Once the imaging positions were determined utilizing these approaches, a 15 mm^2 area composed of 4 × 6 images with 40% overlap between fields was acquired for each well in 22 s. The 15 mm^2 area was chosen to avoid imaging too close to the well walls (well area: 32 mm^2 for 96-well plates).

4.3.7 Image analysis and assay metrics

All image analyses were performed using custom MATLAB scripts. The analyses began by forming full-well images by stitching together the well-focused central portions of the images from a well. Colonoids were identified by segmenting the Hoechst or DsRed fluorescent images using Otsu's automatic intensity thresholding.[27] For some colonoids the fluorescence labeling was dim, which interfered with basic intensity-thresholded segmentation. For these colonoids intensity thresholding did not detect the full colonoid boundary, and thus the segmentation was discontinuous when in reality the colonoids had an intact and continuous border. To compensate, a morphological closing operation using a disk of 19 μm radius (3 pixels) was applied. Objects below 100 μm in effective diameter were removed to eliminate debris, dead cells, and organoid fragments. Segmentation holes were filled and adjacent colonoids separated using a geometric watershed transform.[28] Colonoid centroids, areas, and mean fluorescence intensities were automatically recorded within the colonoid boundaries identified in the final segmentation masks.

In order to track colonoid properties over time, an algorithm was constructed to match the colonoids in the images acquired at different time points. Every identified colonoid's centroid was measured at each time point. When tracking colonoids over time, colonoids whose centroids varied less than 100 μm along the plane of the array and whose areas varied by less than 25% between

time-points were considered to be the same colonoid. In the event of temporal gaps in the tracking of a colonoid, the algorithm linearly interpolated colonoid measurements for up to 2 time points. Colonoids with 3 or more untracked time points were excluded from analysis.

Several metrics were used to quantify changes in colonoid size over time. The magnitude of the change in a colonoid's area was measured as the percent area increase relative to the initial area (ΔA expressed as a %) or maximal value of ΔA during the assay time (ΔA_{max} expressed as a %). The initial rate of size increase of colonoids was quantified as the slope of a linear fit (R^2>0.85) of area as a function of time. By assuming colonoids are spherical and swell isotropically, area rates of change could be converted into net fluid flux occurring between time points 1 and 2 according to: $flux_{1,2} = \frac{\left(\frac{V_2}{A_2} - \frac{V_1}{A_1}\right)}{t_2 - t_1}$, where V_i, and A_i, represent the colonoid volume and colonoid surface at time 1 and 2 (t_i). To cluster colonoid subpopulations, an expanded 10 dimensional data set was extracted per colonoid. Supervised clustering to classify individual colonoids into "non-responsive" (*i.e.* negative control-like) or "responsive" (*i.e.* positive control-like) groups was performed using a binary linear support vector machine classifier (MATLAB's fitcsvm).[29] See section 4.4.5 below for training details. Unsupervised clustering was performed using k-means clustering with k = 2. For classification, each dimension of the data was centered and scaled by the mean and standard deviation. Classification accuracy was estimated using 5 cross-validation folds.

4.3.8 Clustering analyses for determination of colonoid heterogeneity

To determine colonoid heterogeneity using clustering analyses, the size and swelling responses of each colonoid were evaluated using 10 metrics, which were calculated from measurements of the colonoid cross-sectional area over time. Although these 10 metrics were

chosen as a less redundant subset of >15 metrics, it should be noted that several metrics were still largely redundant for our data.

- A colonoid's general size was measured by its initial cross-sectional area (Metric #1) and its final cross-sectional area (Metric #2).
- The magnitude of a colonoid's swelling response was measured by the absolute difference in cross-sectional area between initial and final timepoints (Metric #3), the relative difference in area between initial and final timepoints, normalized by initial area (Metric #4), and the most extreme difference in colonoid area relative to the initial timepoint (highest or lowest), normalized by initial area (Metric #5).
- The kinetics of a colonoid's initial swelling response was measured by the slope of a linear fit to the relative area difference (normalized by initial area) over time data (Metric #6) and the R^2 value of the linear fit (Metric #7). The linear fit was performed using least-squares regression, and was fit to the longest linear ($R^2 > 0.85$) segment of the area trace starting at the initial timepoint. If no initial segment of at least 3 timepoints long could be fit with $R^2 > 0.85$, the line was instead fit to the full area trace.
- The distribution of a colonoid's size over time was measured by the colonoid's area distribution's sample variability (Metric #8), skewness (Metric #9), and kurtosis (Metric #10).

4.3.9 cAMP-stimulated transport

Colonoids at day 2 of growth on the array were used for all fluid transport assays since these colonoids are comprised primarily of stem/proliferative cells which are thought to play a major role in fluid secretion.[30] Wild type colonoids were stained with Hoechst 33342 (2 μM in assay medium) for 25 min. Forskolin was used for activation of adenylyl cyclase to increase the

intracellular cAMP concentration. Forskolin (1 μM), cholera toxin (C-T, 5 μg/mL or 0.5 μg/mL) or subunit B of C-T (C-B, 5 μg/mL or 0.5 μg/mL) in assay medium was added to arrayed colonoids which were then immediately imaged every 3 min for 1-1.5 h. DMSO in an amount equivalent to that in the added forskolin was added to control wells. The viability of colonoids after 48 h on the array with and without an additional 1 h forskolin challenge was measured using propidium iodide to assay dead cells and Hoechst 33342 as a counter stain. 100% of colonoids were viable in both the forskolin or DMSO treated samples.

4.3.10 Investigation of fluid movement using compounds of the enteric nervous and immune systems

Eight compounds that are known to be associated with cAMP or Ca^{2+}-regulated ion transport were assessed for the ability to induce fluid movement into the colonoids leading to colonoid swelling (Table 4.1). All compounds except forskolin were dissolved in 1× PBS or distilled water and diluted 1000× in assay medium prior to addition to the colonoids. Forskolin was dissolved in DMSO and diluted 1000× in assay medium. Addition of assay medium or DMSO (0.1%) was used as a control. After culturing for 2 days in SM, colonoids were stained with Hoechst 33342 for 25 min. The medium in each well was then replaced with the appropriate experimental or control medium and the plate was transferred to the microscope for time-lapse fluorescence imaging every 3.6 min for 32 min. Compound screening was performed in triplicate by culturing arrayed colonoids in three 96-well plates utilizing 16 wells within each plate: one for each of the 8 compounds to be screened, one each for the forskolin and cholera toxin positive and negative controls, respectively, five for the assay medium controls, and one for the DMSO control. To control for plate-to-plate variance, each plate used a random well order for the compounds.

4.3.11 Statistical analysis

Unless otherwise specified, data is presented as the sample mean and standard deviation. Two-tailed t-tests were utilized for comparisons between 2 groups. Statistical analyses of multiple experimental groups and controls were performed using one-way ANOVA and Tukey's test for multiple comparisons. For statistical analysis of multiple experimental groups between embedded and arrayed organoids, two-way unbalanced ANOVA with Type III sum of squares and Tukey's test for multiple comparisons was used. All statistical tests were performed at a significance level of 0.05 and were computed using MATLAB or GraphPad Prism (GraphPad Software, Inc. La Jolla, CA). G*Power software (Heinrich Heine University, Germany) was used to for *a priori* sample size determination based off of a two-tailed t-test for differences in ΔA_{max} of two groups with $\alpha=1-\beta=0.05$.

Box-and-whisker plots were used to show ΔA_{max} (%) of colonoids. The small box indicates the mean of the data, the bar shows the median, and the upper and lower boxes represent the 75^{th} and 25^{th} percentiles of the data, respectively. The whiskers extend to the 5^{th} and 95^{th} percentiles, and "x" denotes outliers. For all statistical comparisons, p values were represented as follows: * for $p<0.05$, ** for $p<0.01$, *** for $p<0.001$, and **** for $p<0.0001$.

4.4 Results and Discussion

4.4.1 Generation of a colonoid array and its characterization

To generate colonoid arrays, a protocol similar to that used to create acinar cultures from tumor cell lines was adapted for the primary intestinal epithelial organoids.[31,13] Colonoid fragments possessing proliferative cells were plated on the surface of a layer of polymerized Matrigel. Cells in the colonoids adhered to the upper surface of the Matrigel and expanded in size while remaining attached to the surface (Figure 4.1A,B). Under these conditions, 24 ± 11% (n =19) of the colonoid

diameter was embedded within the Matrigel with the remainder extending above the Matrigel surface into the overlying medium (Figure 4.1D). None of the colonoids (n=70) on the Matrigel surface overlapped in the Z dimension. In contrast, colonoids embedded in conventional 3D cultures were frequently found to overlap one another and reside in multiple focal planes throughout the gel (Figure 4.2). The polarity of the cell layer surrounding the colonoid lumen was investigated by fixing and cryosectioning the colonoids after 3 days of growth followed by staining F-actin with fluorescently-labeled phalloidin. F-actin was localized to the inner surface of the colonoid lumen suggesting that the actin-rich microvilli were also located on the luminal organoid surface and that the organoids were properly polarized (Figure 4.1C).[32]

Intestinal organoids consist of proliferative and differentiated cell types similar to those found *in vivo*. To identify cell lineages present in the arrayed colonoids, arrayed and embedded colonoids were pulsed with EdU to identify S-phase cells and immunostained for mucin 2 (Muc-2) to identify the differentiated goblet cells. Colonoids were imaged using a fluorescence microscope. The area of the colonoid displaying EdU-based or Muc-2 immunofluorescence was quantified and normalized to the total area of the organoid, *i.e.* the organoid image area positive for Hoechst 33342 fluorescence. Colonoids were cultured on the arrays in a medium rich in growth factors (SM) displayed an EdU+/Hoechst area of 47.2 ± 24.5% (n=27) suggesting large numbers of S-phase or proliferative cells (Figure 4.1E,G). The MUC-2+/Hoechst area was 0.5 ± 1.1 (n=29) indicating that few of the differentiated goblet cells were present under these culture conditions (Figure 4.1E,G). For comparison, Matrigel-embedded colonoids cultured in the presence of the SM possessed an EdU+/Hoechst area of 34.6 ± 22.0% (n=25) that was not significantly different from that of the arrayed colonoids (p=0.852) (Figure 4.1F,G). Similarly, the MUC-2+/Hoechst area for the embedded colonoids (0.3 ± 0.9%, n=25) was not significantly different than that of the

arrayed colonoids (p=0.486) (Figure 4.1F,G). Thus, the arrayed colonoids displayed similar numbers of proliferative and differentiated cells to that found in the embedded colonoids suggesting that the two organoid culture systems were similar. Additionally the large standard deviation in the area of EdU uptake and muc-2 immunostaining suggested that the colonoids might be quite heterogeneous in their properties in both culture systems.

4.4.2 Automated assay of colonoid arrays

Since the colonic organoids displayed heterogeneous behavior, significant sample sizes would likely be required to identify subpopulations and/or responses to some compounds. Thus, automated microscopy and image analysis were implemented so that hundreds of colonoids could be assayed per experiment. A motorized microscope acquired a grid of images spanning each well of a 96-well plate (Figure 4.3A). As the colonoids lay above the hydrogel surface and the structures did not overlap, autofocus routines could be applied to image the colonoid arrays (22 s/well). The images of each well were stitched together followed by application of an automated analysis pipeline (Figure 4.3A,B). The colonoids were segmented using Otsu's method for thresholding to create a mask for subsequent fluorescence measurements.[27] The masks were size-filtered to remove objects less than 60 μm in diameter and adjacent colonoids were separated using a watershed transform.[28] Colonoid centroids, areas, and mean fluorescence intensities were then quantified for the masked regions and these features as well as the colonoid location tracked over time.

To develop the automated platform, murine colonoids expressing DsRed were cultured on the arrays and imaged over 3 days. The wells contained a total of 214 colonoids (n=3 wells). The median colonoid diameter increased from 105.0 ± 12.8 μm to 139.0 ± 6.7 ($p < 0.02$) over the 3-day culture time (Figure 4.3C-E). Between days 2 and 3, the majority of the colonoids (52.6% ± 6.5%)

experienced a ≤25% increase in image plane-area (Figure 4.3D). The colonoids were nearly stationary over this time with an average linear velocity of 2.8 ± 0.3 μm per hour. A small percentage (9.4%) of the colonoid population displayed a >75% increase in image area during the 24 h time with the fastest growing colonoid expanding in area from 17,850 μm^2 to 36,237 μm^2 (equivalent diameter increase from 151 μm to 215 μm). Most of the colonoids (95%) displayed area growth rates <4.3%/h and absolute area growth rates <479 μm^2/h.

The performance of automated image analysis of colonoid area and position was evaluated from image data acquired between day 2 and 3 of culture (Figure 4.3F). The automated image analysis routines segmented and tracked 72.6% ± 7.9% of the wells' colonoids (154 colonoids across 3 wells). A goal of this work was to segment the entire colonoid without including adjacent colonoids during the 24-h analysis window. Only 5.2% ± 0.5% (11 colonoids in total) of the colonoids were segmented or tracked incorrectly by the automated software. This accuracy was attained at the expense of excluding 22.3% ± 7.7% (49 colonoids in total) of the colonoids based upon thresholds of allowable colonoid diameter, swelling rates, and centroid velocities. Both inaccurate measurements and colonoid exclusion occurred predominantly when the colonoids were clustered too densely for successful segmentation or possessed regions that fell below the fluorescence threshold for the mask. Notably, the array with the lowest colonoid density (4 colonoids/mm^2) exhibited the least instances of clustered colonoids and the highest rate of accurate analysis (81.7%). Thus, increasing the density beyond 4-6 colonoids/mm^2 may have diminishing returns on throughput when strict colonoid exclusion criteria are used in image analysis algorithms.

4.4.3 cAMP-regulated transport

Intracellular cAMP production initiates ion transport into the intestinal lumen, which is followed by the passive movement of water into the lumen. In the colonoids, ions and fluid move

into the enclosed lumen causing the structure to swell. To assess the cAMP-regulated transport, arrayed colonoids were stained with Hoechst 33342, stimulated with forskolin (0 or 1 μM), which is commonly used to stimulate the production of cAMP by adenylyl cyclase in cells. The colonoids were imaged over time using the automated platform, and Hoechst fluorescence was used to identify and segment the colonoids. Addition of forskolin to cells resulted in a visible increase in the colonoid diameter in less than 1 h while the DMSO control had no impact on the structures (Figure 4.4A,B). Colonoid area was tracked over time to determine net rate of fluid movement across the monolayer of colonic epithelial cells (Figure 4.4C-E). The percent maximal area increase, ΔA_{max}, of forskolin-treated colonoids was 21.2% [5.3%, 41.9%] (median [25^{th}, 75^{th} percentile], n=66 colonoids) relative to their area prior to forskolin addition (Supplemental Video S2). In contrast colonoids receiving media or DMSO demonstrated a ΔA_{max} of 1.1% [0%, 2.5%] and 1.4% [0%, 4.1%] (median [25^{th}, 75^{th} percentile], n_{media}=63 and n_{DMSO}=71 colonoids), respectively, which were both statistically different from the response of the forskolin-treated organoids ($p<0.0001$ for all comparisons). On average, colonoids achieved 75% of their maximal swelling within 23 min of forskolin addition and 100% of their maximal size within 46 min. The estimated maximal rate of fluid movement in forskolin-treated colonoids during the 1 h assay window was 4.23 ± 3.34 μL h^{-1} cm^{-2}, which was significantly different than that estimated for control colonoids (media addition, 1.50 ± 2.02 μL h^{-1} cm^{-2}; DMSO addition, 1.75 ± 1.93 μL h^{-1} cm^{-2}, $p<0.0001$ for all comparisons). The average initial net fluid flux was between 9-30% that of the average maximal net fluid flux for colonoids in media, DMSO, and forskolin. Overall, the fluid transport rate of arrayed colonoids treated with forskolin was comparable to that of 3D embedded cultures under the same conditions, which was 2.16 ± 0.55 μL h^{-1} cm^{-2}. These results suggested

that cAMP-regulated ion transport followed by passive water movement occurs in the arrayed colonoids.

The information-rich images of arrayed colonoids can be used for identification of heterogeneous behaviors after a perturbation such as application of a drug. For the forskolin-treatment experiment described above, each colonoid's size, swelling magnitude, and swelling kinetics were quantified using a panel of 10 metrics (see Methods). To identify treatment-dependent subpopulations of colonoids, the experimental dataset consisting of 66 forskolin-treated, 71 DMSO-treated, and 63 untreated colonoids was clustered into 2 groups using k-means clustering (Figure 4.4C,D). Forskolin-treated colonoids disproportionally fell into the "responder" cluster, which was composed exclusively of 30 forskolin-treated colonoids. The remaining 36 forskolin-treated and 134 non-forskolin treated organoids clustered into a "nonresponder" group. Forskolin-treated responders and non-responders possessed ΔA_{max} values of 47.7% [35.8%, 63.7%] and 7.6% [4.0%, 20.0%] (median [25^{th}, 75^{th} percentile]), respectively (Figure 4.4C,E). The DMSO-treated colonoid nonresponders exhibited ΔA_{max} values of 2.2% [0.5%, 6.0%] (Figure 4.4D,E). The maximum nonresponder ΔA_{max} was 20.5%, with 48% of forskolin-treated colonoids exceeding this swelling amount (8 nonresponders and 24 responders out of 66 total forskolin-treated colonoids) (Figure 4.4E). These data demonstrate the heterogeneity of colonoids swelling, even in response to the same stimulus, *i.e.* forskolin, a direct activator of adenylyl cyclase.

To further validate the swelling assay using arrayed colonoids, the repeatability of forskolin induced swelling using colonoids derived from four, wild-type mice (3 male, 1 female) was investigated (Figure 4.5). Arrayed colonoids grown from these mice were treated with forskolin while a control well received 0.1% DMSO-containing medium only. The median ΔA_{max} of forskolin-treated colonoids from the four mice were 28.8% [20.5%, 33.1%], 15.1% [8.5%, 24.2%],

7.5% [2.7%, 14.5%], and 20.2% [9.4%, 28.8%] while the matching percent ΔA_{max} for the DMSO control from these mice was 7.4% [4.3%, 10.3%], 5.6% [3.3%, 9.9%], 2.4% [0.9%, 4.9%], and 4.1% [0.1%, 6.9%] (median [25th percentile, 75th percentile]), respectively. The mean ΔA_{max} of all three samples was significantly different from their respective DMSO control (two-way ANOVA, $p<10^{-7}$ for all comparisons) as well as between all four mice except between mice 1 and 4 ($p<0.05$ for all comparisons) (Figure 4.5). While a functional variation between animal tissues can be expected, colonoid swelling did increase across all forskolin-treated samples relative to the paired DMSO control.

The dose dependence of forskolin-induced swelling in arrayed colonoids was then investigated and compared to embedded cultures using colonoids from the same mouse. Both arrayed and embedded colonoids demonstrated a dose-dependent swelling for forskolin concentrations of 50 nM to 5 μM (Figure 4.6A). The dose responses were fit to sigmoidal logistic functions using nonlinear regression with least-squares estimation (Figure 4.6B). For arrayed colonoids, the EC50 and maximal relative area increase of forskolin-induced swelling were 175.7 nM (95% c.i.= [52.4, 299.0] nM) and 344% (95% c.i.= [279, 410] %), respectively. These metrics were not significantly different from the EC50 and maximum response of embedded colonoids from the same mouse, which were 232.4 nM (95% c.i.= [106.9, 357.9] nM) and 284% (95% c.i.= [248, 321] %), respectively. Thus, overall forskolin-induced swelling in arrayed colonoids was similar to that of hydrogel-embedded cultures.

The dose-dependence response to forskolin permits an estimate of the number of colonoids needed to obtain a statistically significant swelling response as the forskolin concentration is altered. The lowest forskolin concentration that induced a statistically different response relative to the control was 250 nM ($p<0.001$, two-way ANOVA), which induced a 2.1 and 2.6-fold

increases in the median ΔA_{max} over the DMSO control for embedded and arrayed colonoids, respectively. Based off these data, the estimated total sample size required to detect statistically significant differences between the ΔA_{max} of forskolin and DMSO-treated colonoids is 2868 for the expected 1.2× difference, 322 for a 1.5× difference, 80 for a 2.8× difference and 42 for a 2.9× difference. Thus even for a moderate level of swelling (1.5-fold size increase), hundreds of colonoids must be screened for statistical confidence. The use of arrayed organoid strategy enables the assay of sufficient colonoids for these biologically-relevant swelling conditions.

4.4.4 Investigation of fluid secretion by cholera toxin

Cholera is a well-known toxin that causes persistent diarrhea through cAMP production as well as activation of enteric nervous and immune systems. The toxin consists of two units, cholera toxin A and B. The combined toxin A & B (CT) is required to activate adenylyl cyclase and produce cAMP.[1] The B subunit of cholera toxin (C-B) binds to intestinal epithelial cells but does not stimulate cAMP production.[33] The impact of cholera toxin on colonoid arrays was investigated by adding CT, C-B, or media to the cultures and applying the automated platform to track the colonoids over time. CT at both 0.5 µg/mL and 5 µg/mL induced a significantly greater increase in the ΔA_{max} than the media control, 0.5 µg/mL C-B, or 5 µg/mL C-B ($p<0.01$ for all comparisons, Figure 4.7A). There was no statistical difference between wells treated with media alone and wells treated with 0.5 µg/mL C-B or 5 µg/mL C-B (Figure 4.7A). These data demonstrate the utility of the arrayed organoid platform in the measurement of cellular responses to enterotoxins.

4.4.5 Screening of compounds associated with the enteric nervous and immune systems during infectious diarrhea

Cell-enterotoxin interactions can activate enteric nervous and immune systems to produce compounds that induce ion transport or inhibit ion absorption with subsequent water movement

producing diarrhea and significance water loss through the colon.[1] To investigate the potency of such compounds on fluid transport on intestinal cells, 8 compounds (bradykinin, prostaglandin E2, vasoactive intestinal peptide, adenosine, serotonin, acetylcholine, and histamine) generated by enteric nerves or inflammatory cells during infectious diarrhea were selected for screening on the primary arrayed colonoids (Table 4.1).[1] Colonoids at day 2 of culture were incubated with the compounds for 32 min while undergoing time-lapse imaging. Forskolin was used as a positive control while culture media and C-B were included as negative controls. Automated image analysis enabled each colonoid's size, swelling magnitude, and swelling kinetics to be quantified using a panel of 10 metrics. This rich dataset was then processed to analyze unique subpopulations. Support vector machine (SVM) classification was used to distinguish between responsive and non-responsive colonoids. For each well-plate replicate, the forskolin-treated positive controls and standard media negative controls were used to train a linear SVM binary classifier, which had an estimated cross-validation accuracy of 91.3% – 94.5% when distinguishing between swelling responders and static non-responders. The effects of the screened compounds on individual colonoid area and resulting classification for a single well plate are shown in Figure 4.7B-C. For the PGE2-treated sample, a large number of colonoids were identified as responders (49.6% ± 17.9%, total of 70 out of 139) (Figure 4.7B,C). This PGE2-responsive subpopulation possessed a greatly increased median ΔA_{max} (16.2%) compared to that of PGE2-nonresponders (median ΔA_{max} of 4.6%). PGE2 is known to be produced during infection with *Vibrio cholerae* leading to an increase in cAMP.[34,35] These results show that colonoids in the cultures were not functionally equal. Previously, the Magness group has shown the transcriptional heterogeneity of small intestinal organoids within the same culture.[36] Small numbers of colonoids treated with compounds other than forskolin or PGE2 were classified as responders (1.9%, or 37 out of 1955 colonoids)

(Figure 4.7B,C). These responding colonoids could represent unique subpopulations within colonoids, but larger numbers of colonoids would need to be tracked to ascertain whether such subpopulations exist. Overall, these data support the utility of the arrayed colonoids when combined with automated imaging and computation as a screening platform to identify the intestinal response to exogenous compounds such as drugs and toxins.

4.5 Conclusions

This paper demonstrates the development of an arrayed colonoid culture system on the surface of a hydrogel support. The colonoids resided on a locally flat surface such that efficient automated imaging was possible using a computer-controlled microscope. Moreover, the cell types and polarity of the arrayed organoids were indistinguishable from hydrogel-embedded organoids. Using simple and accessible automated image analysis methods, the positions and sizes of individual colonoids were measured over time frames as long as 72 hours. Using this approach, the net fluid movement across the epithelial cell monolayer of the organoids was tracked and quantified using the colonoid cross-sectional area as a proxy. This image-based tracking of organoid swelling was used to screen a small set of physiologic molecules associated with the enteric nervous and immune system for their impact on water movement across the colonoid epithelium. Heterogeneity in organoid response to chemicals such as forskolin and PGE2, and toxins such as cholera was readily observed. For example, PGE2-treated colonoids displayed a responsive subpopulation that possessed 3.5× higher response compared to that of PGE2-nonresponders. To detect smaller swelling responses *i.e.* from 1 to 2 fold that of the control, hundreds to thousands of colonoids are required to identify statistically significant responses. This arrayed colonoid system readily permits large numbers of organoids to be assayed enabling small subpopulations to be identified. In this instance, 2248 colonoids were assayed in less than 4 h for

the compound screen. Great utility is anticipated for this arrayed colonoid culture in applications involving screens of drugs, bacterial products, and dietary metabolites on primary intestinal tissue. Further, this platform can be readily extended to culture human intestinal organoids for personalized medicine applications.

4.6 Figures

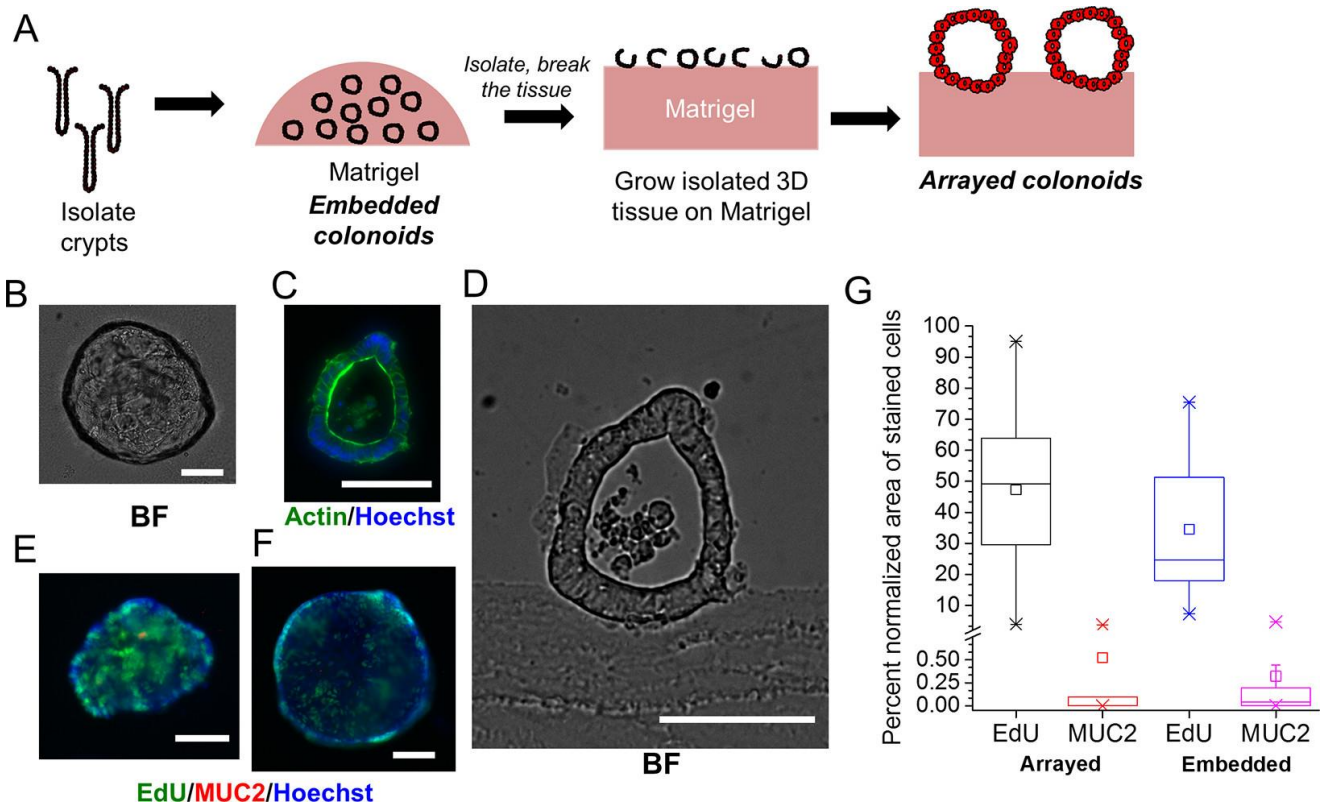

Figure 4.1 Generation and characterization of arrayed colonoids and comparison to embedded colonoids. (A) Work flow for generating the arrayed colonoids. (B) Brightfield image of an individual colonoid within the array. (C) F-actin (green) and Hoechst (blue) stained cryo-sectioned image of an arrayed colonoid. (D) Cryo-sectioned brightfield image of an arrayed colonoid. (E) & (F) EdU (green), MUC2 (red) and Hoechst (blue) stained images of an arrayed colonoid (E) and embedded colonoid (F). (G) Percent normalized area positive for EdU or MUC2 fluorescence in arrayed and embedded organoids. All scale bars represent 75 µm.

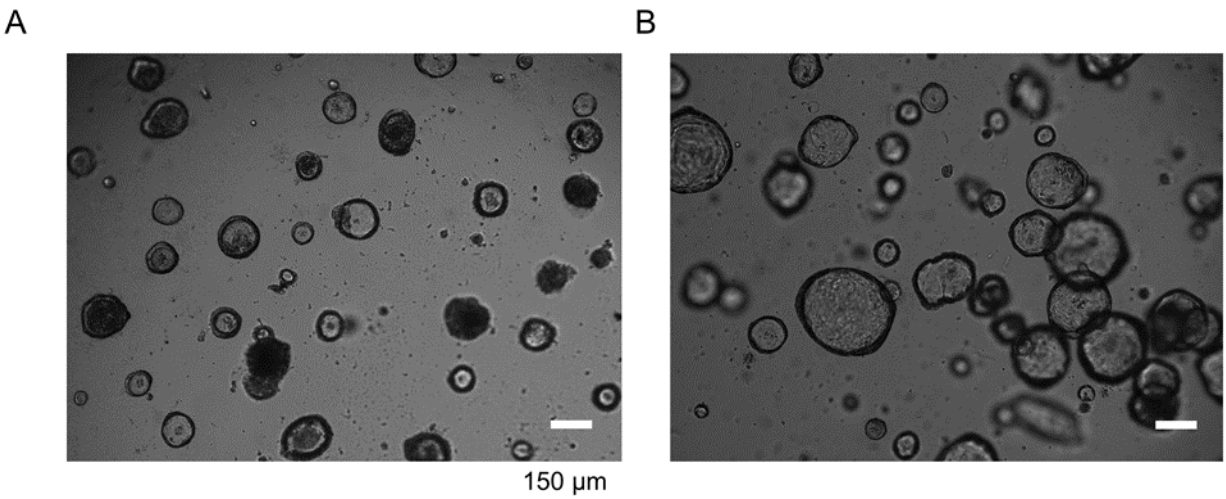

Figure 4.2 Brightfield images colonoids. Shown are images of (A) arrayed and (B) embedded colonoids at day 2 of culture.

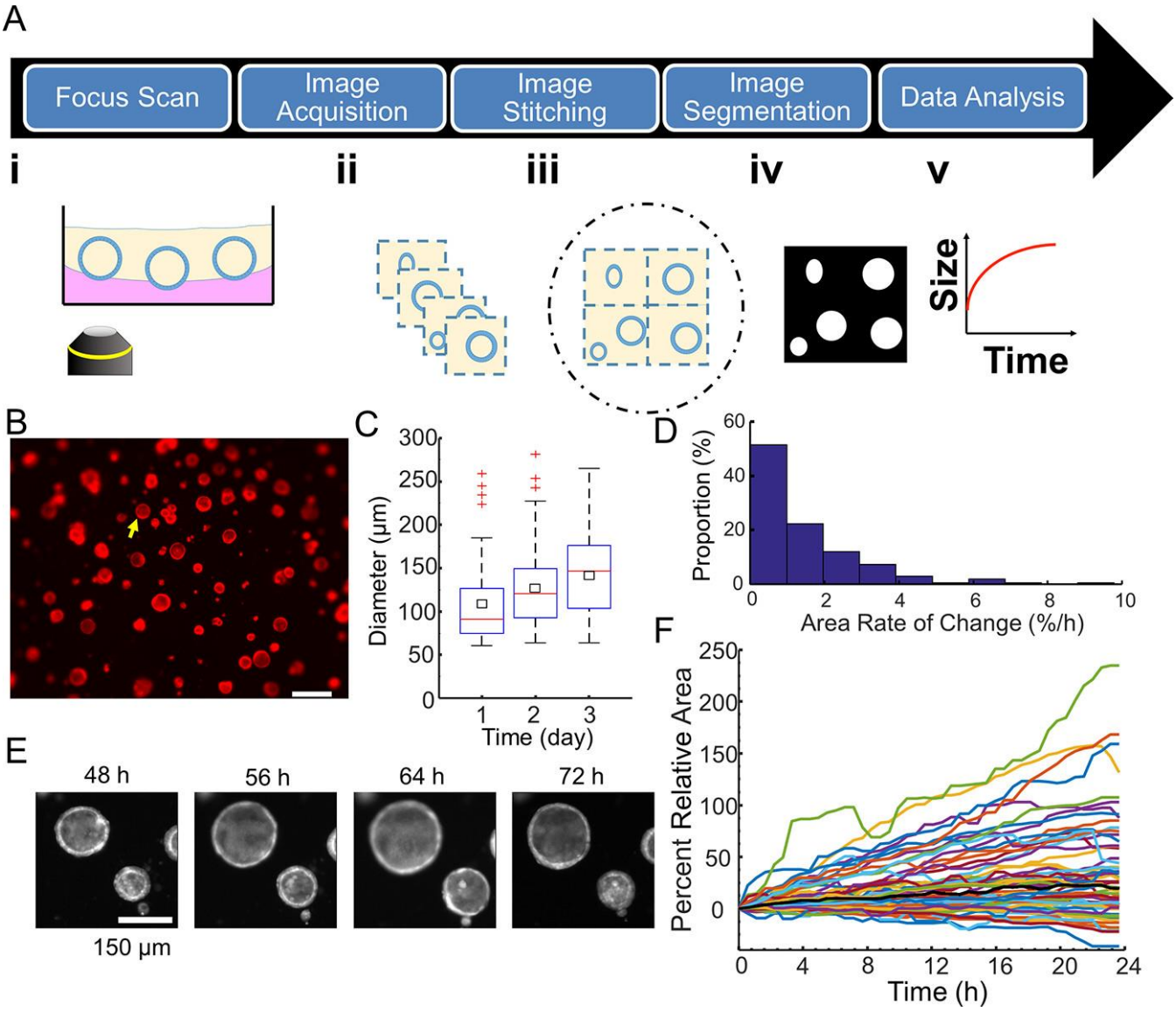

Figure 4.3 Automated imaging and image analysis. (A) Work flow of automated image acquisition and analysis. i: Arrayed colonoids are imaged over time using a motorized widefield microscope. ii: A top-view image of each colonoids is obtained. iii: The images of the colonoids are stitched into a single image per well (black dash-dotted line represent well perimeter). iv: Colonoids are segmented using automated image analysis to produce a binary map of each colonoid. v: Assay metrics such as colonoid size over time are extracted. (B) Stitched, full-well image showing DsRed fluorescence of colonoids after 3 days of growth on the array. The scale bar represents 500 µm.

(C) Box-and-whisker distributions of colonoid diameter over time. (D) Histogram of percent of colonoids versus their percent area rate of change (%/h). (E) A time series of DsRed fluorescence images of the single colonoid indicated by the yellow arrow in panel (B). (F) Change in colonoid cross-sectional area over time, relative to time zero. Each trace represents a single colonoid (n=62 colonoids), with the population median colonoid swelling represented by the black trace.

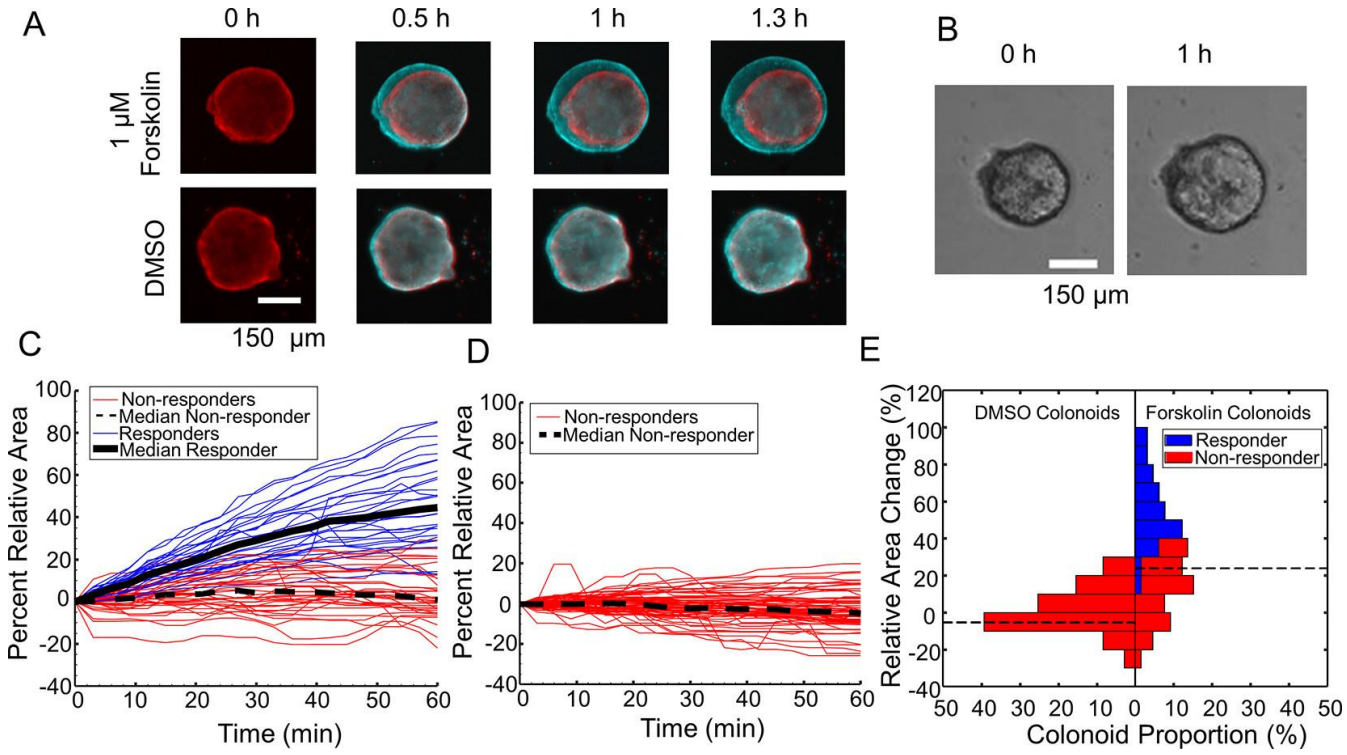

Figure 4.4 Colonoid swelling initiated by forskolin. (A) A time series of composite DsRed fluorescence images over 1.3 h (time 0: red; other time points: cyan) of a colonoid on an array after addition of forskolin or DMSO at time zero. (B) Brightfield images of a colonoid after addition of forskolin (1 μM) at zero. (C) & (D) Shown is ΔA of the colonoids over time. Forskolin ((C), 1 μM) or DMSO ((D), 0.1%) was added at time zero. k-means clustering with k = 2 was performed to classify the population into nonresponders (red) and responders (blue). (E) A comparison of ΔA versus the number of colonoids treated with forskolin or DMSO for the data in panels (C) and (D).

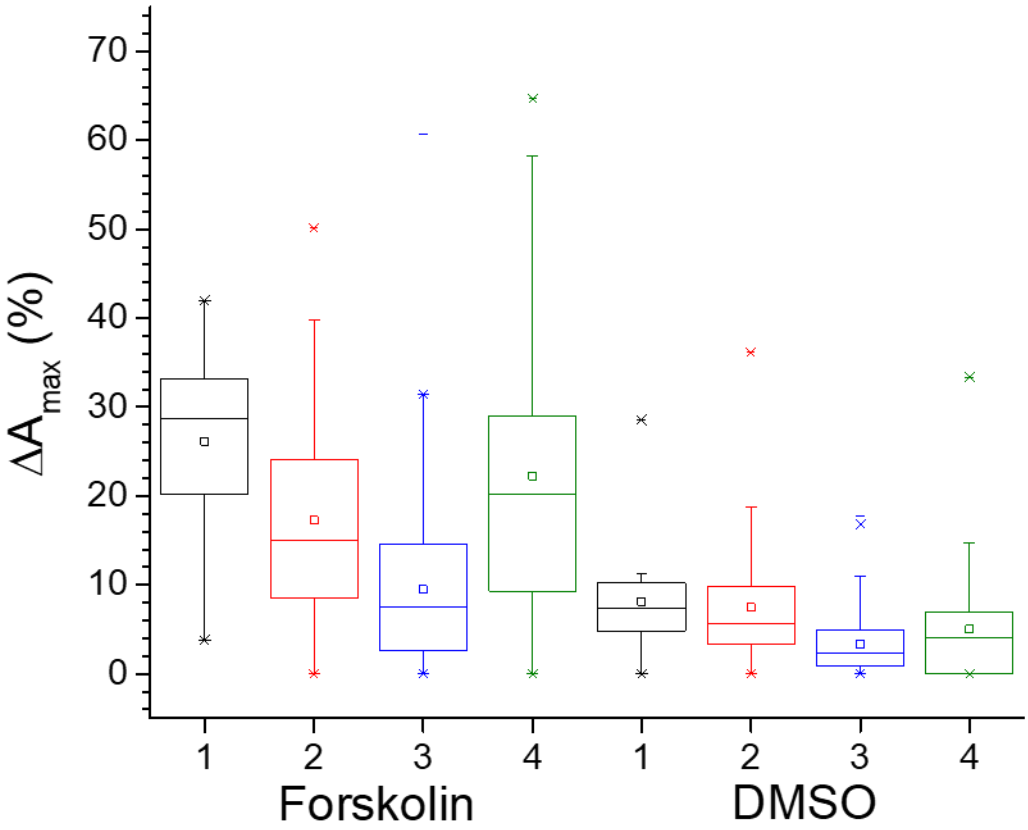

Figure 4.5 A comparison of swelling assay performance. Arrays were generated with colonoids from 4 different wildtype mice (1-3 male, 4-female). Added compounds were forskolin (1 µM) and DMSO (0.1%). All pairwise comparisons are statistically significant ($p < 0.05$), with the exception of Mouse 1 DMSO *vs.* Mouse 2 DMSO, Mouse 1 DMSO *vs.* Mouse 3 DMSO, Mouse 1 DMSO *vs.* Mouse 4 DMSO, Mouse 2 DMSO vs. Mouse 4 DMSO, Mouse 3 DMSO *vs.* Mouse 4 DMSO, Mouse 1 DMSO *vs.* Mouse 3 Forskolin, Mouse 2 DMSO *vs.* Mouse 3 Forskolin, Mouse 3 Forskolin *vs.* Mouse 4 DMSO, and Mouse 4 Forskolin *vs.* Mouse 1 Forskolin.

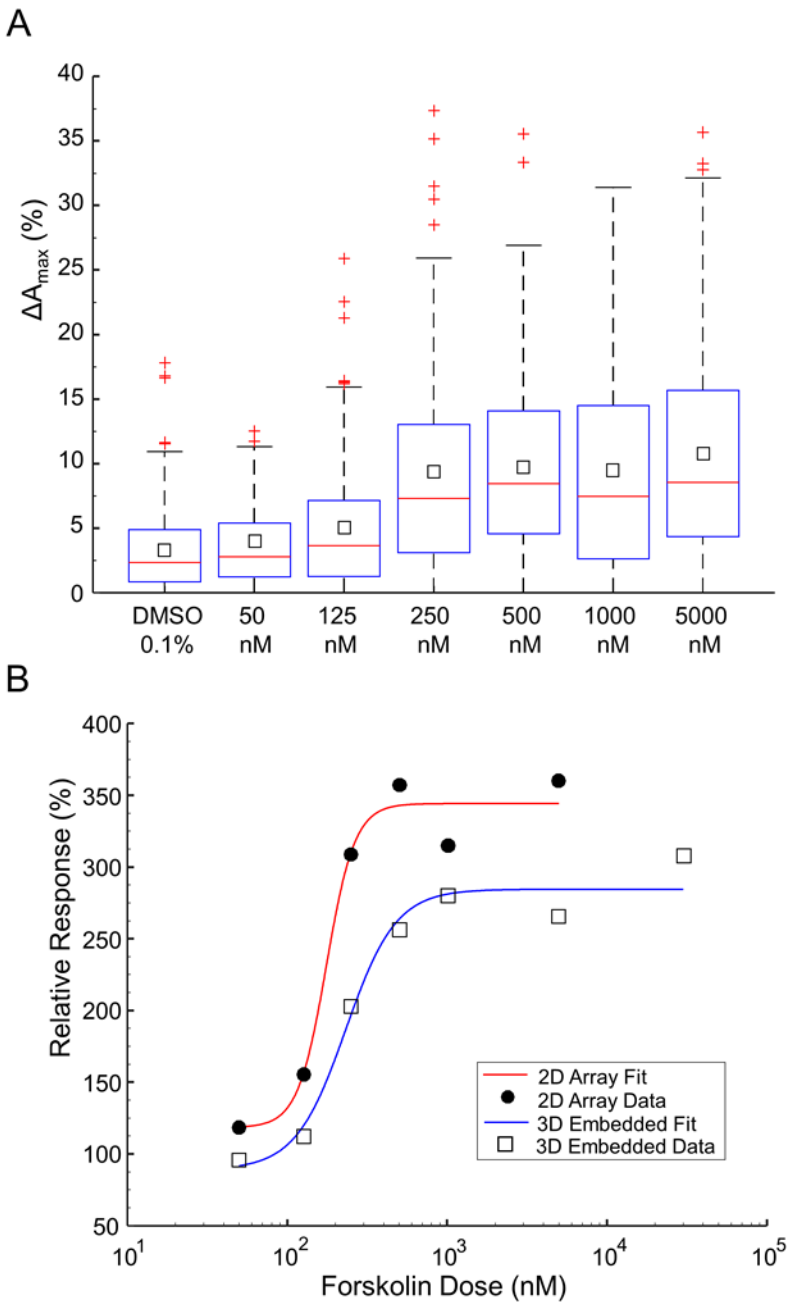

Figure 4.6 Dose dependence of forskolin-induced swelling. (A) ΔA_{max} of arrayed colonoids incubated with varying forskolin concentrations for 1 h. (B) ΔA_{max} of arrayed (closed black circles) and embedded (open squares) colonoids incubated with varying concentrations of forskolin. The dose responses were fit to sigmoidal logistic functions using nonlinear regression with least-squares estimation.

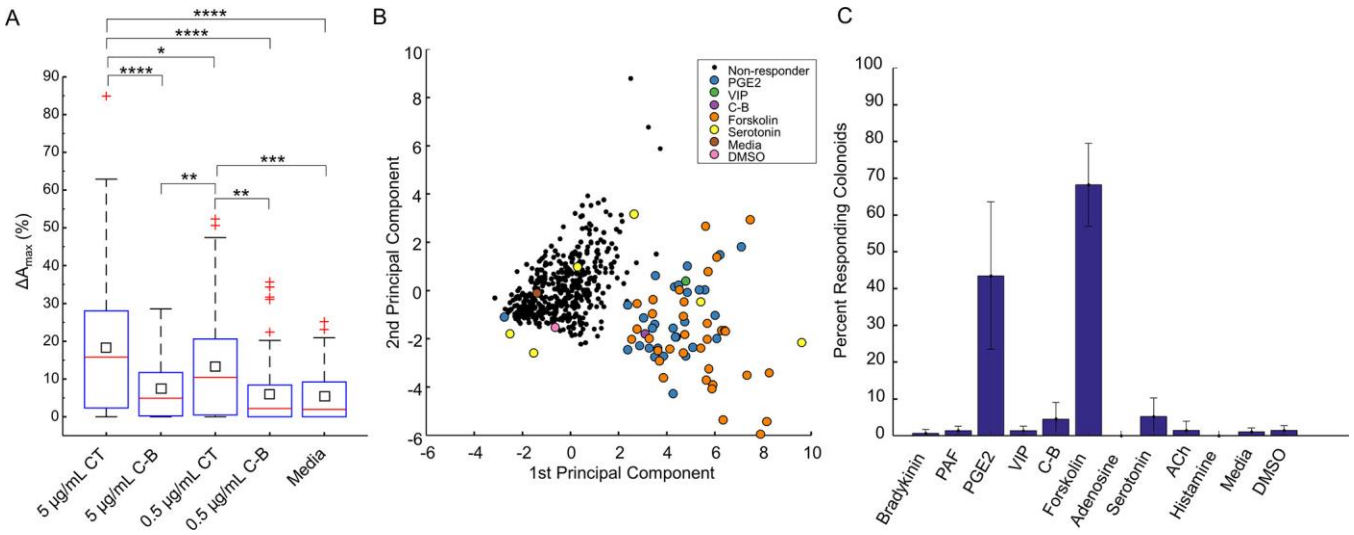

Figure 4.7 Colonoid swelling initiated by CT and compounds associated with the enteric nervous and immune systems. **(**A) Box-and-whisker plots of the maximal area attained by colonoids as a percentage of their area at time zero. The colonoids were incubated with CT or its B subunit at the indicated concentrations for 1.5 h. Colonoid responses to CT, C-B and assay medium was statistically compared. (B) 2-D reduction of a 10-dimensional colonoid dataset using principal component analysis. The data set consisted of 768 colonoids across 16 wells of a 96 well plate treated with 8 compounds and 4 controls. For clarity, the non-responding colonoids in negative control media are omitted. All non-responding colonoids are shown in black, whereas colonoids with forskolin-like swelling responses are shown color-coded by treatment compound. (C) Proportion of colonoids that exhibit swelling within a 32 min window in response to compound treatment. Error bars represent ±1 standard deviation using 3 replicate experiments. An SVM classifier was trained for each replicate experiment using that replicate's forskolin-treated and control colonoids as the classification's positive and negative training groups, respectively.

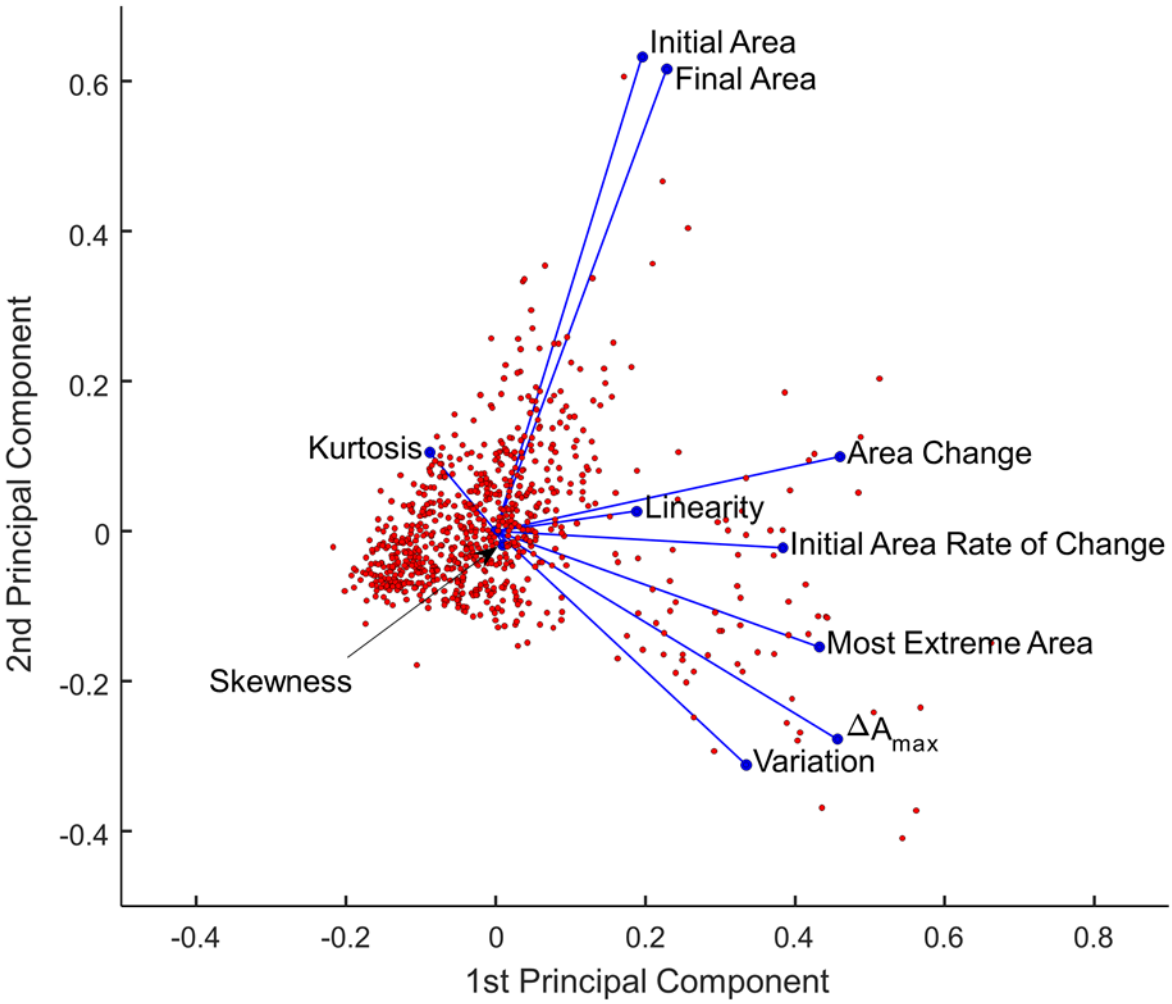

Figure 4.8 Principal component analysis. Shown are both the orthonormal principal component coefficients for each variable and the principal component scores for each observation from one of 3 replicate experimental datasets of compound-induced colonoid swelling. Shown is a 2-D reduction of one of the three 10-D datasets, which was extracted from 768 colonoids across 16 wells of a 96 well plate treated with 8 compounds and 4 controls. The orthonormal principal components coefficients for each of the 10 colonoid metrics are indicated by the blue vectors. Each red dot represents the normalized principal component score of one observed colonoid.

4.7 Tables

Table 4.1 Compounds with impact on colonoid swelling

Compound number	**Compound name**	**Receptor/ transporter**	**Screened concentration**
1	Bradykinin	B2	100 nM
2	Platelet activating factor (PAF)	PAF	100 μM
3	Prostaglandin E2	E	5 μM
4	Vasoactive intestinal polypeptide (VIP)	VIP	60 μM
5	Adenosine	Adenosine	100 μM
6	Serotonin (5-hydroxytryptamine) (5-HT)	Serotonin transporter	50 nM
7	Acetylcholine (ACh)	Muscarinic	300 μM
8	Histamine	Histamine H1	9 mM
9	Forskolin	Non-receptor based	1 μM
10	Cholera B sub unit (C-B)	GM1 gangliosides	0.5 μg/mL
11,12,13, 14,15	Assay medium		
16	DMSO		0.1%

4.8 REFERENCES

(1) Field, M. Intestinal Ion Transport and the Pathophysiology of Diarrhea. *J. Clin. Invest.* **2003**, *111* (7), 931–943.

(2) O'neal, C. J.; Jobling, M. G.; Holmes, R. K.; Hol, W. G. J. Structural Basis for the Activation of Cholera Toxin by Human ARF6-GTP. *Science (80-.).* **2005**, *309* (5737), 1093–1096.

(3) Hodges, K.; Gill, R. Infectious Diarrhea: Cellular and Molecular Mechanisms. *Gut Microbes* **2010**, *1* (1), 4–21.

(4) Greger, R. Role of CFTR in the Colon. *Annu. Rev. Physiol.* **2000**, *62* (1), 467–491.

(5) Thiagarajah, J. R.; Verkman, A. Chloride Channel-Targeted Therapy for Secretory Diarrheas. *Curr. Opin. Pharmacol.* **2013**, *13* (6), 888–894.

(6) Muanprasat, C.; Chatsudthipong, V. Cholera: Pathophysiology and Emerging Therapeutic Targets. *Future Med. Chem.* **2013**, *5* (7), 781–798.

(7) Grabinger, T.; Luks, L.; Kostadinova, F.; Zimberlin, C.; Medema, J. P.; Leist, M.; Brunner, T. Ex Vivo Culture of Intestinal Crypt Organoids as a Model System for Assessing Cell Death Induction in Intestinal Epithelial Cells and Enteropathy. *Cell Death Dis.* **2014**, *5* (5), e1228.

(8) Shamir, E. R.; Ewald, A. J. Three-Dimensional Organotypic Culture: Experimental Models of Mammalian Biology and Disease. *Nat. Rev. Mol. Cell Biol.* **2014**, *15* (10), 647–664.

(9) Ranga, A.; Gjorevski, N.; Lutolf, M. P. Drug Discovery through Stem Cell-Based Organoid Models. *Adv. Drug Deliv. Rev.* **2014**, *69–70*, 19–28.

(10) Sato, T.; Vries, R. G.; Snippert, H. J.; Wetering, M.; Barker, N.; Stange, D. E.; Es, J. H.; Abo, A.; Kujala, P.; Peters, P. J. Single Lgr5 Stem Cells Build Crypt Villus Structures in Vitro without a Mesenchymal Niche. *Nature* **2009**, *459* (7244), 262–265.

(11) Dekkers, J. F.; Wiegerinck, C. L.; Jonge, H. R.; Bronsveld, I.; Janssens, H. M.; Winter-de Groot, K. M.; Brandsma, A. M.; Jong, N. W. M.; Bijvelds, M. J. C.; Scholte, B. J.; et al. A Functional CFTR Assay Using Primary Cystic Fibrosis Intestinal Organoids. *Nat. Med.* **2013**, *19*, 939–945.

(12) Yamada, K. M.; Cukierman, E. Modeling Tissue Morphogenesis and Cancer in 3D. *Cell* **2007**, *130*, 601–610.

(13) Debnath, J.; Brugge, J. S. Modelling Glandular Epithelial Cancers in Three-Dimensional Cultures. *Nat. Rev. Cancer* **2005**, *5*, 675–688.

(14) Zietek, T.; Rath, E.; Haller, D.; Daniel, H. Intestinal Organoids for Assessing Nutrient Transport, Sensing and Incretin Secretion. *Sci. Rep.* **2015**, *5*, 16831.

(15) Mizutani, T.; Nakamura, T.; Morikawa, R.; Fukuda, M.; Mochizuki, W.; Yamauchi, Y.; Nozaki, K.; Yui, S.; Nemoto, Y.; Nagaishi, T. Real-Time Analysis of P-Glycoprotein-Mediated Drug Transport across Primary Intestinal Epithelium Three-Dimensionally Cultured in Vitro. *Biochem. Biophys. Res. Commun.* **2012**, *419* (2), 238–243.

(16) Schwank, G.; Koo, B.-K.; Sasselli, V.; Dekkers, J. F.; Heo, I.; Demircan, T.; Sasaki, N.; Boymans, S.; Cuppen, E.; Ent, C. K.; et al. Functional Repair of CFTR by CRISPR/Cas9 in Intestinal Stem Cell Organoids of Cystic Fibrosis Patients. *Cell Stem Cell* **2013**, *13*, 653–658.

(17) Jin, B.-J.; Battula, S.; Zachos, N.; Kovbasnjuk, O.; Fawlke-Abel, J.; In, J.; Donowitz, M.; Verkman, A. S. Microfluidics Platform for Measurement of Volume Changes in Immobilized Intestinal Enteroids. *Biomicrofluidics* **2014**, *8* (2), 24106.

(18) Moon, C.; Zhang, W.; Ren, A.; Arora, K.; Sinha, C.; Yarlagadda, S.; Woodrooffe, K.; Schuetz, J. D.; Valasani, K. R.; Jonge, H. R.; et al. Compartmentalized Accumulation of cAMP near Complexes of Multidrug Resistance Protein 4 (MRP4) and Cystic Fibrosis Transmembrane Conductance Regulator (CFTR) Contributes to Drug-Induced Diarrhea. *J. Biol. Chem.* **2015**, *290* (18), 11246–11257.

(19) Fujii, S.; Suzuki, K.; Kawamoto, A.; Ishibashi, F.; Nakata, T.; Murano, T.; Ito, G.; Shimizu, H.; Mizutani, T.; Oshima, S.; et al. PGE2 Is a Direct and Robust Mediator of Anion/fluid Secretion by Human Intestinal Epithelial Cells. *Sci. Rep.* **2016**, *6* (1), 1–15.

(20) Foulke-Abel, J.; In, J.; Kovbasnjuk, O.; Zachos, N. C.; Ettayebi, K.; Blutt, S. E.; Hyser, J. M.; Zeng, X.-L.; Crawford, S. E.; Broughman, J. R.; et al. Human Enteroids as an *Ex-Vivo* Model of Host–pathogen Interactions in the Gastrointestinal Tract. *Exp. Biol. Med.* **2014**, *239* (9), 1124–1134.

(21) Spence, J. R. Clocking the Pace of Organoid Research. *Cell. Mol. Gastroenterol. Hepatol.* **2017**, *4* (1), 203–204.

(22) Wang, Y.; DiSalvo, M.; Gunasekara, D. B.; Dutton, J.; Proctor, A.; Lebhar, M. S.; Williamson, I. A.; Speer, J.; Howard, R. L.; Smiddy, N. M.; et al. Self-Renewing Monolayer of Primary Colonic or Rectal Epithelial Cells. *CMGH* **2017**, *4* (1), 165–182.e7.

(23) Gracz, A. D.; Ramalingam, S.; Magness, S. T. Sox9 Expression Marks a Subset of CD24-Expressing Small Intestine Epithelial Stem Cells That Form Organoids in Vitro. *AJP Gastrointest. Liver Physiol.* **2010**, *298* (5), G590–G600.

(24) Ahmad, A. A.; Wang, Y.; Gracz, A. D.; Sims, C. E.; Magness, S. T.; Allbritton, N. L. Optimization of 3-D Organotypic Primary Colonic Cultures for Organ-on-Chip Applications. *J. Biol. Eng.* **2014**, *8* (1), 1–10.

(25) Miyoshi, H.; Stappenbeck, T. S. In Vitro Expansion and Genetic Modification of Gastrointestinal Stem Cells in Spheroid Culture. *Nat. Protoc.* **2013**, *8* (12), 2471–2482.

(26) Ramalingam, S.; Daughtridge, G. W.; Johnston, M. J.; Gracz, A. D.; Magness, S. T. Distinct Levels of Sox9 Expression Mark Colon Epithelial Stem Cells That Form Colonoids in Culture. *Am. J. Physiol. - Gastrointest. Liver Physiol.* **2011**, *302* (1), G10–G20.

(27) Otsu, N. A Threshold Selection Method from Gray-Level Histograms. *Automatica* **1975**, *11* (285–296), 23–27.

(28) Roerdink, J. B. T. M.; Meijster, A. The Watershed Transform: Definitions, Algorithms and Parallelization Strategies. *Fundam. informaticae* **2000**, *41* (1, 2), 187–228.

(29) Schölkopf, B.; Smola, A. J. *Learning with Kernels: Support Vector Machines, Regularization, Optimization, and beyond*; MIT press, 2002.

(30) Rao, M. C.; Sarathy, J.; Sellin, J. H. Intestinal Electrolyte Absorption and Secretion. In *Sleisenger and Fordtran's Gastrointestinal and Liver Disease*; Chapter 101; 2016; pp 1713–1735.

(31) Debnath, J.; Muthuswamy, S. K.; Brugge, J. S. Morphogenesis and Oncogenesis of MCF-10A Mammary Epithelial Acini Grown in Three-Dimensional Basement Membrane Cultures. *Methods* **2003**, *30*, 256–268.

(32) Ubelmann, F.; Chamaillard, M.; El-Marjou, F.; Simon, A.; Netter, J.; Vignjevic, D.; Nichols, B. L.; Quezada-Calvillo, R.; Grandjean, T.; Louvard, D.; et al. Enterocyte Loss of Polarity and Gut Wound Healing Rely upon the F-Actin-Severing Function of Villin. *Proc. Natl. Acad. Sci.* **2013**, *110* (15), E1380–E1389.

(33) Sánchez, J.; Holmgren, J. Cholera Toxin — A Foe & a Friend. *Indian J. Med. Res.* **2011**, *133* (2), 153–163.

(34) Hecht, G. Innate Mechanisms of Epithelial Host Defense: Spotlight on Intestine. *Am. J. Physiol. Physiol.* **1999**, *277* (3), C351–C358.

(35) Dey, I.; Lejeune, M.; Chadee, K. Prostaglandin E2 Receptor Distribution and Function in the Gastrointestinal Tract. *Br. J. Pharmacol.* **2006**, *149* (6), 611–623.

(36) Gracz, A. D.; Williamson, I. A.; Roche, K. C.; Johnston, M. J.; Wang, F.; Wang, Y.; Attayek, P. J.; Balowski, J.; Liu, X. F.; Laurenza, R. J.; et al. A High-Throughput Platform for Stem Cell Niche Co-Cultures and Downstream Gene Expression Analysis.

CHAPTER 5: SIGNIFICANCE AND FUTURE AIMS

5.1 Dissertation Summary

This dissertation described three interrelated research projects. Chapter 2 described the development of microfabrication of tensioned membranes and mathematical modeling of the deformation of membrane-based microarrays, which together enabled automated microscopy of microraft arrays and their adhered cells. Chapter 3 pertained to technology development toward a system for automated monitoring and splitting of human induced pluripotent stem cells. Lastly, Chapter 4 detailed the application of automated image analysis and pattern recognition to screen diarrhetic compounds on stem cell derived colonic organoids. In broad terms, the common theme connecting these projects was the development and application of automated technologies to enable the microscale analysis of biological samples. The combination of laboratory automation and biological image analysis resulted in powerful, high-throughput research tools for stem cell analysis, sorting, and screening. Below, the scientific impact (Section 5.2) and future directions (Section 5.3) of this dissertation's research are explored. For brevity, the discussion has been limited to the most notable scientific impacts and to the immediate future directions of the research.

5.2 Significance

5.2.1 Membrane Transfer Microfabrication

The "membrane transfer" microfabrication reported in Chapter 2 is a novel way to imbue tension in thin materials. The simple addition of a temporary substrate allowed the storage of enough tension within microarray membranes and more than an order of magnitude reduction to the membrane deflection. While the effectiveness of the method was demonstrated for Sylgard 184

polydimethylsiloxane (PDMS) membranes, its principle of action is expected to be similar for membranes composed of other vulcanizable materials. Mechanical stretching represents an alternative method to pre-tension membranes; however, a major downside of this method is that it warps micromolded features imprinted on the membrane. In contrast, the membrane transfer method consistently and evenly pre-tensions membranes prior to the gelation of micromolded features and therefor maintains the fidelity of micromolded features.

It should be emphasized that the use of planar sacrificial substrates to store tension in membranes is a generalizable method that is compatible with other microfabrication pipelines. Most membrane and microchip fabrication pipelines already utilize sandwiched assemblies of planar layers and are already compatible with the tension storage method. Furthermore, the stored pre-tension would be unaltered by subsequent temperature cycling steps, i.e. from downstream microfabrication processes, as long as the membrane remains laminated to its substrate. Since the underlying physical principle of pre-tensioning is the well-understood principle of thermal expansion, the structural reactions of the membranes to forces is readily described by quantitative modeling. This modeling ability enhances the utility of the method when applied to the fabrication of microdevices demanding precise and consistent structural properties, such as PDMS lenses. The accessibility, simplicity, and effectiveness of thermal pre-tensioning combined with its inherent compatibility with microfabrication and design pipelines makes the method a significant development for the microfabrication of microarrays, microfluidics and MEMs devices.

5.2.2 Brightfield detection of cells in microdevices

The image acquisition and standard deviation projection (SDP) analysis pipeline presented in Chapter 3 represents a straightforward method for detection of adherent cells. Critically, the method is label-free which simplifies experimental workflows and is inherently minimally

perturbative to cells, which is highly desirable for induced pluripotent stem cells (iPSCs) and iPSC-derived cells for disease modeling, basic biology research, or therapeutics. The SDP method specifically detects non-stationary objects within a specified focal range. This capability can be used to distinguish detect living, adherent cells from a background consisting of microfeatures, uneven illuminations, and debris. The pipeline is more specific and robust than contrast-based detection techniques that assume a uniform featureless image background. Although recent machine learning algorithms have been demonstrated to distinguish adherent cells from their surface, these require extensive supervised training datasets. The SDP method simply distinguished cells from an arbitrary culture substrate based upon their difference in focal plane. The adaptability of the SDP pipeline with respect to the culture surface makes it a superior option for *in vitro* culture applications on transparent microfluidics, microarrays, and engineered culture scaffolds.

5.2.3 High throughput functional organoid assays

The colonic organoid (colonoid) culture and assay method developed in collaboration with Dr. Dulan Gunasekara in Chapter 4 marks a new paradigm in colonoid research. Colonoids have a great potential as model systems for biological research and drug screening. However prior to this work, the functional variability within a population of colonoids and between populations derived from different individuals had not been widely explored outside of transcriptional heterogeneity.[1] Indeed, the majority of prior research was based upon observations of very few colonoids.[2] Furthermore, the reliance of prior methods on embedded cultures and confocal imaging precluded the use of colonoids for high-throughput, multiwell plate screening applications. With the development of a planar colonoid culture reported in this dissertation, the temporal size and morphology of thousands of colonoids can now be assayed per experiment with a motorized

widefield microscope and simple image analysis techniques. The marks an important technological milestone towards truly high-throughput drug screening with colonoids. Furthermore, the observation of marked heterogeneity in colonoid maturation rate and transmembrane transport function has important ramifications for experimental design with these organoids. In many cases, the marked heterogeneity in colonoids will require the analysis of many more colonoids to establish sufficient statistical power to test biological hypotheses.

5.3 Future Aims

The optimization of automated microscopy of microraft arrays in Chapter 2 lays the foundations for the use of higher resolution microscopy for microraft array cell sorting and cytometry. The autofocus, modeling, and image acquisition methods developed in this dissertation could allow the use of higher magnification objectives (20 × and greater) without incurring a loss in focus on cells, even on curved substrates. Higher resolution microscopy is essential to analyze compact cells (such as stem cells or epithelial cells) or to distinguish cells based on subcellular phenotypes (such as features of the nucleus, cell membrane, or mitochondria). Nicole Smiddy (UNC Allbritton Lab), Ian Williamson (UNC Magness Lab), Sebastian Mestril (UNC Allbritton Lab), and Brae Petersen (UNC Allbritton Lab) are currently engaged in microarray imaging applications making use of the technology developed in Chapter 2. These researchers' applications are, respectively, iPSC sorting based on expression of subcellular markers, organoid microinjection, calcium flux imaging, and chemical cytometry.

The technology to release large quantities of microrafts will enable cell cytometry and sorting based upon a screening paradigm. The novel applications of this technology are extensive. Hypothetically, screen-based cell sorting would enable almost any assayable biological or chemical factor of interest to be used to identify and isolate cells. In my postdoctoral research at

the Allbritton lab, I aim to continue my collaboration with the Ramsey lab and Transviragen, Inc. to develop a system capable of a genetic sort of iPSCs. In addition, Nicole Smiddy (UNC Allbritton lab) and the Purvis lab (UNC) are already applying microraft array-based sorting methods for sorting iPSCs. These projects will rely on the microraft cell culture, colony biopsy, and monitoring methods developed in Chapter 2 and 3 of this dissertation.

5.4 REFERENCES

(1) Gracz, A. D.; Williamson, I. A.; Roche, K. C.; Johnston, M. J.; Wang, F.; Wang, Y.; Attayek, P. J.; Balowski, J.; Liu, X. F.; Laurenza, R. J.; et al. A High-Throughput Platform for Stem Cell Niche Co-Cultures and Downstream Gene Expression Analysis. *Nat. Cell Biol.* **2015**, *17* (3), 340–349.

(2) Dekkers, J. F.; Wiegerinck, C. L.; Jonge, H. R.; Bronsveld, I.; Janssens, H. M.; Winter-de Groot, K. M.; Brandsma, A. M.; Jong, N. W. M.; Bijvelds, M. J. C.; Scholte, B. J.; et al. A Functional CFTR Assay Using Primary Cystic Fibrosis Intestinal Organoids. *Nat. Med.* **2013**, *19*, 939–945.

(3) Heo, I.; Dutta, D.; Schaefer, D. A.; Iakobachvili, N.; Artegiani, B.; Sachs, N.; Boonekamp, K. E.; Bowden, G.; Hendrickx, A. P. A.; Willems, R. J. L.; et al. Modelling Cryptosporidium Infection in Human Small Intestinal and Lung Organoids. *Nat. Microbiol.* **2018**, *3* (7), 814–823.